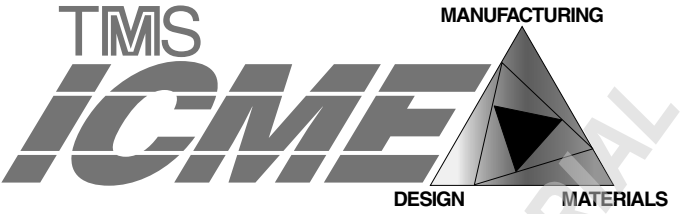

3rd World Congress

on Integrated Computational Materials Engineering (ICME 2015)

ICME Applications

3rd World Congress on Integrated Computational Materials Engineering (ICME 2015)
Edited by: Warren Poole, Steve Christensen, Surya R. Kalidindi, Alan Luo, Jonathan D. Madison, Dierk Raabe, and Xin Sun
TMS (The Minerals, Metals & Materials Society), 2015

IMPORTANCE OF CONTROLLING MICROSTRUCTURE HETEROGENEITY WHEN DESIGNING STEEL

Kohsaku Ushioda[1], Hideaki Sawada[1], Masaaki Sugiyama[1]

[1]Nippon Steel & Sumitomo Metal Corp., 20-1 Shintomi, Futtsu, Chiba, 293-8511, Japan

Keywords: Heterogeneity, Recrystallization, Phase transformation, Hydrogen embrittlement

Abstract

Steel has been used since long in the past, but there still remain many unexplored possibilities. In order to draw out this latent potential, the concept of materials integration is garnering attention in view of discontinuously improving the function and performance of steel products, while reducing the necessary development period. In this paper, considering the utilization of materials integration, the evolution of the microstructure during plastic deformation and phase transformation as well as controlling hydrogen embrittlement are discussed in terms of heterogeneity. In addition, a brief outlook on the future of materials integration is presented.

Introduction

One characteristics of steels is that they have a very wide range of strength, varying by up to about 100 times, as shown in Fig. 1 [1]. However, the strength levels used practically in various markets are only a fraction of steel's potential [1]. In this sense, steel can be called an attractive material which still has many unexplored possibilities. However, there remain many technical issues to be solved in order to draw out this latent potential.

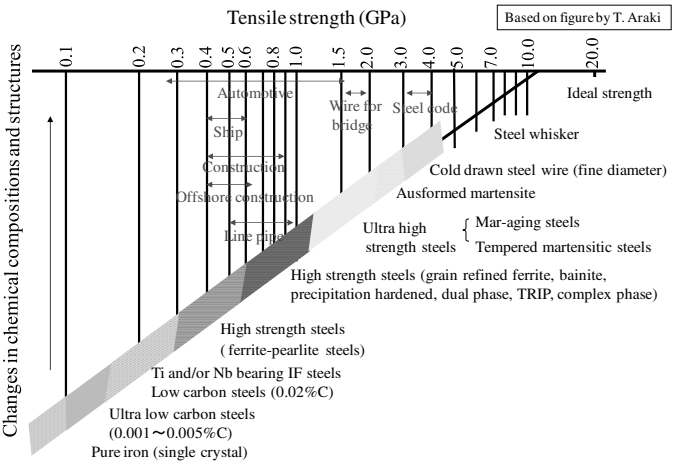

Fig. 1 Spectrum of steel strengths together with the strength levels of practically used steels [1].

Integrated Computational Materials Engineering (ICME) is an important concept and is considered to be the future direction of development.

In this paper, focus is first placed on the heterogeneous deformation structure in poly crystal Fe. Then, the effect of Boron (B) addition on retarding the austenite (γ) to ferrite (α) phase transformation is discussed. Also, since hydrogen embrittlement is one of the prohibiting factors to further increases in strength, the mechanism by which precipitates trap hydrogen is presented. Finally, the future outlook of ICME is presented.

Heterogeneous deformation structure and recrystallization

Heterogeneous deformation structure becomes most essential when controlling the microstructure and crystal orientation by recrystallization and phase transformation. The structure formed by rolling is heterogeneous as schematically illustrated in Fig. 2 [2]. The grain boundary region, shear band and deformation zone around hard second particles are typical heterogeneous deformation structures.

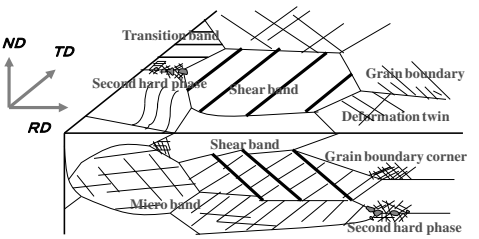

Fig. 2 Schematic illustration of the heterogeneity of a cold-rolled structure [2].

An example of heterogeneous deformation nearby a grain boundary is shown in Fig. 3 [3]. IF (Interstitial Free) steel with a grain diameter of about 40μm was cold-rolled by 80%. As a result of the statistical analysis of 84 grain boundaries parallel to the rolling plane, the boundaries were classified into one of the following three boundaries depending on the neighboring orientation relationship; a) relatively flat boundary, b) irregularly serrated boundary, and c) boundary associated with fine grains. In particular, it is worthy to note that 22 of the 84 boundaries analyzed were classified as case c).

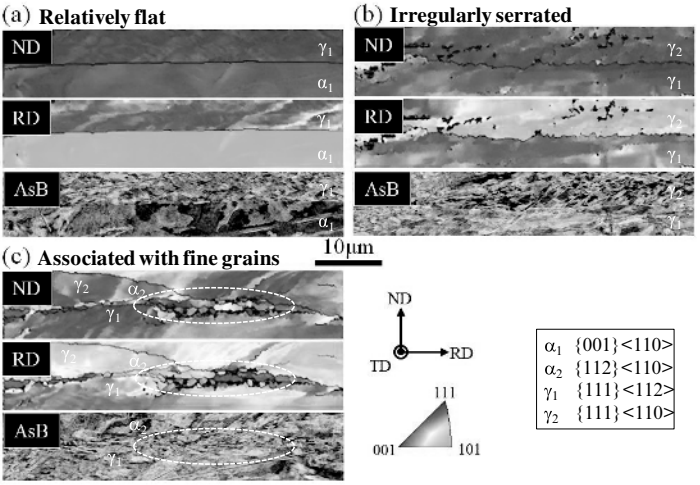

Fig. 3 Heterogeneous cold-rolled microstructure in the vicinity of a grain boundary [3].

A TEM micrograph of a shear band and its 3D schematic illustration is shown in Fig. 4 [3, 4]. Fe-0.02C (mass%) was water quenched from 700ºC and then cold-rolled by 70%. Intensive shear was localized in the shear band, and the crystal rotated from {111}<112> in the matrix to Goss orientation ({110}<001>) in the shear band around the TD//<110> axis.

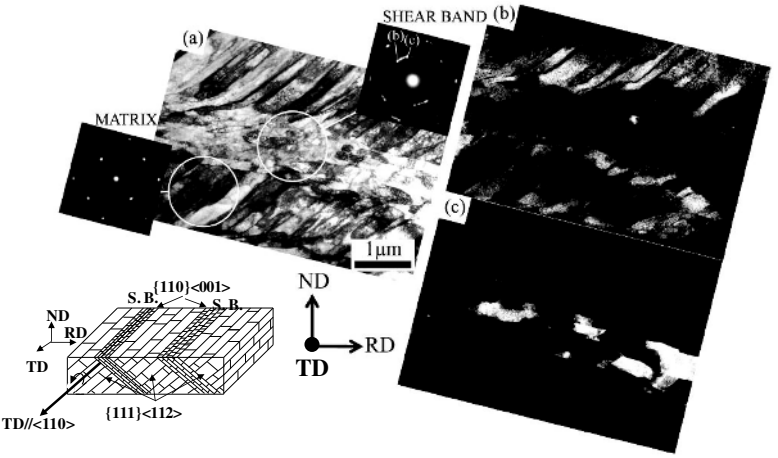

Fig. 4 TEM bright field image showing shear band, and diffraction pattern together with dark field images. 3D schematic illustration of shear band is also presented. [3, 4]

The heterogeneous deformation around the hard second phase is shown in Fig. 5 [5]. Fe-0.07C-16Cr was quenched from two phase region and then cold-rolled by 75%. EBSD analysis shows that large strain was concentrated around the hard α' (Fig. 5 a). However, when α' was tempered at 550 ºC for 1h prior to cold-rolling, the deformation became rather uniform (Fig. 5b).

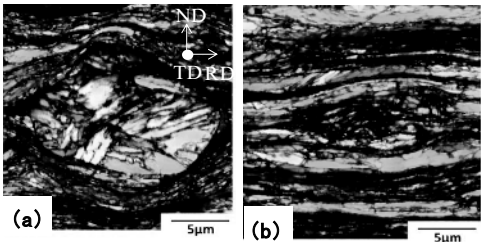

Fig. 5 Deformation zone around a hard second phase in Fe-0.07C-16Cr. (a) quenched α' and (b) tempered α' [5].

The heterogeneity in deformations has neither been systematized experimentally nor been rigorously predicted. Therefore, there is a strong need to predict the heterogeneity by 3D CP-FEM or FFT and then verify the predictions by, for example, 3D XRD experiments. Ultimately, a numerical approach is expected to predict the evolution of the microstructure and texture during recrystallization and phase transformation using predicted heterogeneous deformation structure through a combination of the crystal plasticity and phase field method. Despite the fact that research is being carried out in this direction [6-8], there still exist issues to be overcome in the future.

B segregation to the γ grain boundary and its effect on the γ/α phase transformation

It is well known that the addition of several massppm of B retards the γ/α phase transformation and subsequently improves hardenability, because B segregates to the prior γ grain boundary. Therefore, the addition of a small amount of B is effective from the standpoint of reducing the amount of necessary alloying elements and relaxing the process conditions.

Recently, B segregation to the γ boundary has been investigated using CS-STEM [9]. B segregates as much as 1600 times with a thickness of about two atomic layers (Fig. 6 a). On the other hand, the first principle calculation was applied to B segregation. The segregation energy to the Σ9 boundary, which is rather close to the general boundary, was evaluated [10]. Taking into

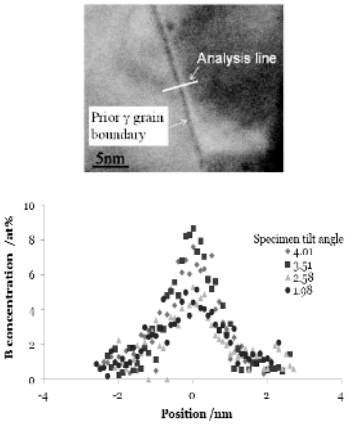

a)

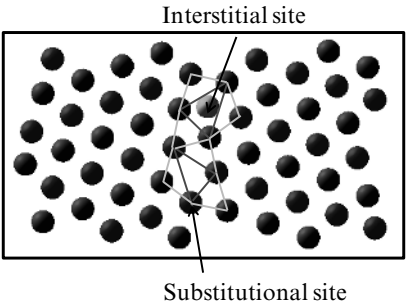

b)

Fig. 6 a) STEM image and B concentration profiles measured by CS-STEM with several tilt angles around the prior γ grain boundary of Fe-0.05C-1.5Mn-3Ni-0.0011B (mass %) annealed at 950ºC for 60s, then cooled to 650ºC with a cooling rate of 30ºC/s followed by He quenching [9], and b) schematic view of B segregation into Σ9 grain boundary and structure units after first principle calculation [10].

consideration structure relaxation, magnetism and change in lattice constant at high temperature, the segregation energy varied from -2.24 to -0.70 eV, which is similar to the value -0.59~-1.0 eV found by Auger spectroscopy. Moreover, a calculated grain boundary structure unit as shown in Fig. 6 b) resembled the one observed in the Σ9 Cu grain boundary [10].

The kinetic model for γ/α phase transformation was studied taking into account B segregation to the γ boundary using the difference in grain boundary energy $\Delta\gamma^{\gamma\gamma}$ described in Eq. (1) [11]:

$$\Delta\gamma^{\gamma\gamma} \fallingdotseq -\delta / (V_m^{gb}) RTkx^{\gamma} \qquad (1)$$

, where, δ, V_m^{gb}, k *and* x^{γ} are the thickness, molar volume, segregation coefficient and concentration of B at the γ grain boundary, respectively.

A value of -0.12Jm^{-2} for $\Delta\gamma^{\gamma\gamma}$ was obtained by substituting experimentally determined values. Fig. 7 shows the relationship between the critical activation energy for α nucleation at the 4-grain junction at 705 ºC under conditions where the γ/α interface energy was 0.5Jm^{-2} and 0.6Jm^{-2}. It is clear that α nucleation is drastically retarded due to the fact that the addition of 0.002% B decreases $\gamma^{\gamma\gamma}$ by 0.12Jm^{-2}. Furthermore, DICTRA calculations suggest that the addition of B does not affect the α growth, which is in good agreement with the experimental result [11]. The coexistent strong effect of Nb and Mo with B on γ/α phase transformation is well known; however, the effect

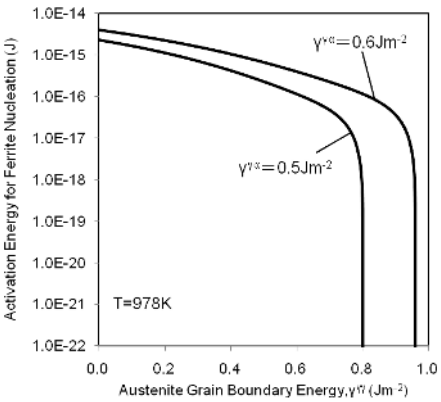

Fig. 7 Calculated activation energy for α nucleation as a function of γ grain boundary energy $\gamma^{\gamma\gamma}$ at 705ºC for two γ/α interfacial energies $\gamma^{\gamma\alpha}$ [11].

needs to be modeled in order to more effectively exploit the addition of B.

Resistance to hydrogen embrittlement by means of hydrogen trap

Hydrogen embrittlement is one of the inhibiting factors to further strengthening steel. Irrespective of the various mechanisms proposed for hydrogen embrittlement, it is essential to trap hydrogen by fine precipitates. The TiC/α-Fe interface is an example of trap site. A direct observation of the trap site was successfully made by 3D AP as shown in Fig.8 [12]. The material used was precipitation hardened steel of 0.03C-0.2Mn-3.0Al-0.1Ti, which was water-quenched from 1250 ºC in α-Fe phase followed by aging at 580 ºC for 4h in order to form fine TiC. AP observation was carried out after charging deuterium into the specimen. The reason for using deuterium was to improve the detection sensitivity, because deuterium occurs very infrequently in nature, but has chemical characteristics similar to hydrogen. The trapping of deuterium in the TiC/Fe interface is clearly shown in Fig.8, which is presumably due to elastic strain and/or misfit dislocation in the semi-coherent interface.

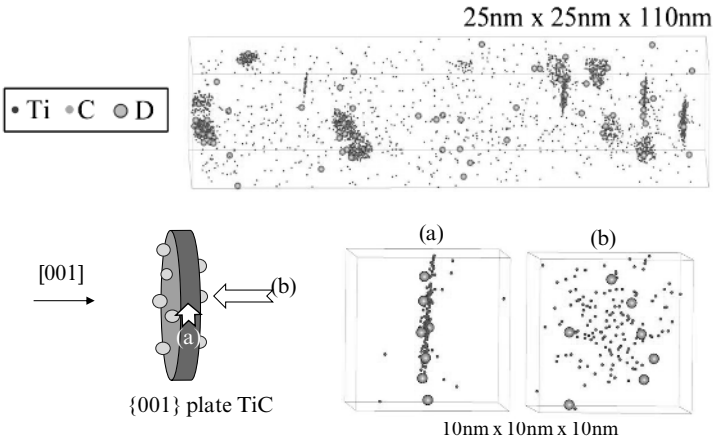

Fig. 8 3D AP elemental mapping showing deuterium trapped by TiC in α-Fe [12].

Recently, the interfacial energy of NbC/α-Fe has been predicted by first principle calculation through the application of the order (N) method [13]. Fig.9 a) shows the results of the interfacial energy for coherent and semi-coherent interfaces. The lowest interfacial energy, 0.6J/m^2, occurred at the coherent interface, where the C atom of NbC positions on an Fe atom in the matrix. On the contrary, the interfacial energy at the semi-coherent interface was as large as 1.2J/m^2. The atomic configuration of semi-coherent interfaces is illustrated in Fig.9 b), where the lattice in the matrix bends in such a manner for an Fe atom to site beneath the C atom of NbC resulting in the formation of a misfit dislocation.

Nano-precipitates of the alloy carbides TiC, NbC and VC have been characterized as having the hydrogen trapping property [14]. The hydrogen trapping ability of (semi-) coherent alloy carbides was clarified to vary in the descending order of NbC > TiC >> VC presumably due to the difference in lattice misfit. The hydrogen trap energy depending on the trap site may be obtained by

Table1 Calculated trap energy (kJ/mol) of a hydrogen atom by TiC and VC in α–Fe [15].

	VC	TiC
Coherent strain	<15	<29
Interstitial site	-106	-58
C vacancy	116	125
Coherent interface	-6	48

first principle calculation, but calculation has not been performed for semi-coherent nor incoherent interface [15]. The calculated potential energies for hydrogen atoms trapped by TiC and VC are summarized in Table 1. TiC is expected to trap hydrogen in the coherent interface, whereas the C-vacancy in VC might be the trap site, but not be effective in the case of the high diffusion barrier. Computational material science is expected to be intensively exploited for the purpose of investigating the effective hydrogen trap sites.

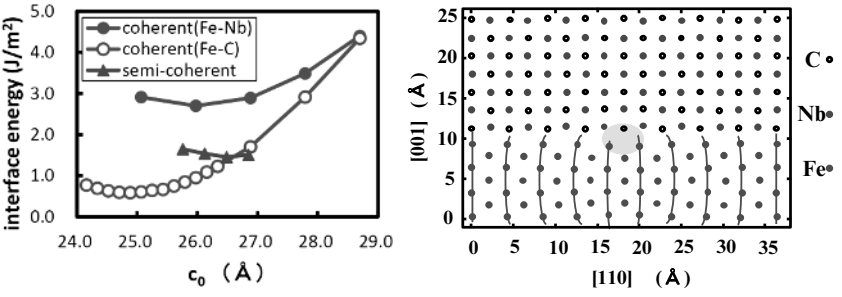

a) b)

Fig. 9 a) Calculated interface energies of the coherent and semi-coherent NbC/ α-Fe interface as a function of the length of C_0, b) atomic configuration of the semi-coherent interface in the (110) plane [13]. The region of the dislocation core is positioned in the center of interface.

Future outlook

For the purpose of fully exploiting ICME, it is necessary to first brush up the fundamental research in the individual fields. Simultaneously, depending on the objectives, the relevant issues should be solved by linking and integrating the technologies in different fields. Furthermore, international collaboration will become more important in the future.

References

1. K.Ushioda, "Challenge for further strengthening of steels," Proc. 2nd Int. Symp. on Steel Science (ISSS-2009), Ed. by K. Higashida and N. Tsuji, ISIJ, Kyoto, (2009) , 39-48
2. K.Ushioda and H.Tsuchiya, "Fundamentals for controlling the microstructure and properties of cold rolled and continuously annealed sheet steels," *Trans. Ind. Ins. Met*, **6**6(2013), 655-664
3. K.Ushioda, S.Nakanishi, T.Morikawa, K.Higashida, Y.Suwa and K.Murakami, "Evolution of heterogeneous deformation structure and recrystallization texture of steel," *Mater. Sci. Forum*, **753**(2013), 58-65
4. S.Nakanishi, T.Morikawa, K.Higashida, H.Murakami, K.Kimura and K.Ushioda, "Effect of solute carbon content of microstructures of cold-rolled ferritic steel," *Tetsu-to-Hagane*, **98**(2012), 253-261
5. K.Kimura, K.Ushioda, J.Hamada, E.Ishimaru and A.Takahasi, "Recrystallization behavior of SUS 430 stainless steel containing hard second phase prior to cold-rolling," to be published.
6. J.Humphreys, P.Bate, A.Gholinia and I.Brough, "Measuring and modelling the microstructures of two-phase aluminium alloys after deformation," *Mater. Sci. Forum*,**715-716**(2012), 23-32
7. T.Takaki, A.Yamanaka, Y.Higo and Y.Tomita, "Development of phase-field model and

computational procedure during static primary recrystallization," *Jpn Soc. Mech. Engi. A*, **73**(2007), 482-489
8. A.Yamanaka, T.Takaki and Y. Tomita, "Simulation of austenite to ferrite transformation in deformed austenite by crystal plasticity finite element method and multi-phase-filed method," *ISIJ Int*., **52**(2012), 659-668
9. G.Shigesato, T.Fujishiro and T.Hara, "Boron segregation to austenite grain boundary in low alloy steel measured by aberration corrected SEM-EELS," *Mat. Sci. Engi. A*, **535**(2012), 358-365
10. H.Sawada, "First principles study of grain boundary embrittlement in Fe-Ni-S alloy," *Comp. Mater. Sci.*, **55**(2012), 17-22
11. S.Yoshida, K.Ushioda and J.Agren, "Kinetic model of the γ to α phase transformation at grain boundaries in Boron-bearing low-alloy steel," *ISIJ Int.*, **54**(2014), 685-692
12. J.Takahashi, K.Kawakami, Y.Kobayashi and T.Tarui, "The first direct observation of hydrogen trapping sites in TiC precipitation-hardening steel through atom prove tomography," *Scripta Mater.*, **63**(2010), 261-64
13. H.Sawada, S.Taniguchi, K.Kawakami and T.Ozaki, "First-principles study of interface structure and energy of Fe/NbC," *Modelling Simul. Mat. Sci. Eng*., **21**(2013), 045012
14. F-G Wei, T.Hara and K.Tsuzaki, "Nano-precipitates design with hydrogen trapping character in high strength steel," *ASM Int*., ISBN-13:978-1-61503-003-3, (2009), 448-455
15. K.Kawakami and T.Matsumiya, "Numerical analysis of hydrogen trap state by TiC and V_4C_3 in bcc-Fe," *ISIJ Int.*, **52**(2012), 1693-1697

3rd World Congress on Integrated Computational Materials Engineering (ICME 2015)
Edited by: Warren Poole, Steve Christensen, Surya R. Kalidindi, Alan Luo, Jonathan D. Madison, Dierk Raabe, and Xin Sun
TMS (The Minerals, Metals & Materials Society), 2015

ICME FOR PROCESS SCALE-UP: IMPORTANCE OF VERTICAL AND HORIZONTAL INTEGRATION OF MODELS

Gerald Tennyson, Rishabh Shukla, Saurabh Mangal, Savya Sachi, Amarendra K Singh

Tata Consultancy Services, Pune 411 013, India

Keywords: vertical-horizontal integration, process scale-up, multi-scale modelling, multi-phase modelling

Abstract

ICME will play a major role in reducing the lead time in development of a new product or component. One of the areas where ICME is likely to play a crucial role is process scale-up of mill products. Process scale-up of a mill product from laboratory to production stage is largely done through hit-and-trial and is a non-trivial exercise. It involves plant level trials which are expensive and time consuming. Use of ICME can significantly narrow down the design search space thereby reducing need for experimentation or plant trial, which in turn will lead to bringing down the cost and time of development. However many challenges need to be addressed to realize the full potential of ICME at an industrial scale. Manufacturing any product/ component involves a host of unit operations and the properties of the end product are intrinsically linked with final as well as intermediate processing steps. To link the material-processing-structure-performance matrix, there is a need to enhance models across various unit operations through multi-scale/multi-phase modelling and integration of models at various length scales. This allows for the information flow across various unit operations and thereby ensures horizontal integration of each process to simulate the entire manufacturing chain. This step is crucial in designing set points and quantifying the influence of various unit operations on end product performance. In this paper, we illustrate the vertical-horizontal integration of models through an example

Introduction

Modelling of materials processing and metallurgical operations has come a long way since its inception in the early seventies. Application of mathematical modelling in metallurgical process optimization, which began around the late seventies, has also progressed a long way. In current scenario, mathematical modelling and simulations are extensively used in several processing industries to either select a suitable design of equipment for their unit operations or to optimize the process operation. We illustrate the use of modelling and simulation technique for design and process optimization in steel industry with the help of few examples. In the recent past, steel industry has adopted major technological advances to compete with the challenges posed by new advanced materials. Steel manufacturers are striving to manufacture product mix with newer grade of steels (advanced high strength steel, for example) for improved properties. Manufacturing a steel product mix (rod, bar, sheet) involves a series of unit operations (see Figure 1), each having a significant influence on the final properties. Models to capture the effect of various phenomena occurring in a unit operation exist and are used frequently. We provide a gist of information on the current state of mathematical models for two of the unit operations, namely ladle refining and continuous casting.

Mathematical Models of Ladle Refining and Continuous Casting Operations

Ladle furnace receives steel form basic oxygen or electric arc furnace and is the key to maintain desired level of steel cleanliness and maintaining composition of alloying elements (Ni, Cr, Mn etc.) within a specified band. Steel cleanliness is assessed with respect to the amount and nature of

inclusions present and the level of tramp elements such as sulphur, oxygen and phosphorus in steel. The aim of refining operation is to facilitate deoxidation, superheat control, desulphurization, and inclusion removal to meet the specified requirements to meet the chemistry and cleanliness requirements at the end of ladle refining operation.. Mathematical models have been developed and employed to model the aforesaid phenomena. Singh et al. have developed a chemistry model to predict amount of additives to be added for maintaining desired steel and slag composition and a thermal model to account for the heat losses that occur during refining, thereby suggesting an arcing strategy to compensate for the same [1]. Population balance method (PBM) based inclusion evolution model to study the behaviour of inclusions and calculate final inclusion distribution coming out from ladle has been developed [2, 3]. To account for inclusions that are formed during course of refining, thermodynamic modelling is done and is coupled with PBM model. Lots of investigations are reported with respect to removal of sulphur during refining. Maintaining desired level of slag basicity and having favourable flow conditions to increase slag/steel interfacial area is of prime importance to facilitate sulphur removal. Models have been developed to study the effect of purging rate on sulphur removal [4]. Anderson et al. [5] talk about importance of slag compositional control for sulphur removal. They have developed model to calculate final sulphur content in steel with variation in the composition of ladle furnace slag. There are several other models addressing design related issues and other important aspects of ladle refining operation. We have provided a glimpse of some of the models that are used to understand various phenomena in ladle refining. We next describe few models used to understand few phenomena in continuous casting operation.

Caster receives steel from tundish and is a crucial step in formation of variety of steel products from liquid steel. The performance of casting operation is assessed in terms of productivity, quality parameters such as segregation, crack index, oscillation mark depth and cost of production. Different phenomena take place during casting that influences the aforesaid performance measures. Mathematical models have been developed to model these phenomena and design casting operation to meet the quality and productivity requirements. During casting, segregation of solutes takes place owing to difference in solubility limit in solid and liquid phase. Models are available to predict centre line segregation (CLS) in cast slab [6] and thereby designing the casting operation in a way to have severity of segregation within tolerable limit [7]. Thermo-mechanical models are available to predict surface and internal crack in a slab which occur as a result of thermal stresses developed during solidification. The model is used to optimize the cooling conditions in different segments of caster to produce a slab having cracks within acceptable limit. During continuous casting, inclusions get redistributed into columnar and equiaxed zone, which affect the quality of final product. Transition of morphology from columnar to equiaxed is thus of great importance for industry. Models are available to predict the location of columnar equiaxed transition and compute the relative proportions of columnar and equiaxed zone [8]. Another important phenomenon to occur during solidification is micro-segregation. Micro-segregation results in variation of solute concentration in the inter-dendritic region and lead to a situation favourable for formation of precipitates [9]. Models are available to capture micro-segregation during solidification, which is then used to predict evolution of precipitates during casting operation.

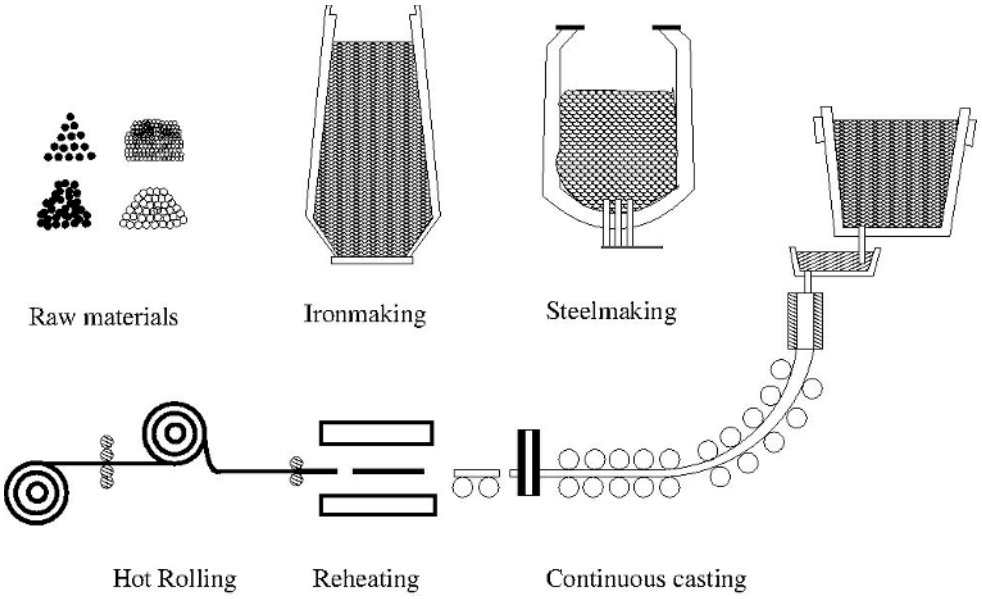

Figure 1. Schematic of operations in steel processing

The previous sections provide a glimpse of few mathematical models, used to study different phenomena occurring in two unit operations and address the associated challenges. The models that we have talked about previously are problem specific and are not studied in conjunction with the other phenomena. For example, desulfurization model is used to decide slag chemistry and argon purging during refining to optimize sulphur removal. However, while studying the same we do not consider deoxidation and inclusion evolution model. As a result, we may end up with desired sulphur content in steel but slippage may happen in other requirements (inclusion content, superheat etc.). This can be qualified by a study reported in [10], which says high purging rate is desired for sulphur removal which on other hand is detrimental for inclusion content as high purging lead to increase in oxygen pick up (increase in slag eye opening). Thus, a mathematical model used for process or design optimization of a unit operation should combine all important associated models to meet the conflicting requirements of productivity and quality of the product. It is important to note here that the product of ladle operation is steel melt for tundish and product of casting operation is slab or billet. Also, requirements of these products are well specified: Target chemistry and cleanliness in case of ladle refining and segregation level and other quality parameters in case of cast product. These have come about through trial and error and years of experience. In contrast, for process scale up of a new grade, the product requirements at the end of ladle refining, caster and other unit operations are not known apriori and need to evolve to meet the ***end product requirements.*** Thus, in ICME framework, modelling of unit operations is entirely different and the focus here is to generate information flow to immediate next and subsequent operations so as to relate these to end product requirements. For example, CLS model is used to design casting operation in a way so as to have severity of segregation within control (a requirement on slab). However, the CLS model does not give us any information on the composition profile in slab, which is very critical when we talk about deformation behaviour during rolling operation. In such a situation, a slab that has qualified after casting operation with respect to segregation level may not be suitable to be rolled. The silo-based study of unit operation is therefore not useful for development of steel product with specific properties.

Above discussions establish the need of ICME approach of model development and study. In ICME

approach, the flow of information from one unit operation to other is essential which enable us to carry out integrated study of each operation (termed horizontal integration) [11], unlike what is done in silo-based approach. The horizontal integration of unit operations requires information in far greater details, which will require modelling each phenomenon with a deeper insight. For example, requirement on steel product is put with respect to total oxygen content, which is a measure of inclusions present. Simple chemistry model is used to optimize ladle refining and predict operating conditions to meet total oxygen requirement. However, if we are doing an integrated study, further detailed models will be required to be able to provide information on chemical composition of inclusions, its type, morphology and size, as this information need to be passed on to the subsequent unit operation (during rolling). This will enable us to study the behaviour of inclusions of different size, shape and type during rolling. The integration of models for different phenomena and models at different length scales (termed as vertical integration) is required to establish the information required by subsequent unit operations. One such study in integrating computational thermodynamics with kinetics simulations on the strengthening mechanisms in magnesium alloys at elevated temperatures is done by Bryan et al.[12] The vertical integration is useful not only to obtain information required by subsequent operation but also help us to have a better understanding and process design of the corresponding unit operation as well. For example, integration of thermal, desulphurization and inclusion evolution model during refining helps us to explore the design set points of ladle operation to have a balance between these critical requirements. Focus in such a case is not to have maximum of one requirement but to achieve the specified target with respect to all three requirements. This is an aspect which remains untouched when doing optimization using an individual model.

Problem Statement

We have talked about importance of modelling and simulation in studying various processes. The essence of vertical-horizontal integration in ICME approach of development of materials, products and associated manufacturing processes is presented. Next, we explain the importance of proposed method of horizontal-vertical integration for solving a problem encountered during sheet manufacturing in steel industry. Suppose steel mill is involved in production of sheet with certain grade of steel. The operating constraints and process requirements are known to process designer as they are involved in sheet manufacturing day-in-day-out. However, if happens a scenario where owing to the changed performance and properties requirements, manufacturers are asked to produce sheet with a newer grade of steel with enhanced properties. This grade of steel is used to manufacture sheet at a laboratory scale, but now the challenge posed to sheet manufacturers is to scale-up the production from lab to an industrial scale. This requires exploring the design set points of each unit operation to produce the sheet with desired properties at a plant scale. One way of doing this is to resort to experimentation and plant trials, which is highly expensive and takes a lot of time (8-10 years for automotive materials). Other way is to use computational models for exploring the design set points, thereby reducing experimentation and time and cost incurred in the development. However, current models are problem specific and are developed to address issues of a particular phenomenon. The optimization of process using these models in isolation will not be a true representative of desired solution. The need of the hour is to use ICME approach of models integration to explore the solution space for production of a sheet. This requires exploring the design set points of involved unit operations, which in turn requires knowledge of operating constraints and requirements, which is not available for the case where sheet is being manufactured with a new grade of steel. The first task thus is to identify operating constraints and requirements for each unit operation, which is imposed by the subsequent unit operations as each process step is connected and information flows form one operation to the other. Schematic showing flow of information across the entire sheet manufacturing chain is presented in Figure 2. Identifying the aforesaid operating constraints process requirements requires having information about each spec in sufficient details. The vertical integration of models provide a way to obtain these information in

greater details (as is required), which is then passed across other unit operations to put constraints and requirements on them. This flow of information from one unit operation to other that allows for integrated study is termed as horizontal integration. For example, thermodynamic model for inclusion formation is integrated with PBM model and kinetics based model to calculate size, shape and type of inclusions. This information is passed on to subsequent operation and sets up a requirement for them. This way, we make use of vertical-horizontal integration to explore the design set points for manufacturing sheet with a new grade of steel. Next, we talk in greater detail about integration of models to obtain detailed information and making use of this information to predict the design set points of unit operation for manufacturing sheet with desired properties.

1. Integration of models to predict composition, size, shape and distribution of inclusions in the cast slab. This information is used in predicting the performance of final product (with respect to fatigue life) and studying the behaviour of slab during rolling.
2. Integration of models to predict micro-segregation and evolution of precipitates during solidification. This information is used to predict design set points of reheating operation.
3. Integration of models to obtain compositional profile across cast slab and precipitates. This information is used to predict design set points of reheating operation.

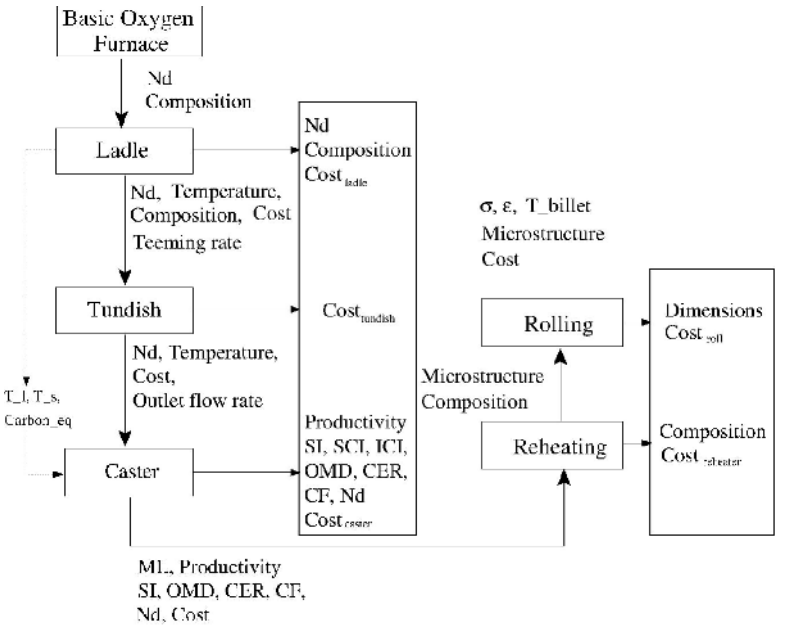

Figure 2. Flow of information across process chain

Illustrations of Vertical-Horizontal Integration

Models Integration for Inclusion Characterization

The aim of this vertical integration is to characterize inclusion distribution in the cast slab. The importance of this information and the modelling strategy adopted to obtain the same is elucidated. Let us consider a situation where the interest is to manufacture a sheet with specified fatigue life. Presence of inclusions significantly affects the fatigue life of sheet and inclusions in industry are measured in terms of total oxygen. The specification on fatigue life sets up a requirement to have

oxygen content in steel below 10 ppm. However, having total oxygen content below specified limit does not guarantee desired fatigue life as total oxygen is only a measure of amount of inclusions and do not tell anything about their composition, size, shape and distribution. Lot of study has been done to establish the effect of inclusions on fatigue life. Salajegheh et al. have carried out finite element simulation to study the effect of clustering of inclusions on performance of advance high strength steels during fatigue loading [13]. This establishes the importance of studying spatial distribution of inclusions in the cast slab. Performance of sheet during fatigue loading also depends on how the inclusions behave during rolling operation. The behaviour of inclusions during deformation depends on the type of inclusions, i.e., whether it is a hard inclusion or soft inclusion and how is it distributed in the matrix. Akash et al. [14] have studied the behaviour of hard and soft inclusions during hot rolling [14]. Luo in his thesis [15] has developed a model to study the behaviour of inclusions during rolling which in turn helps in carrying out rolling in a way so as to improve the properties of the final product. For example, he has reported a transition temperature for silicate inclusion below which these behave as non-plastic and plastic at temperature above. The studies reported above establish the importance of having inclusions information in far detail than merely using total oxygen as qualifying criteria. Next, we explain the modelling framework which can be utilized to obtain this information and preserve it to be utilized during rolling. Inclusions are largely removed or modified during ladle refining. Inclusions coming from basic oxygen furnace are removed and new inclusions, owing to refractory erosion and deoxidation, are formed during ladle refining. Information on size, shape, composition and distribution of inclusions has to be modelled during ladle refining. Integration of different models such as thermodynamic and kinetics model, population balance and fluid flow model (vertical integration), is used to obtain the aforesaid inclusion information. This information is then passed on to the next unit operation of continuous casting. Inclusions of different types and sizes from the ladle arrive at the caster with a given volume fraction and number density. Inclusions of all types are generally homogeneously distributed in the liquid steel but during solidification in caster, redistribution of inclusions occurs in the slab. It should also be noted that it is difficult to measure the distribution of inclusions in the cast slab even by a destructive examination of the slab. The difference between the solid and liquid densities causes the inclusions to either get trapped within the solid or transported to different sections in the cast. Inclusions in the melt are pushed towards the center mainly due to the moving columnar front. The spatial distribution of inclusion largely depends on the location of columnar-equiaxed transition (CET). However, not all the inclusions are pushed towards the CET. It has been established that the primary and secondary dendrite arm spacings (PDAS and SDAS) depend on the thermal gradient and the cooling rate respectively. In general, it is assumed that the inclusion whose size lies within the PDAS get engulfed by the growing columnar dendrites and those above, are pushed towards the center. By far, the most commonly used method to determine the location of inclusions is the model by Hunt [8], where it is possible to determine the location of the columnar to equiaxed transition zone using the thermal gradient and cooling rate information. We have developed a model based on Hunt's criteria on CET to predict inclusion size distribution in the cast slab. The number density of inclusions along with their sizes is shown in Figure 3. It is assumed at this point that the inclusions that are entering the cast (initial) get segregated in the center.

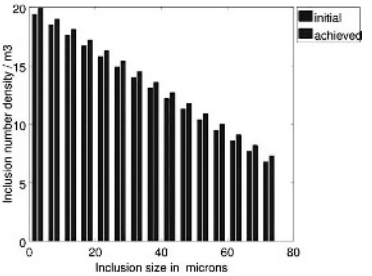

Figure 3. Variation in the inclusion number density as a function of its size

Further enhancements to the model are underway to determine the spatial variation of these inclusions throughout the cast section. We are incorporating the information on PDAS and SDAS into the current model (described above) to predict the spatial distribution of inclusions across the slab, which plays a significant role in determining the behaviour of slab during deformation and subsequently its properties.

We have obtained some information on inclusions which have been shown in the above figure. Following a similar vertical integration modelling strategy, we can obtain the detailed information on size, shape, composition, volume fraction and spatial distribution of inclusions. This information is then linked to models of rolling operation (horizontal integration) and is used to design the rolling process in a way so as to avoid any crack formation during deformation and to ensure attainment of desired fatigue life in the final sheet.

Models Integration to Predict Precipitates Evolution

The aim of this vertical integration is to obtain the information on level of micro-segregation and type, size and shape of precipitates formed during solidification. The importance of this information and the modelling strategy adopted to obtain the same is elucidated. Final properties of sheet depend on the microstructure and defects level present. Presence of certain precipitates in cast slab which is rolled, may have a tendency for crack formation and propagation and thereby increases the defect levels in the final sheet, more than the specified limit. It is essential to ensure such precipitates are not present in the slab to be rolled. This sets a target on reheating operation to ensure the precipitate requirements are met, so that no problems are encountered during rolling. We then need to obtain the information on size, shape and type of precipitates present in the slab that is reheated. The formation of precipitates during solidification depends on various factors such as localized variation in composition due to macro and micro-segregation, flow conditions, dendrite arm spacing etc. Lots of work has been done in past to understand micro-macro segregation, precipitation kinetics, fluid flow during solidification. However, these models have been used in isolation to optimize the casting operation with respect to a specific problem. This may help us to take care of a specific problem, but may lead to occurrence of others and we may not be able to capture the required information on size, shape and type of precipitates in sufficient detail. In this work, we illustrate vertical integration of different models (micro-macro segregation, precipitation kinetics, and fluid flow) to predict type, size and shape of precipitates formed (required by reheating operation as stated above).
Chemical composition of the alloy, cooling rate and thermal gradients decide the nature of precipitates that may form. Precipitation kinetics is modelled using a Scheil-Gulliver scheme, where solutal information is able to predict the type of precipitates that would form. Coupled with cooling rate, it is also possible to quantify the volume fraction of the precipitates that are evolving. Integrating precipitation kinetics and thermal model with a macro-segregation model is essential, because calculating precipitates evolution using nominal composition does not provide the exact representation of the actual scenario. During casting, as solidification proceeds, due to convective forces, macro-segregation causes the solutes to get redistributed along the length of the cast, thereby altering the nominal composition along the entire domain of the cast. The variation in the solute levels caused during macro-segregation further affects the solidification behaviour of the alloy. Different regions in the cast now tend to solidify differently. Solute rejection from the primary phase leads to micro-segregation. This also gets affected by the variation in the localized composition field caused by macro-segregation. We report evolution of precipitates MnS and NbC for both the aforesaid cases (with and without integration of macro-segregation model) to illustrate utility of vertical integration. In the absence of macro-segregation, solute segregation levels are uniform and we expect a uniform distribution of MnS and NbC depending on the cooling rate and segregation levels. The same is observed with the first model, which is evident from the horizontal lines for MnS and NbC (see Figure 4). However, when we use second modelling strategy (macro-

segregation model integrated), a significant variation in the size, volume fraction and the number density of the precipitates. This is shown by extracting few zones along the length of the cast viz., along the centre line (CL) and quarter line (QL) and is elucidated clearly in Fig 4.

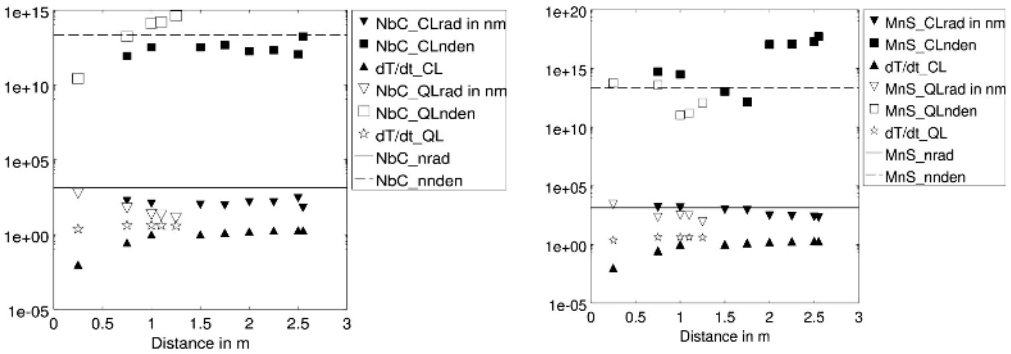

Figure 4. Size distribution along caster length for (a) NbC precipitates and (b) MnS precipitates respectively

MnS and NbC which are formed along the grain boundaries have a tendency to pin the grain boundaries during rolling. NbC, in particular, will not allow grain boundary migration to occur during recrystallization due to the solute drag effect. Their tendency to cluster makes it more difficult to subject the material to rolling as they might form voids. It thus becomes necessary to reduce the volume fraction of these precipitates. Reheating the slab to remove the precipitates is necessary. Generally in reheating, the time-temperature profiles are designed assuming the volume fraction of the precipitates that might form for a given alloy composition. Depending on the melting point and the volume fraction of the precipitates, the time taken and the temperature required for dissolution is calculated. It also needs to be pointed out, that there exists a trade-off between the volume fraction of the precipitates and the austenite grain size. Designing a reheating profile for higher dissolution, will also tend to increase the austenite grain size. This reduces the number of ferrite nucleating sites leading to larger ferrite grains thereby decreasing the toughness and strength. We have obtained the information on size, shape, type and volume of precipitates present in the cast slab and target precipitate level (stated above) needed to ensure smooth rolling operation. Incorporating the same in the reheating model and exploring the design space enables us to determine the time and temperature of reheating required to aid in dissolution of precipitates. Another important consideration while design exploration is to have a trade-off between dissolution of precipitates and austenite grain size. If we aim higher dissolution, austenite grain size increases, leading to lesser nucleation sites for ferrite, implying larger ferrite grain size and decrease in toughness of the final sheet. Thus, we explore the design set points of reheating operation to have a balance between these two conflicting requirements of dissolution and austenite grain size.

Models Integration to Predict Constitutive Relation

The aim of this vertical integration is to obtain the constitutive relations which explain the deformation behaviour of a material during rolling as a function of composition, precipitates and inclusion density and distribution, etc. We explain the importance of this information and what modelling strategy was adopted in obtaining the same. In sheet metal production, reheated slab is subjected to multiple reductions. Depending on the reduction ratio, it becomes necessary for the material to undergo multiple stages of roll passes. Many factors influence a material's response to deformation such as microstructural inheritance from previous processing routes, temperature,

composition, precipitate type and volume fraction of inclusions. In the absence of such information, practice is to develop solutions based on well-established constitutive relations, which give the bulk values of stress, strain as a function of nominal composition. However in such a case, information hidden in the form of precipitates, hard-soft inclusions and solute segregation is not captured to study the deformation behaviour of material. It therefore becomes necessary to enhance the constitutive models bringing in the effect of information on inclusions, precipitates and solute segregation.

In current work, we try to bring in the effect of micro/macro-segregation on constitutive relations. The information on micro and macro-segregation is available from previous unit operation (casting, reheating). This information is then used to calculate the spatial variation of stress as a function of composition along different points in the slab. The calculation is done based on a model by Gladman et al. [16], which considers the influence of chemical composition of steel on yield stress. The yield strength value at different locations of slab with varying composition (owing to micro and macro-segregation) is obtained through the simplified relation from Gladman,

$$\sigma_y = 88 + 37.2\,[\text{wt\% Mn}]\,83\,[\text{wt\% Si}] + 2900\,[\text{wt \%N}]^{0.5} + 17\,(0.001\,\text{Da})^{-0.5}$$

Where, Da is the austenite grain size in μm.

Figure 5 demonstrates the variation on yield strength as a function of distance across the caster length. Incorporating the effect of these detailed information in the constitutive relation enable us to have a better understanding of deformation behaviour of a material during rolling, and thereby facilitating us to have more accurate prediction of the design set points of rolling operation (roll pass design, rolling temperature etc.)

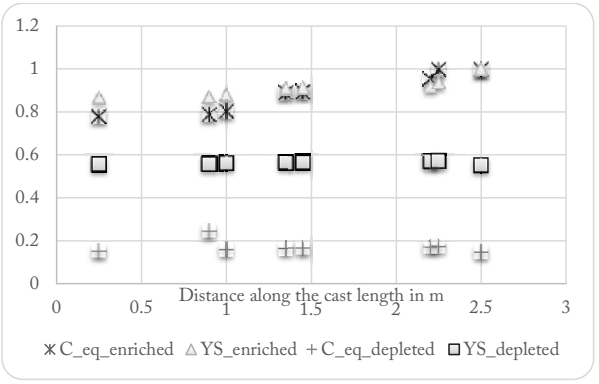

Figure 5. Variation of yield strength (YS) as a function of carbon equivalent and along distance of the cast. All values are normalized.

Closing Remarks

In current work, we have discussed the importance of vertical-horizontal integration of models (an ICME approach) in enabling rapid process scale-up of mill products and the challenges involved in developing models in ICME framework. We have illustrated, using two examples, how these challenges can be addressed. In first example, we talk about integration of various models to obtain information on precipitates, which is used to identify the design set points of reheating operation that will lead to meeting the specified requirements on final sheet. In second example, we talk about integration of micro and macro-segregation information into the constitutive relations to have a better understanding of deformation behaviour of a material during rolling, thereby designing the rolling operation to obtain the microstructure that will lead to attainment of desired sheet properties.

This study presented a methodology for bringing in different processes at different length scales and across different processes. Determining the properties of materials requires a holistic view and is always not a function of a single process alone but the manufacturing route that has been chosen. It is also brought forth that there is a scarcity of models to predict the entire gamut of information. A model which is well established for a particular process may lose its capability when plugged in an integrated framework. This dearth in the model capabilities was put forth in the examples elucidated. The example of sheet manufacturing was chosen to showcase the depth of information required in building integrative models in an ICME based framework. However, this alone is not sufficient, as the interlinking between multiscale modelling and through process modelling requires knowledge up to the atomistic length scales and their effect on large scale grain growth mechanisms. This also stresses how the underlying microstructure decides the properties of a material. A newer methodology proposed by Akash et al. [17] showcases the need for a data science driven approach. This approach elucidates the need to deduce a structure-property relationship to relate and quantify microstructural features with macro scale parameters. This linkage would prove more valuable in passing efficient process parameter information to the subsequent unit operations. George Box is reputed to have observed that all models are wrong and some are useful. The computational models that we use always have some uncertainty associated with them. Going forward, we need to identify solutions which are insensitive to the uncertainties associated with the models.

Acknowledgments

The authors thank TRDDC, Tata Consultancy Services, Pune for supporting this work.

References

1. Nath N.K., Mandal K., Singh A.K., Basu B., Bhanu C., Kumar S., and Ghosh A., 2006, "Ladle furnace on-line reckoner for prediction and control of steel temperature and composition", *Iron and Steelmaking*, Vol. 33 (2), pp. 140-150.
2. Zhang L. and Thomas B.G., 2002, "Inclusion nucleation, growth and mixing during steel deoxidation", *UIUC, Continuous Casting Report No. 200206*, pp. 1-19.
3. Anapagaddi R., Shukla R., Mangal S., and Singh A. K., 2013, "Exploring the design space of a continuous casting tundish for improved inclusion removal and reduced dead volume", Proceedings of the *International Conference on Science and Technology of Ironmaking and Steelmaking*, CSIR - National Metallurgical Laboratory, Jamshedpur.
4. Turkdogan E.T., 1996, Fundamentals of Steelmaking, Institute of Materials, ISBN 0901716804, 9780901716804.
5. Andersson M., Hallberg M., Jonsson L., and Jönsson P., 2002, "Slag-slag-metal reactions during ladle treatment with focus on desulphurisation", *Ironmaking & Steelmaking,* Vol. 29, Issue 3, pp. 224-232.
6. Mayer F., Wu M., and Ludwig A., 2010, "On the formation of centreline segregation in continuous slab casting of steel due to bulging and/or feeding", *Steel Research Int.*, Vol. 81, No. 8, pp. 660-667.
7. Shukla R., Goyal S., Singh A.K., Allen J.K., Panchal J.H., and Mistree F., 2014."An approach to robust process design for continuous casting of slab". *International Design Engineering Technical Conferences & Computers and Information in Engineering Conference IDETC/CIE 2014*, Buffalo, New York Paper Number DETC2014 34208.
8. Flood S.C., and Hunt J.D., 1987, "Columnar and equiaxed growth: Equiaxed growth ahead of a columnar front", *Journal of Crystal Growth*, Vol. 82, pp. 552-560.
9. Pudar M., Zamberger S., Spiradek-Hahn K., Radis R. and Kozeschnik E., 2010, "Computational analysis of precipitation during continuous casting of micro-alloyed steel", *Steel Research*

International, Volume 81, Issue 5, pp. 372-380.
10. Ghosh A., 2000, Secondary Steelmaking: Principles and Applications, CRC Press, ISBN 9780849302640 - CAT# 0264.
11. Shukla R., Kulkarni N., Gautham B.P., Singh A.K., Allen J.K., Panchal J.H., and Mistree F., 2015, "Design exploration of engineered materials, products and its associated manufacturing processes", *JOM*, Vol. 67 (1), pp. 94-107.
12. Bryan Z.L. and Manuel M.V., 2015, "Concurrent integration of science-based mechanistic relationships with computational thermodynamics and kinetic simulations for strengthening magnesium alloys at elevated temperatures", *JOM*, Vol. 67 (1), pp. 179-185.
13. Salajegheh N., Prasannavenkatesan R., McDowell D.L., Olson G.B., and Jou H.J., 2014, "Finite element simulation of shielding/intensification effects of primary inclusion clusters in high strength steels under fatigue loading", *Journal of Engineering Materials and Technology,* Vol. 136 / 031003, pp. 1-8.
14. Gupta A., Goyal S., Padmanabhan K.A., and Singh A.K., 2014, "Inclusions in steel: micro–macro modelling approach to analyse the effects of inclusions on the properties of steel", *The International Journal of Advanced Manufacturing Technology,* DOI: 10.1007/s00170-014-6464-5
15. Luo C., 2001, "Modelling the behaviour of inclusions in plastic deformation of steels", PhD Thesis, Division of Materials Forming, Department of Production Engineering, Royal Institute of Technology, ISSN 1650-1888.
16. Pietrzyk M., Lenard J.G., and Cser L., 1999, Mathematical and physical simulation of the properties of hot rolled products, *Elsevier* , Amsterdam, pp.73-75.
17. Gupta A., Cecen A., Goyal S., Singh A.K., and Kalidindi S.R., 2013, "Multiscale model for non-metallic inclusions/ steel composite system using data science enabled structure-property linkages", *2nd Congress on Integrated Computational Materials Engineering,* TMS, pp. 57-62.

3rd World Congress on Integrated Computational Materials Engineering (ICME 2015)
Edited by: Warren Poole, Steve Christensen, Surya R. Kalidindi, Alan Luo, Jonathan D. Madison, Dierk Raabe, and Xin Sun
TMS (The Minerals, Metals & Materials Society), 2015

FINITE ELEMENT MODEL FOR PLYMOUTH TUBE PROCESSING USING INTERNAL STATE VARIABLES

Heechen Cho[1], Mark F. Horstemeyer[1,2], Youssef Hammi[1], David K. Francis[1]

[1]Center for Advanced Vehicular Systems, Mississippi State University;
200 Research Blvd. Starkville, MS 39759, USA
[2]Mechanical Engineering Departement, Mississippi State University;
206 Carpenter Bldg., P.O. Box ME, Mississippi State, MS 39762, USA;

Keywords: ISV, history, tubing, steel 1010

Abstract

The complete manufacturing process of cold drawn welded steel tubing was simulated using a history dependent internal state variable plasticity-damage model. In order to implement the history dependent model, the Internal State Variables (ISV) Plasticity-Damage (DMG) model that has been developed at Sandia National Labs and Mississippi State University was employed for a low carbon steel AISI 1010, which is the alloy used by the partnering tube manufacturing company. Even though the model is performed at the structural scale, the history variables (internal state variables) which are driven by microstructural changes—e.g., dislocation density and grain size—were tracked through the whole sequences, and the history model captured real thermal and mechanical behaviors of the target material. Once the internal state variables were extracted from the simulation, the model showed critical deformation histories that one could not notice with the naked eye, and must therefore be considered for future design of the tubing process.

Introduction

Manufacturing process of cold drawn welded steel tubing of Plymouth Tube Company (PTC) can be broken down into eleven steps. However, in these steps, Forming, Sizing, Normalizing and Drawing are the pertinent ones to affect thermo-mechanical properties. For this reason, this study focused on these four major steps. The MSU DMG ISV model is based on the ISV plasticity formulation of Bammann [1993]. This model was enhanced by the addition of the void nucleation, growth, and coalescence terms that are related to the damage evolution [Horstemeyer & Bammann, 2010]. This model, implemented into the finite element code Abaqus, was used for simulations of diverse structural analysis. In this simulation study, the ISV model was the first ever history dependent modeling for tube manufacturing.
The ISV model has been developed over the last 30 years. This material modeling method can carry a material's mechanical and thermo-mechanical history, which affects the permanently deformed material behavior. Capturing the material history is very critical to accurately characterize mechanical behavior, especially in sequential processing of materials such as tubing. Non-observable state variables (internal state variables) that are related to microstructural change—such as dislocations, plastic spin, and torsional softening—arising from microstructural rearrangement or anisotropy will immediately affect the next mechanical/thermo-mechanical

step in a sequence. Stress-strain behaviors at varying strain rates or stress states (e.g. tension followed by compression or vice versa) are not captured in any empirically-based models. Because ISV modeling is based on the non-observable state variables and is able to carry history, it is also possible to predict mechanical changes such as failure and fracture by modeling damage. [Bammann, 1990] Deformation history coming from sequential processes is especially difficult to capture due to complicated boundary conditions. Clearly, to have a model with historical capabilities, the history of variables should be transferred to next steps continuously in the model. Currently, only ISV theory can address the prediction of desired properties because of the ability to capture history effects.

Model Description

In order to model the sequential processing steps of materials, the history dependence of the stresses, strains, and microstructural contents must be included to capture high fidelity solutions [Horstemeyer & Wang, 2003]. Key to the modeling and simulation of the sequential processes is the constitutive model. One modeling framework that can capture history dependence is MSU DMG ISV model, which is based upon multiscale material modeling, even though only macroscale was considered in this study. The viscoplasticity model formulated by Bammann *et al.* [1993] coupled with the damage model of Horstemeyer [2012], called DMG-Plasticity model, is used in this work to describe the nonlinear response of the material behavior. The thermo-viscoplastic constitutive equations are developed in the framework of the classical thermodynamics of irreversible processes.

The hyperbolic sine functional form defines the plastic flow rule

$$\boldsymbol{D^p} = \begin{cases} f(T)\sinh\left[\dfrac{|\boldsymbol{s}-\boldsymbol{\alpha}| - [\kappa + Y(T)](1-\phi)}{(1-\phi)V(T)}\right]\boldsymbol{n} & \text{if } \|\boldsymbol{s}-\boldsymbol{\alpha}\| - \kappa - Y(T) \geq 0 \\ 0 & \text{if } \|\boldsymbol{s}-\boldsymbol{\alpha}\| - \kappa - Y(T) < 0 \end{cases}, \quad (1)$$

where ϕ is the total damage, $\boldsymbol{s}$ the deviatoric Cauchy stress, and $\boldsymbol{n}$ the plastic normal tensor defined as

$$\boldsymbol{n} = \frac{3}{2}\frac{\boldsymbol{s}-\boldsymbol{\alpha}}{\|\boldsymbol{s}-\boldsymbol{\alpha}\|}. \quad (2)$$

The function Y(T) is the rate-independent yield stress, the function $f(T)$ determines when the rate-dependence affects initial yielding, and the function V(T) determines the magnitude of rate-dependence on yielding. The definition of this plastic flow rule leads to a Mises type yield function defined by

$$f = \|\boldsymbol{s}-\boldsymbol{\alpha}\| - (1-\phi)\left\{\kappa - Y(T) - V(T)\sinh^{-1}\left[\frac{\bar{d}_p}{f(T)}\right]\right\} = 0 \quad (3)$$

The evolution of the plasticity internal state variables is prescribed in the hardening minus recovery format. The hardening may be defined as the increase in yield stress due to plastic deformation. For hardening materials, the yield surface will evolve in space in one of three ways. The first form of yield surface evolution is called isotropic hardening (the scalar variable), κ, which reflects the effect of the global dislocation density. Secondly, the next yield surface origin can move in stress space, which is called kinematic hardening, $\boldsymbol{\alpha}$. Kinematic hardening captures the Bauschinger effect, which also reflects the effect of anisotropic dislocation density. The third type of yield surface evolution is a mixed hardening where both isotropic and kinematic hardening characteristics are evident. The mixed hardening model is likely the most accurate

among three cases. The thermodynamic force conjugate to the kinematic hardening internal state variable, $\boldsymbol{\alpha}$, representing the directional hardening, is defined by the evolution equation

$$\dot{\boldsymbol{\alpha}} = \left[h(T)\boldsymbol{D}^p - \left[r_d(T)\bar{d}_p + r_s(T)\right]\|\boldsymbol{\alpha}\|\boldsymbol{\alpha}\right]\left(\frac{DCS_0}{DCS}\right)^z, \tag{4}$$

and the isotropic hardening κ by

$$\dot{\kappa} = \left[H(T)\bar{d}_p - \left[R_d(T)\,\bar{d}_p + R_s(T)\right]\kappa^2\right]\left(\frac{DCS_0}{DCS}\right)^z, \tag{5}$$

where

$$\bar{d}_p = \sqrt{\frac{2}{3}\boldsymbol{D}^p{:}\,\boldsymbol{D}^p} \quad \text{and} \quad \|\boldsymbol{\alpha}\| = \sqrt{\frac{3}{2}\boldsymbol{\alpha}{:}\,\boldsymbol{\alpha}} \tag{6}$$

The terms $r_s(T)$ and $R_s(T)$ are scalar functions describing the diffusion-controlled static or thermal recovery, and $r_d(T)$ and $R_d(T)$ are the functions describing the dynamic recovery. The deviatoric stress $\boldsymbol{s}$ is $\boldsymbol{s} = \boldsymbol{\sigma} - I_1\mathbf{1}$ where $I_1 = \mathrm{tr}(\boldsymbol{\sigma})$.

For materials to have a desired shape and mechanical properties, the material has to be softened in order to be drawn and and obtain customized mechanical properties. These processes are called normalization or annealing. In this study, the tube material is subjected to two normalizing processes which happen before first drawing and after second drawing. During the normalizing, recovery, recrystallization, and grain growth phenomena occur due to heating, so that the material's strength is reduced and has higher ductility. A time- and temperature-dependent grain size evolution equation was employed to capture these softening phenomena [Kwon Y.S. et al., 2004]. For the temperature dependency, the Arrhenius type equation was utilized while the rate equation of grain size evolution relates to the time variable. The equation is expressed as

$$\dot{DCS} = \frac{g_a \exp\left(-\frac{g_b}{g_c T}\right)}{DCS^2}, \tag{7}$$

where DCS is the dendrite cell size or grain size, g_a, g_b, and g_c the material constants determined by calibration, and T is the temperature. The time and temperature dependency of grain size change is critical to see how duration and temperature conditions of the annealing process affect softening.

Simulation Setups / Results

Every simulation was run with only a unique set of material constants that was determined before the first process. These material constants were calibrated by using the DMG-Fit software (Figure 1) that was developed at the Center for Advanced Vehicular Systems (CAVS) at Mississippi State University. The material in the simulated tube manufacturing process was AISI 1010 since that is one of the alloys currently used at PTC. To include a temperature-dependent step called annealing, tension experiments were performed at room temperature (298 K) and at high temperature (623 K, 662 F). Since this study was limited to plasticity, the damage part was excluded as one can see in the Figure 1. The specimen used for mechanical testing calibration was the raw sheet material that was fed into the first sequence (forming). The material parameters and the calibrated model constants are given in the Tables 1 and 2, respectively.

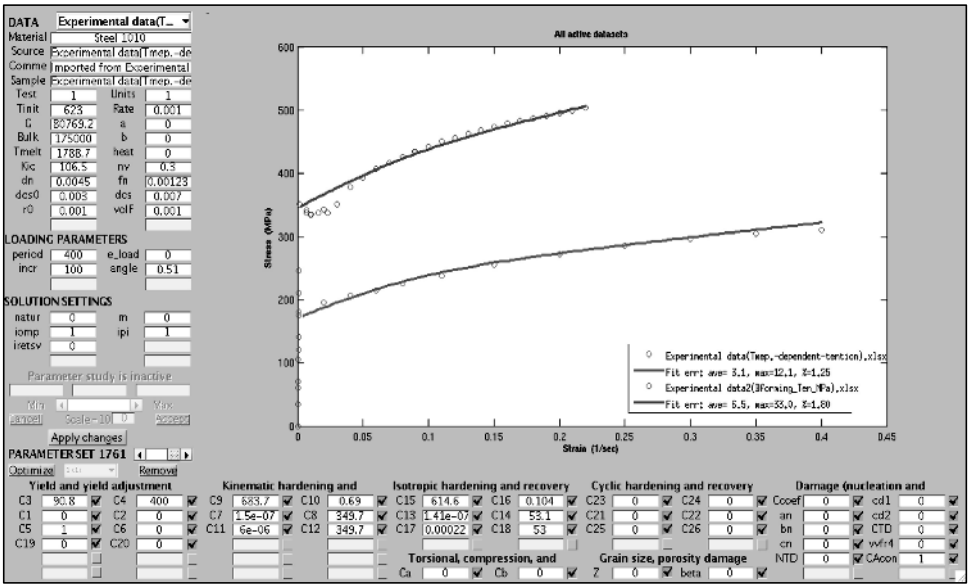

Figure 1 Material constants calibration using DMG fit routine. The dotted line is from tension tests, and the red line is model plot for data at room temperature while the blue line is for high temperature (623 K)

Due to the experimental uncertainty in the mechanical response, in the simulations, the maximum and the minimum (bounded) values of each ISV following the end of a simulation were transferred to the next simulation as upper bound and lower bound, respectively. Also, following each simulation, a tension test simulation using a single 3D element was run, and the stress-strain result from the simulation was compared to experimental data of the corresponding step.

The tubing processes were sequentially modeled in eventual separate steps. In the PTC facility, tubes are physically cut at the end of some steps before being transferred to the next step. Thus it is completely realistic to simulate processing steps separately with different boundary conditions and initial conditions while inheriting the ISV values.

At the end of each step, the ISV material solution is averaged and used as initial material condition in the following step. In other words, the isotropic and kinematic hardenings are initialized based to the material solution of the previous state. All tubing processes, except normalization, is deformed by rigid bodies such as forming rollers, dies, and mandrels in the drawing bench. For the simulations to be realistic as much as possible, the external geometry of contact surfaces of every tool deforming the steel 1010 was used.

ISV Plasticity-Damage Model Calibration and Validation

Using the DMG-Fit software, the ISV material set of constants was fit to the stress-strain experimental curves at varying temperatures. The FEA tension simulation with the fitted material constants using Abaqus outputs exactly same curves as the calibrated curves. Since the material constants were validated, the set of constants had been used for whole sequential simulations of tubing.

Simulations of Forming and Sizing Processes

In this tube forming simulation, the flat material (from raw steel coil) is traveling through several rollers that will force the flat sheet to bend in order to form a tube shape (Figure 2). All sets of rollers were assumed rigid and represented by analytical surfaces that pivoted around reference points. The boundary conditions were set to:

- Rollers: free to rotate on only one axis (z-axis or y-axis);
- Material Velocity: 30 inch/sec (0.76 m/sec) moving in x direction;
- Coefficient of friction: 0.05

The continuum element is available in Abaqus/Explicit only with reduced integration (C3D8R). Multiple elements through the thickness were used to remove the hourglass effect and model the bending response accurately. The number of elements used was 19,294. Figure 2 shows the von Mises stress in forming simulation, at different moments of the analysis, starting from the flat sheet state to the final tube shape. One can observe that both the Mises stress and the plastic equivalent strain are not uniform along the circumference of the tube. The simulation was validated by comparing the post-forming stress-strain behavior with the experimental results (Figure 3(a)). For sizing simulation to have the material history from the previous step, the isotropic and kinematic hardening solutions were uniformly initialized in the whole tube mesh via the user material subroutine VUMAT. Thanks to the history variables from forming, sizing simulations could capture empirical data accurately (Figure 3(b)).

Simulations of Normalizing Process

In normalizing, the tube undergoes a heat treatment process to decrease strength and increase ductility. The desired tube properties are directly influenced by the combination of temperature and time in the furnace. The heating process affects the microstructures (e.g. grain size and dislocations). To capture thermal and time dependent changes of the material, the ISV model

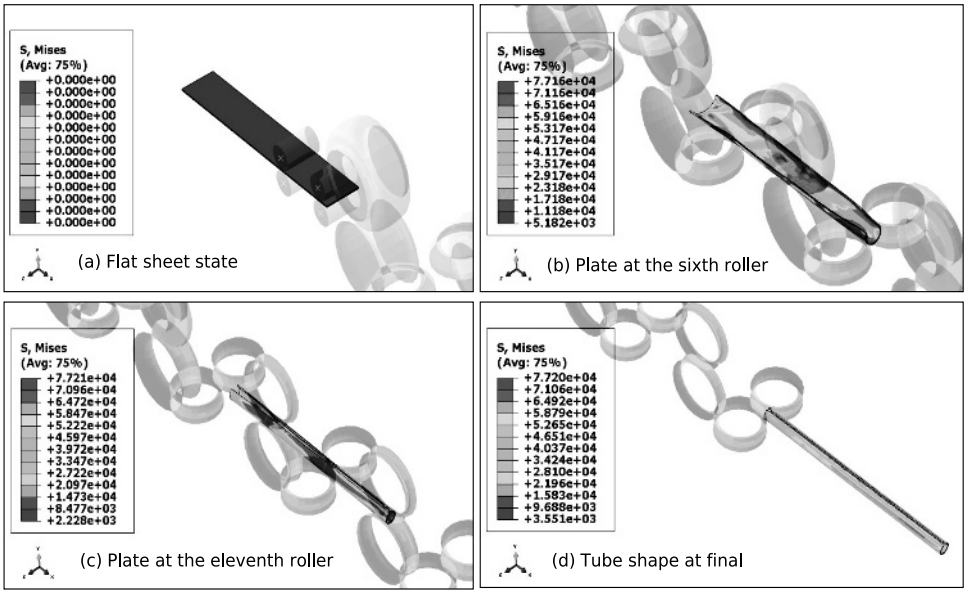

Figure 2 Tube forming simulation showing the von Mises stress (in psi) progression from sheet to tube.

contains static recovery terms in both hardening variables. Here, the static recoveries were basically employed to include the creep behavior of the solid material caused by dislocation climb. However, even though the dislocation climb phenomenon can be numerically captured by the static recovery terms, the recrystallization of grains overwhelmingly softens the tube material compared to dislocation climb, therefore the recrystallization model was definitely needed. Hence, a time-and temperature-dependent grain size evolution rate formulation as expressed in Equation (7) was used. The simulation was performed in Abaqus/Standard with the user material subroutine UMAT. The tube is meshed with coupled temperature-displacement solid elements C3D8RT and the boundary conditions are as following:

- Tube: Stationary;
- Ramping up to 1200 K (1700 F) – 10 minutes;
- Holding to 1200 K – 10 minutes;
- Cooling down to 298 K – 10 minutes.

Since the tube was not constrained at both ends, the stresses are near zero in the tube. High temperature during normalizing was modifying the microstructures of the material, and their evolution could be captured by the hardening variables and the grain size dependent yield stress (Figure 3(c)). As the stress-strain curve showed softening, large amount of softening had indeed occurred in the isotropic hardening variable. In order to connect internal state variables, the final hardening values were initialized to the initial point of the next simulations: drawings.

Simulations of Drawing Processes

The objective of the tube drawing process is to resize the tube by shrinking a large diameter tube into a smaller one through a die. The mandrel and the die were represented by rigid surfaces. The tube was drawn to reduce 20% in OD and thickness compared to initial dimension during the first drawing step. The second drawing step shrank 50% in OD compared to initial dimension. The following boundary conditions were applied:

- Tube: x-direction moving (front part of tube);
- Die and Mandrel: fixed components (encastred);
- Material Velocity: 33.24 inch/sec (0.84 m/sec);
- Friction coefficient: 0.34.

Although this tube is not a thin-walled structure, the shell element (plane stress) showed the more accuracy compared to experimental data than the solid element. Hence, the shell element with reduced integration (S4R) was utilized for those two drawing simulations. Drawing processes were simulated by using Abaqus/Explicit with VUMAT in order to enhance capturing ability under the dynamic boundary conditions. First drawing could be captured accurately while the second drawing simulation over-predicted the ultimate stress in the stress-strain curve (Figure 3(d), 3(e)). Even though the tube is highly deformed compared to the first drawing, the experimental stress-strain curve shows that it has not hardened severely. Saturated hardening could cause this effect or dynamic recrystallization could be the reason too. Further research is needed to investigate this phenomenon. In order to connect history variables, the final hardening values were initialized to the initial point of the next simulation: final annealing.

Simulations of Final Annealing

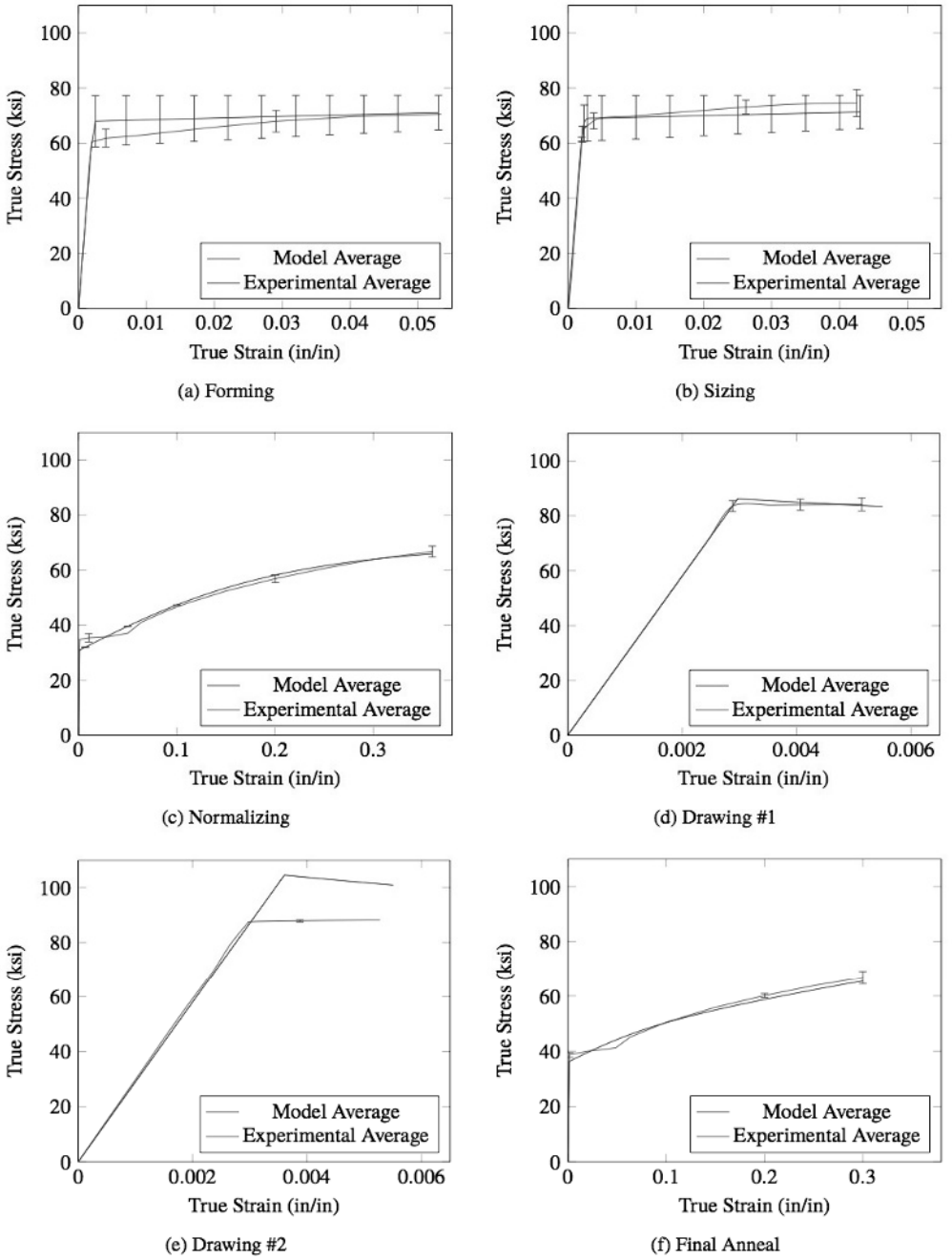

Figure 3 Stress-strain behavior comparison between simulation and experimental result (tension) after each step

Final annealing process has exactly the same boundary conditions as normalizing prior to drawings. The only difference is the material's initial mechanical state. Therefore, the same simulation as normalizing had been performed with different initialized history variables' values and different grain size evolution. This simulation was validated by comparison with experimental stress-strain behavior after annealing process. (Figure 3(f)) Even though the second drawing was somewhat over-predicted and transferred high hardening values to this simulation, since hardenings were softened completely by heat, remaining amount of hardening values could not play an important role in determining post stress-strain curve.

Conclusions

Finite element simulations captured most of the sequences of the thermomechanical tubing processes. Two history variables (isotropic and kinematic hardenings) that are characteristics of the DMG ISV model contributed to link every sequence thermomechanically, which shows that the DMG ISV model can perform material modeling at sophisticated level. As a result of carrying these history variables, most sequences could be predicted using only one set of material model constants without any new fittings through the steps. Through this history dependent model, unobservable and inherent changes in a certain material can be tracked and it provides some critical information in terms of mechanical properties. The information gained from the simulation-based approach with ISVs will allow for optimizing the manufacturing method.

References

Bammann, D.J., Chiesa, M.L., Horstemeyer, M.F., and Weingarten, L.I., (1993), "Failure in Ductile Materials Using Finite Element Methods," eds. N. Jones and T. Weirzbicki, Structural Crashworthiness and Failure, Applied Science, pp.1-54

Bammann, D.J., (1990), "Modeling temperature and strain rate dependent large of metals", *Applied Mechanics Reviews,* Vol.1, pp.312-318

Horstemeyer, M.F., Bammann, D.J., (2010), "Historical review of internal state variable theory for inelasticity", *International Journal of Plasticity*, Vol. 26, pp.1310-1334

Horstemeyer, M.F., Wang, P., (2003), "Cradle-to-grave simulation-based design incorporating multiscale microstructure-property modeling: reinvigorating design with science", *Journal of Computer-Aided Materials Design*, Vol. 10, pp. 13-34

Horstemeyer, M.F., (2012), "Integrated Computational Materials Engineering (ICME): Using Multiscale Modeling to Invigorate Engineering Design with Science", *Wiley Press*

Kwon, Y.S., Wu, Y., Suri, P., Germain, R.M., (2004), "Simulation of the sintering densification and shrinkage behavior of powder-injection-molded 17-4 PH stainless steel", *Metallurgical and Materials Transactions A*, Vol. 35A, pp.257-263

3rd World Congress on Integrated Computational Materials Engineering (ICME 2015)
Edited by: Warren Poole, Steve Christensen, Surya R. Kalidindi, Alan Luo, Jonathan D. Madison, Dierk Raabe, and Xin Sun
TMS (The Minerals, Metals & Materials Society), 2015

AB-INITIO CALCULATION OF SOLUTE EFFECTS ON AUSTENITE GRAIN BOUNDARY PROPERTIES IN STEEL

Michael Hoerner[1], Mark Eberhart[2], John Speer[1]

[1]Colorado School of Mines; Department of Metallurgical and Materials Engineering, 1500 Illinois Street, Golden, Colorado 80401, USA
[2]Colorado School of Mines; Department of Chemistry and Geochemistry, 1500 Illinois Street, Golden, Colorado 80401, USA

Keywords: Austenite, Grain Boundary, Simulation, Solute Drag, Steel

Abstract

Ab-initio density functional theory calculations have been performed to determine the effect of solutes including Cr, Ni, Mo, and Mn on the boundary energy for a variety of coincident site lattice grain boundaries of FCC iron (austenite). The boundaries investigated were of tilt character and both symmetric and asymmetric boundary planes were investigated. Boundary energies were determined for boundaries in pure Fe and for boundaries with single solute atoms at a variety of sites in each boundary. The results are compared to Arrhenius type equations developed from experimental work in the literature and used to hypothesize a mechanistic model for the effects of solutes on boundary mobility based upon the thermodynamic and kinetic effects of solutes at austenite grain boundaries. The predictive capabilities of atomic configurations and bond structures are evaluated and areas for future work are identified. This work provides a new framework for understanding the effects of solutes on atomic scale grain boundary energies and solute drag effects on boundaries.

1. Introduction

Solute drag is an established phenomenon in a variety of materials systems and is reported to have a substantial effect on grain boundary mobility [1-9]. For this reason there have been substantial efforts to model and understand the origin of solute drag as well as attempts to measure and predict solute drag from an experimental standpoint. Currently there are two types of models, theoretical models based upon classic thermodynamics and kinetics and computational models using kinetic Monte Carlo simulations. A brief overview of these models is presented in Section 1.1. Researchers have also approached solute drag experimentally by developing empirical models to describe the expected effect that solutes have on grain boundary mobility. A brief description of some of this work in FCC Fe is presented in Section 1.2.

1.1 Models of Solute Drag

Theoretical models based on classical kinetics follow continuum theory and assume a continuous solute concentration gradient at the grain boundary. These models calculate a drag force on the grain boundary due to the solute concentration profile at the boundary and rely on long range diffusion. An impurity flux model for a moving boundary was presented by Cahn [10] and independently by Lücke and Stüwe [11] and is known as the Cahn-Lücke-Stüwe model which, in steady state, is:

$$D\frac{dC}{dx}+\frac{DC}{kT}\frac{dE}{dx}+VC=VC^{\infty} \quad (1)$$

where D is the solute diffusivity, C is the solute concentration, E is the boundary impurity interaction energy, V is the boundary velocity, C^{∞} is the solute concentration away from the boundary, k is the Boltzmann constant, and T is temperature. This model makes a range of assumptions including the assumption of a flat boundary (due to the one dimensional model), no structural effects on boundary migration, a continuum description of the boundary solute interaction, the assumption of an ideal solution, high boundary concentrations of impurities, and only one type of solute [12].

Due to the time involved in solute diffusion and the diffusion length necessary to develop a steady state solute concentration profile it has proved difficult to model the effects of solute drag using molecular dynamics (MD) [12]. Instead kinetic Monte Carlo simulations have been used to study the effect of solute drag using an Ising spin model [13]. These simulations use a square lattice with a binary spin variable where atoms in one grain are assigned one spin and atoms in the other grain have the second spin. Each atom at the boundary is given the opportunity to jump (switch its spin) and the jump is accepted if the jump lowers the total system energy or increases the system energy to an amount below an energy threshold. Otherwise, the jump fails and the atom remains in its current grain. The authors believe that this model gives a qualitative method of studying the impact of solutes on grain boundary motion [13]. Further, their simulations have demonstrated that the CLS model is insufficient to predict the effects of solutes on grain boundary motion and can fail to capture the qualitative features of grain boundary interaction with solutes. However, these models also fail to capture the structural and mechanistic effects of solutes on grain boundary migration and so direct comparison with experimental work is not possible [12].

1.2 Empirical Prior Austenite Grain Size Relationships

There is a rich body of evidence describing the effects of certain solutes on prior austenite grain size [14-16]. Much of this work has been compiled into empirical Arrhenius type equations which describe the expected prior austenite grain size as a function of various solute concentrations and empirical significance constants for each solute. One such model was developed by Lee and Lee [14]:

$$d = 76671exp\left(\frac{-89089 + 3581C + 1211Ni + 1443Cr + 4031Mo}{RT}\right)t^{0.211} \quad (2)$$

where d is the grain diameter in microns, R is the gas constant, T is the temperature in Kelvin, t is the time in seconds, and C, Ni, Cr, and Mo are the concentrations of those elements in the alloy in weight percent. Similar models have been predicted for the effect of manganese in plain carbon-manganese steels [15,16].

2. Procedure

The solute-boundary binding energy is determined in the present work by starting with a simulation of the boundary with a single solute atom a large distance from the boundary so that there are minimal solute-boundary interactions. This is a relative energy that can be used to compare to the energy under conditions where the solute atom is located at binding or unstable sites at the boundary. The solute is then placed at several locations within the boundary to determine the effect of the solute position on the boundary energy. This method of determining the solute-boundary binding energy is used to limit the energetic variation that might be caused by reliance on absolute energy calculations in VASP. By keeping the simulation cell and settings constant and only moving the solute atom, comparative energies can be used and any uncertainty in the absolute energy of the system is removed.

Data have been gathered from simulations of five pure tilt coincident site lattice (CSL) grain boundaries in austenite with a [0 0 1] tilt axis: symmetric and asymmetric Σ5 boundaries, an asymmetric Σ7, and symmetric and asymmetric Σ13 boundaries. Figure 1 shows the structure of the boundaries. The calculations were performed using projector augmented wave (PAW) pseudopotentials and a PBE functional. *K*-point generation was automatic and energy convergence with respect to the *k*-point mesh was verified. CSL boundaries were employed to ensure periodic boundary conditions. A variety of CSLs were employed to provide more general information about the effect of solutes on grain boundaries.

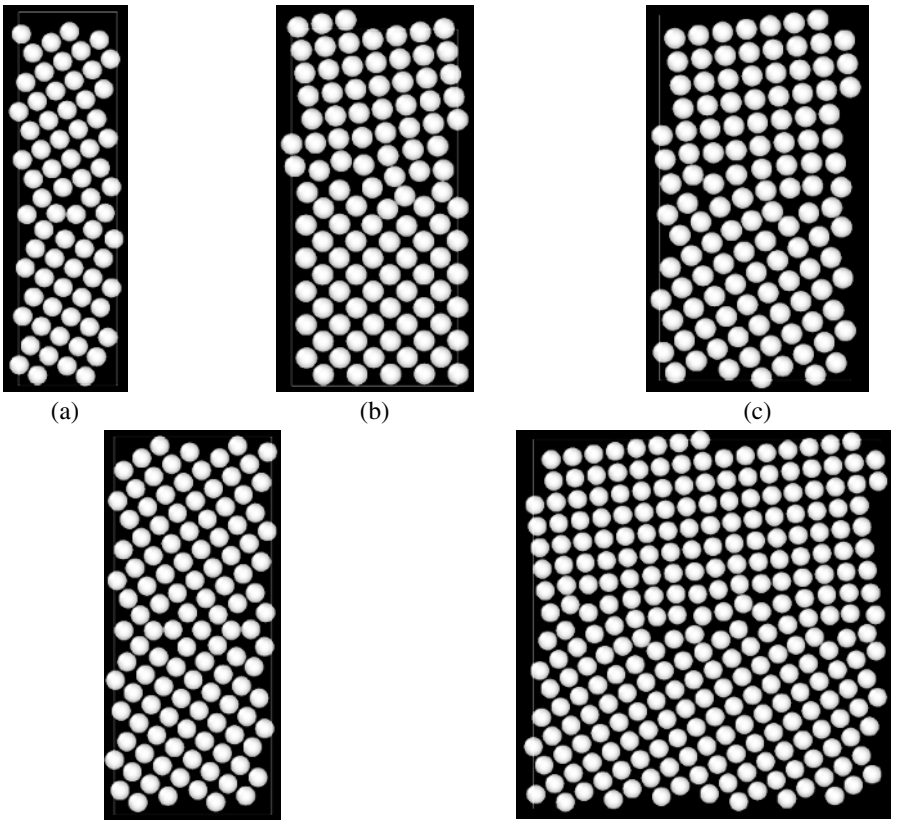

Figure 1. Structures used in simulating prior austenite grain boundaries in VASP. Symmetric (a) and asymmetric (b) Σ5 grain boundaries, an asymmetric Σ7 grain boundary (c), and symmetric (d) and asymmetric (e) Σ13 boundaries. Projections of (0 0 1) planes are shown in the figure.

3. Results

The effects of substitutional solutes on a large number of coincident site lattice tilt grain boundaries have been determined. Multiple positions on each boundary have been investigated and the solute-boundary binding energy determined. These binding energies will be discussed in more detail in section 3.1. Section 3.2 discuses certain sites at the simulated grain boundaries

which display strong (greater than 1 eV) solute-boundary binding energies with Mo and other solutes and will thus be considered preferential substitutional sites (PSS) for solutes. There are also boundary sites displaying strong repulsion to solutes, referred to as unstable sites (US). Significantly, we have found a common bonding motif characteristic of both the negative and positive solute binding energy sites, which is discussed in Section 3.2. Finally, there is a linear correlation between the empirical activation energy constants found by Lee and Lee [14] and the average energy of PSS discussed in Section 3.3.

3.1 Solute-Boundary Binding Energies

Shown in Table 1 are the calculated solute-boundary binding energies for Cr, Mn, Mo, and Ni atoms at twenty locations across five different grain boundaries. All boundaries were found to contain pairs of sites characterized by one site with a large negative binding energy—(PSS)—and an adjacent site with a large positive binding energy—(US). Notably the PSS are always linked by a bond path to US. That is, each maximum binding energy site is adjacent to a site that has a strong repulsion for solutes. There are a large number of sites that demonstrate high binding energies and they appear in both symmetric and asymmetric grain boundaries as well as in boundaries of varying CSL orientation. Similarly, large repulsive energies are observed throughout grain boundaries of different CSL orientation, for both symmetric and asymmetric boundaries. It has been found that the site characteristics can be predicted based on the topology of these sites.

Solute-Boundary Binding Energy (eV)

Grain Boundary	Cr	Mn	Mo	Ni
Σ5 Symmetric	-0.07	-0.01	-0.45	-0.17
	-0.25	**-0.09**	**-1.03**	**-0.09**
	0.07	0.00	0.79	0.05
Σ5 Assymmetric	-0.17	-0.07	-0.94	-0.01
	-0.37	**-0.11**	**-1.74**	**-0.26**
	0.04	0.03	0.07	-0.12
	-0.02	0.00	0.04	-0.12
Σ7 Assymmetric	0.19	0.07	0.97	-0.04
	-0.25	-0.08	-0.71	-0.17
	-0.20	**-0.04**	**-1.04**	**-0.33**
	-0.28	**-0.11**	**-1.29**	**-0.14**
	-0.01	-0.01	0.09	-0.06
	0.07	0.03	0.41	-0.12
Σ13 Symmetric	**-0.30**	**-0.13**	**-1.11**	**-0.04**
	0.11	0.02	1.01	0.09
	-0.24	**-0.09**	**-1.02**	**-0.15**
Σ13 Asymmetric	**-0.31**	**-0.10**	**-1.31**	**-0.23**
	0.09	0.00	0.77	0.12
	0.11	0.02	0.78	0.06
	-0.30	**-0.11**	**-1.35**	**-0.12**

Table 1: Solute-boundary binding energy for Cr, Mn, Mo, and Ni in a variety of boundary sites where the bold energies correspond to confirmed PSS. For comparison, the vacancy formation energy in austenite has been calculated to be between 1.7 and 1.9 eV [17].

3.2 Bonding Motif of High Binding Energy and Repulsive Sites

There is a common bonding motif shared by all PSS and their corresponding US, which, though it varies in subtle detail from boundary to boundary, shows the common bonding topology represented in Figure 2. The PSS is on the right of the Figure (shown independently in Figure 3) and the US are on the left (shown independently in Figure 4). Each PSS is connected by bond paths to five atoms on one side of the site and two atoms sitting at US on the other, giving it an effective coordination number of seven. In turn, the US is characterized by nine bond paths and hence an effective coordination number of nine. In terms of their local coordination and bonding topology, the US is closer to that of the native austenite environment (coordination number of 12) than is the PSS. This suggests that there is an energy distribution across the motif where the atoms surrounding the US (the top and left in Figure 2) are in a lower energy state than the PSS in the center of Figure 2. This energy variation is caused by the local bonding environments of the atoms in these locations.

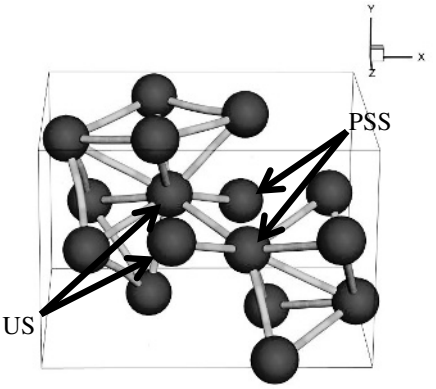

Figure 2. The topology of the adjacent PSS and US. There are two potential US and two potential binding sites (PSS) in this structure because each US is bound to two PSS and vice versa (*color image; refer to PDF version*).

Consistent with these observations, we hypothesize that in a pure Fe system, the environment around the PSS is a high energy structure that is stabilized by pairing with the local structure around the US. It is believed that slight distortions of these two configurations of atoms can stabilize a wide range of grain boundary structures.

While all solutes modeled show preferential substitution on every PSS and are unstable or non-interacting on every US, the energy variations are dramatic, with Mo exhibiting the greatest interactions and having the greatest variation. Initial analysis suggests that this extreme behavior is a consequence of the change in Fe-Fe bonding caused by the Mo substitution. Figure 5 lends support to this observation. Figure 5 shows an US with a Mo atom and the same US containing an Fe atom. Note that the Fe-Fe bond paths in the coordination sphere around the Mo atom are more curved than those in the US coordination sphere around the Fe atom. This kind of bond path curvature is characteristic of "weakened" bonds, with the bonds actually disappearing at some critical curvature [18]. Thus it appears that Mo will tend to be excluded from this site primarily because there are an insufficient number of electrons in this region to support good (neighboring) Fe-Fe bond formation. On the other hand, solutes with more valence electrons than Mo such as Mn and especially Ni, will not affect the Fe-Fe bonding to the same extent—consistent with the reduced binding energies reported in Table 1.

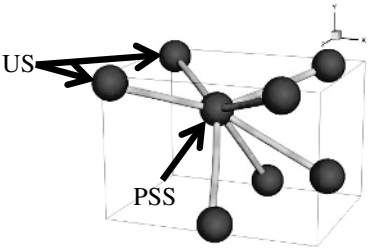

Figure 3. The topology of atomic sites that display high binding energies. The central atom is the PSS (*color image; refer to PDF version*).

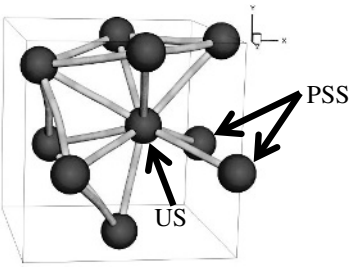

Figure 4. The topology of atomic sites that display instability when occupied by certain solutes. The central atom is the US (*color image; refer to PDF version*).

(a) (b)

Figure 5. The topology of an US containing Mo (a) and pure Fe (b). The bond lines can be seen to curve towards the Mo solute where they remain straight with the Fe, indicating that the Mo is not able to supply enough valence electrons to meet the needs of the local bonding environment (*color image; refer to PDF version*).

3.3 Correlation Between Binding Energies and Empirical Activation Energies

Lee and Lee reported empirically determined activation energies for solute Mo, Ni, and Cr effects on austenite grain growth using an Arrhenius relationship for predicting prior austenite grain size [14]. The activation energies given in Lee were converted from $J/mol * wt\ pct$ to $eV/atom * wt\ pct$ and are plotted in Figure 6 against the average of the solute boundary

binding energy from all preferential solute sites that have been simulated in this work. There is a strong linear relationship between the solute binding energy in the PSS and the empirical activation energy. This implies that the PSS may play an important role in solute drag and may prove useful as a predictor of the effect of untested solutes on austenite grain boundary mobility. Possible ways that these sites might impact boundary migration will be discussed in Section 4.

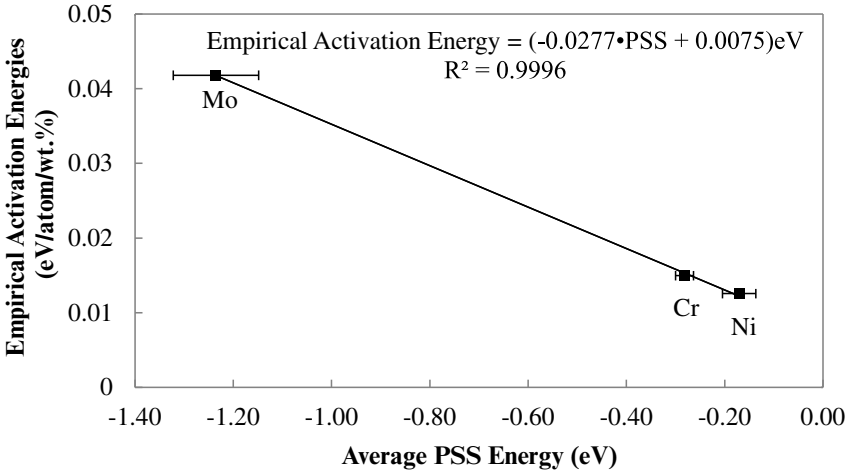

Figure 6. The relationship between the average of solute binding energies for seven preferential solute sites from DFT simulations and the empirically determined activation energies from Lee and Lee [14]. The error bars represent standard error for each solute.

4. Discussion

The linear relationship between the energy of PSS and the empirical activation energies provides strong evidence that these sites impact solute drag in the austenite system. The detailed mechanism by which these sites impact solute drag is currently under investigation but some conclusions can be made with certainty. Since PSS are found adjacent to US, any atomic motion that would require a solute to move from a PSS into an US will cause a significant increase (on the order of 1-2 eV) in the free energy of the system on a local scale. Though the activation energy for such a motion is yet to be determined, the final state would be of a higher energy locally and so the long range driving forces that prompt grain growth would have to be larger to cause such a motion to take place. Thus, it is hypothesized that solutes in these PSS serve to arrest the motion of local sections of grain boundary and thus inhibit boundary mobility. It can also be said that the highly site dependent nature of solute-boundary binding energies requires that the interaction of solutes and boundaries be treated as a discrete quantity and not a continuous function. Further, the local structure of a boundary cannot be ignored. The way in which solute drag is approached in materials will be reconsidered in light of these results.

5. Acknowledgements

The support of the Advanced Steel Processing and Products Research Center and the Office of Naval Research (ONR) Grant No. N00014-10-1-0838 are gratefully acknowledged, as are the contributions of Dr. E. B. Damm of TimkenSteel Corporation.

6. References

1. Y. Mishin, M. Asta, J. Li, "Atomistic Modeling of Interfaces and Their Impact on Microstructure and Properties," *Acta Materialia*, Vol. 58, pp.1117-1151, 2010
2. I. Toda-Caraballo, P. Bristowe, C. Capdevila, "A Molecular Dynamics Study of Grain Boundary Free Energies, Migration Mechanisms and Mobilities in a bcc Fe-20Cr Alloy," *Acta Materialia*, Vol. 60, pp. 1116-1128, 2012
3. A. Lim, M. Haataja, W. Cai, D. Srolovitz, "Stress-Driven Migration of Simple Low-Angle Mixed Grain Boundaries," *Acta Materialia*, Vol. 60, pp. 1395-1407, 2012
4. B. Schonfelder, G. Gottstein, L. Schindlerman, "Comparative Study of Grain-Boundary Migration and Grain-Boundary Self-Diffusion of [0 0 1] Twist-Grain Boundaries in Copper by Atomistic Simulations," *Acta Materialia*, Vol. 53, pp. 1597-1609, 2005
5. R. Godiksen, Z. Trautt, M. Upmanyu, J. Schiotz, D. Jensen, S. Schmidt, "Simulations of Boundary Migration During Recrystallization Using Molecular Dynamics," *Acta Materialia*, Vol. 55, pp. 6383-6391, 2007
6. M. Tonks, Y. Zhang, S. Biner, P. Millett, X. Bai, "Guidance to Design Grain Boundary Mobility Experiments with Molecular Dynamics and Phase-Field Modeling," *Acta Materialia*, Vol. 61, pp. 1373-1382, 2013
7. C. Deng, C. Schuh, "Diffusive-to-Ballistic Transition in Grain Boundary Motion Studied by Atomistic Simulations," *Physical Review B*, Vol. 84, pp. 214102-1 – 214102-10, 2011
8. H. Song, J. Hoyt, "A Molecular Dynamics Simulation Study of the Velocities, Mobility and Activation Energy of an Austentie-Ferrite Interface in Pure Fe," *Acta Materialia*, Vol. 60, pp. 4328-4335, 2012
9. M. Mendelev, C. Deng, C. Schuh, D. Srolovitz, "Comparison of Molecular Dynamics Simulation Methods for the Study of Grain Boundary Migration," *Modelling and Simulation in Materials Science and Engineering*, Vol. 21, 045017 (13pp), 2013
10. J. Cahn, "The Impurity-Drag Effect in Grain Boundary Motion," *Acta Metallurgica*, Vol. 10(9), pp. 789-798, 1962
11. K. Lücke, H. Stüwe, "On the Theory of Grain Boundary Motion," *Recovery and Recrystallization of Metals*, pp. 171-201, 1963
12. M. Mendelev, D. Srolovitz, "Impurity Effects on Grain Boundary Migration," *Modelling and Simulation in Materials Science and Engineering*, Vol. 10, pp. R79-R109, 2002
13. M. Mendelev, D. Srolovitz, W. E, "Grain-Boundary Migration in the Presence of Diffusing Impurities: Simulations and Analytical Models," *Philosophical Magazine A*, Vol. 81 no. 9, pp. 2243-2269, 2001
14. S. Lee, Y. Lee, "Prediction of Austenite Grain Growth During Austenitization of Low Alloy Steels," *Materials and Design*, Vol. 29, pp. 1840-1844, 2008
15. E. Anelli, "Application of Mathematical Modelling to Hot Rolling and Controlled Cooling of Wire Rods and Bars," *ISIJ International*, Vol. 32 no. 3, pp. 440-449, 1992
16. T. Reti, Z. Fried, I. Felde, "Computer Simulation of Steel Quenching Process using a Multi-Phase Transformation Model," *Computational Material Science*, Vol. 22, pp. 261-278, 2001
17. T. Klaver, D. Hepburn, and G. Ackland, "Defect and Solute Properties in Dilute Fe-Cr-Ni Austenitic Alloys From First Principles," *Physical Review B*, Vol. 85, pp. 174111-1-174111-23, 2012.
18. T. Jones, J. Miorelli, M. Eberhart, "Reactive Cluster Model of Metallic Glass," *Journal of Chemical Physics*, Vol. 140, pp. 084501, 2014

3rd World Congress on Integrated Computational Materials Engineering (ICME 2015)
Edited by: Warren Poole, Steve Christensen, Surya R. Kalidindi, Alan Luo, Jonathan D. Madison, Dierk Raabe, and Xin Sun
TMS (The Minerals, Metals & Materials Society), 2015

ICME TOWARDS IMPROVED UNDERSTANDING OF BAINITE IN 100CR6

Wenwen Song, Wolfgang Bleck, Ulrich Prahl

Department of Ferrous Metallurgy, RWTH Aachen University, Germany

Key words: bainite; carbides; atom probe tomography; *ab initio*; phase field model

Abstract

In the design of high strength steels, bainite structures gain importance because of their excellent balance of strength and toughness. However, bainite still remains the least understood austenite decomposition reaction. Following the philosophy of Integrated Computational Materials Engineering (ICME), we combine various simulation and advanced characterization approaches at different length scales in order to improve the scientific understanding of this solid phase transformation. In the present work, bainite transformation in 100Cr6 steel with nano-sized cementite (θ) precipitation within bainitic ferrite (α_B) is analyzed. The bainite transformation was introduced and investigated by TEM, atom probe tomography (APT), phase-field simulations and *ab initio* calculations. APT shows that in lower bainite isothermally held at 260 °C both ε and θ precipitate adopting plate-like shapes and precipitate under para-equilibrium mode. With the help of atom probe concentration data input and para-equilibrium phase diagram calculation using ThermoCalc software, isothermal bainite formation was simulated by means of phase field approach. To simulate the very fine cementite, ultra-small grid spacing, i.e. 2 nm, was applied in the simulation. A faceted model has been coupled in the simulation for both bainitic ferrite (α_B) and cementite (θ) growth. APT showed the high amount of carbon trapped within bainitic ferrite. It is of significant importance to take into account both carbon partitioning and carbon trapping within bainite ferrite in bainite transformation simulations.

Introduction

100Cr6 is a high carbon bearing steel which is widely used in the construction and automotive industry. To meet to the needs of application-required mechanical properties, 100Cr6 is mostly applied in either martensitic and/or bainitic state [1-3]. The bainite exhibits complex microstructures, containing not only the bainitic ferrite matrix but also the 2nd phases, i.e. alloyed carbides, θ-carbide (cementite, Fe_3C), ε-carbide ($Fe_{2.4}C$), etc. [3]. At different bainite formation temperatures, the 2nd phases precipitate from the bainitic ferrite matrix at different locations with the varied shapes, which leads to fairly different mechanical properties of the materials.

In the present work, ε and θ carbide precipitation and elemental partitioning features associated with ε and θ precipitation in both, upper and lower bainite formation, in high carbon bearing steel 100Cr6 were investigated using TEM and Atom Probe Tomography (APT) [3]. *Ab initio* (density-functional) predictions together with quasi-harmonic phonon calculations were further performed in order to assess the thermodynamics associated with ε carbide ($Fe_{2.4}C$) formation and its competition with θ carbide (cementite Fe_3C) precipitation [3]. A faceted model has been coupled in the phase field simulation for both bainitic ferrite (α_B) and cementite (θ) growth. Carbon redistribution across γ/α_B and α_B/θ phase boundaries during bainite transformation is further discussed.

Experimental

The chemical composition of the steel 100Cr6 is given in Table I. The material is mainly alloyed with Cr and microalloyed with Mo. Si and Mn are both at a low level, while the Al content is almost negligible. The N content in the steel is 75 ppm.

Table I. Chemical composition of the investigated steel 100Cr6 (wt.%)

Fe	C	Si	Mn	P	S	Cr	Mo	Ni	Al	Cu	N
Bal.	0.967	0.30	0.23	0.003	<0.001	1.38	0.02	0.07	0.026	0.05	0.0075

In order to study the isothermal bainite transformation, the samples were austenitized at 850 °C for 300 s, followed by rapid cooling to 260 °C and 500 °C at a rate of 55 °C/s. At the isothermal transformation temperature (ITT) of 260 °C, the samples were isothermally held for 2500 s in order to form a lower bainite microstructure. At the isothermal transformation temperature (ITT) of 500 °C the samples were isothermally held for 1200 s in order to form an upper bainite microstructure. The heat-treatment cycles are illustrated in Figure 1. Austenitization and bainitization were performed in a Bähr 805A dilatometer, where the dimension of the specimen was Φ 3 mm×10 mm.

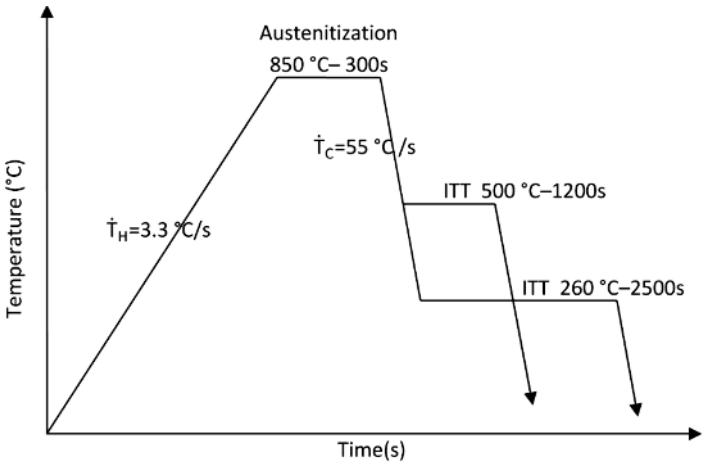

Figure 1. Heat treatment cycle of the investigated steel 100Cr6. (ITT stands for Isothermal Transformation Temperature)

To characterize the bainitic morphology, a Tecnai F20G2 Transmission Electron Microscope with an embedded US1000 Gatan camera was used. TEM foils were prepared from the heat-treated specimen with a twin-jet electro polishing device, using a chemical solution of 10 vol.% perchloric acid and 90 vol.% acetic acid. APT specimens were cut from the heat-treated material and electro-polished with standard electro-polishing methods [4]. APT analyses were performed using a Local Electrode Atom Probe (LEAP 3000X HR, Cameca Instruments) in pulsed voltage mode at a pulse fraction of 15 % and a pulse frequency of 200 kHz. The specimen base temperature was about 60 K [5-7].

Simulation methods

In the phase field simulation, bainitic transformation was assumed to take place under para-equilibrium mode [3]. Only carbon as an interstitial can redistribute by long-range diffusion, whereas substitutional alloy elements, e.g. Si, Mn, Cr, are considered to be frozen in their sublattice. The composition c in $\Delta G(c,T)$ is represented by the local carbon concentration c, which can be gained by coupling phase field equation (1) with carbon diffusion equation. The carbon diffusion is expressed as the sum of the fluxes in the individual grains i and j weighted by the phase field parameters ϕ_i and ϕ_j with $\phi_i + \phi_j = 1$. The fluxes are calculated from the composition gradient and the diffusivity in each grain, D_i^C and D_j^C [8]:

$$\frac{\partial C}{\partial t} = \nabla\left[\phi_i D_i^C \nabla C_i + \phi_j D_j^C \nabla C_j\right] \tag{1}$$

Where C_i and C_j are the carbon concentration in grain i and j, respectively.

The austenite (γ) phase was assumed to be isotropic, which grows identically in all directions. To describe the anisotropic growth of bainitic ferrite and cementite (θ), a faceted model being implemented in MICRESS® was applied. In the model [9], it is assumed that each crystallographic orientation has individual properties, e.g. interfacial energy and interfacial mobility. For each facet type, the interfacial energy is calculated as:

$$\sigma = \sigma_0 \cdot k_{st}^2 \cdot \left(k_{st}^2 \cdot \cos\theta^2 + \sin\theta^2\right)^{-\frac{3}{2}} \tag{2}$$

where σ_0 is the surface energy between two phases; k_{st} is the static anisotropy coefficient of the facet and θ is the misorientation of the normal vector of the interface to the normal vector of the nearest facet.

The interfacial mobility is calculated as the following equation:

$$\mu = \mu_0\left[k_{kin} + (1 - k_{kin}) \cdot \tan\left(\frac{kappa}{\tan\theta}\right) \cdot \frac{\tan\theta}{kappa}\right] \tag{3}$$

where μ_0 is the interfacial kinetic coefficient between two phases, indicating the interface mobility; k_{kin} is the kinetic anisotropy coefficient and θ is the misorientation of the normal vector of the interface to the normal vector of the nearest facet. The parameter *kappa* in the faceted model defines the broadness of the anisotropy function with the value in the range of 0 and 1.

All first-principles electronic-structure calculations were based on density-functional theory [3]. The simulations were performed by using the augmented (PAW) plane-wave approach using the Vienna ab initio Simulation Package [3]. Volume expansions and temperature-dependent thermodynamic properties were evaluated in the framework of the quasi-harmonic approximation, taking into account the electronic ground state and the harmonic vibrational contributions to the Helmholtz free energy for various volumes. The vibrational free energy was fitted as a linear function of the volume in order to reduce calculation time [3].

Results and discussion

TEM and morphology

The bright field TEM image in Figure 2(a) shows lower bainite microstructure in the sample isothermally heat-treated at 260 °C for 2500 s. As shown in Figure 2(a), nano-sized carbides precipitate within bainitic ferrite α_B plates and the particles precipitate with an angle of approximately 60° to the longitudinal direction of bainitic ferrite α_B [3]. The boundaries of the bainitic ferrite α_B subunits are indicated in Figure 2(a) in terms of dashed green lines. The bright field TEM image in Figure 2(b) shows the upper bainite microstructure in the sample isothermally heat-treated at 500 °C for 1200 s [3]. Unlike the plate-like morphology of bainitic ferrite α_B observed in lower bainite it adopts a more lath-type shape in upper bainite. As is shown in Figure 2(b), nano-sized carbides are precipitated between the bainitic ferrite laths in the upper bainite [3]. Several carbides precipitate from the grain boundary (GB) shown at the right bottom of Figure 2(b). The TEM images reveal that the average size of nano-sized carbides in lower bainite is about 30 nm in width and about 80 nm in length, while in upper bainite, the coarsened carbides are even as large as 100 nm in width and 0.5 - 1 μm in length [3].

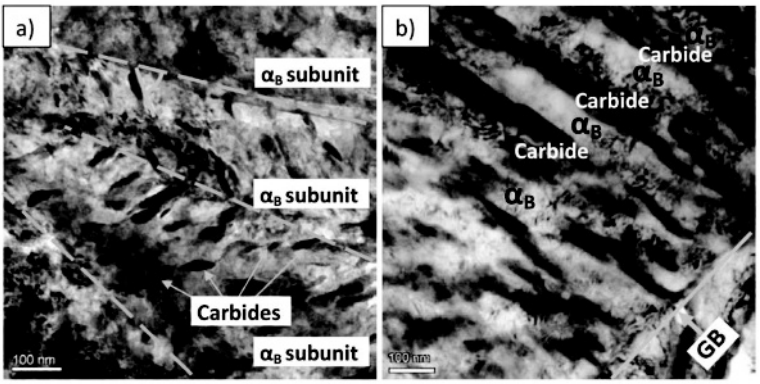

Figure 2. TEM micrographs of 100Cr6 steel (a) lower bainite at 260 °C for 2500 s, (b) upper bainite at 500 °C for 1200 s; α_B: ferrite, θ: cementite and GB: grain boundary. [3]

Atom probe tomography and elemental partitioning

The Atom Probe Tomography (APT) images in Figure 3 shows the 3D carbon atomic map and 1D concentration profiles of lower bainite formed at 260 °C in 100Cr6 steel [3]. A local overview of the carbon distribution in bainitic ferrite matrix and carbides is shown images in Figure 3. The carbon-rich regions correspond to cementite Fe_3C and ε carbide $Fe_{2.4}C$ [3]. The carbon-depleted region represents the bainitic ferrite, which is supersaturated with carbon. The atom probe results indicate the co-existence of ε carbide and Fe_3C precipitation [3].

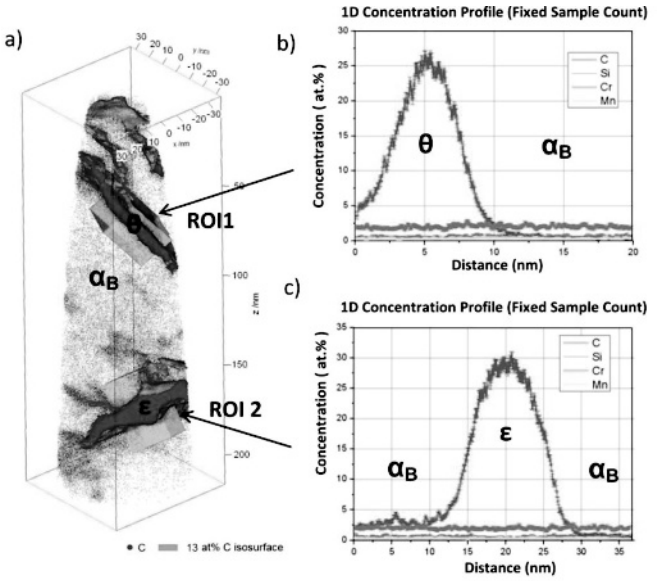

Figure 3. (a) Carbon atomic map and 13 at.% iso-concentration surface in lower bainite in 100Cr6 isothermally heat-treated at 260 °C for 2500 s; 1D concentration profile in ROI1 (b) and ROI2 (c) in Figure 3 (a); α_B: bainitic ferrite, θ: cementite and ε: ε carbide $Fe_{2.4}C$ [3].

Figure 4 displays the 3D carbon atomic map and proxigram profiles of upper bainite formed at 260 °C in 100Cr6 steel. Figure 4(a) shows a local overview of the carbon distribution in bainitic ferrite α_B and cementite (θ) in upper bainite in 100Cr6. The carbon-rich region with a carbon content of about 25 at.% corresponds to cementite (θ) [3]. The carbon-depleted region in the bulk represents bainitic ferrite α_B. Figure 4(b) displays the proxigram of carbon and alloy elements at the interface of bainitic ferrite α_B and cementite (θ) in upper bainite. The proxigram reveals the partitioning characteristics of carbon and alloying elements at the bainitic ferrite (α_B)/cementite (θ) interface [3]. The carbon largely partitions to the austenite during upper bainite formation at 500 °C, which leads to carbide precipitation directly from austenite [3].

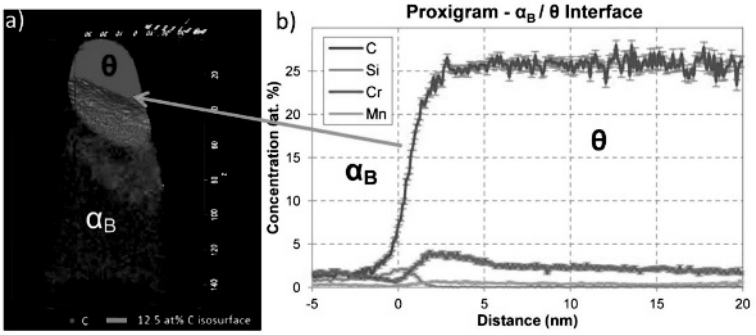

Figure 4. (a) Carbon atomic map and 12.5 at.% iso-concentration surface in upper bainite in 100Cr6 isothermally heat-treated at 500 °C for 1200 s; (b) Proxigram showing carbon and alloy concentrations across bainitic ferrite and cementite (θ) interface; α_B represents bainitic ferrite, θ represents cementite [3].

Ab initio calculation

Figure 5 shows the Gibbs free energy for epsilon carbide ($Fe_{2.4}C$) to cementite (θ) transition reaction as a function of temperature. Positive value of the Gibbs free energy indicates a ε favored region and a negative value indicates a cementite favored regime [3]. The theoretical calculation results reveal that the formation of epsilon carbide $Fe_{2.4}C$ benefits from a ferritic matrix. In bainitic ferrite matrix at 260 °C, the Gibbs energy is about 0.1 kJ/mol only and the formation of θ Fe_3C and ε $Fe_{2.4}C$ have nearly the same probability from a thermodynamic standpoint, whereas in austenitic matrix, the formation of cementite is clearly preferred at any temperature; for example, at 500 °C it is favored by 4 kJ/mol [3]. It further indicates that ε carbide is more prone to precipitate from lower bainite than from upper bainite.

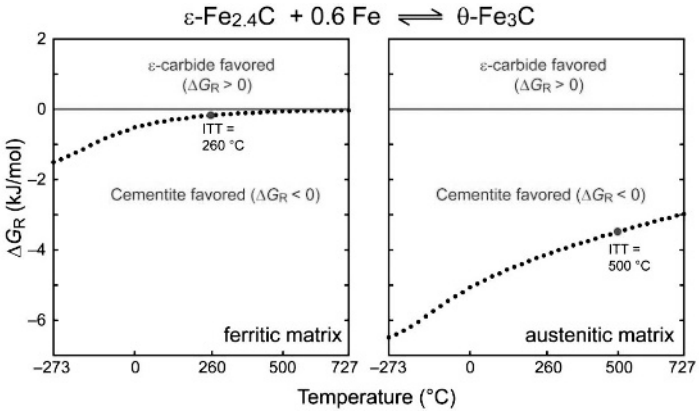

Figure 5. Gibbs free reactions energies between ε-$Fe_{2.4}C$ and cementite (Fe_3C, θ) as a function of temperature in a ferritic (left) and an austenitic matrix (right). Both experimental isothermal transformation temperatures (ITT) are indicated [3].

Phase field simulation

Figure 6 shows the simulated cementite (θ) precipitation in a single lower bainite plate and the corresponding concentration profiles of carbon redistribution at γ/α_B and α_B/θ interfaces during bainitic phase transformation at 260 °C in 100Cr6. In Figure 6(a), cementite (θ) precipitates at an inclination of about 60° with respect to the long axis of the bainitic ferrite (α_B). Figure 6(b) illustrates the carbon concentration profiles along a-b line in Figure 6(a), showing the migrating bainitic ferrite/austenite interface and carbon redistribution behavior during bainitic ferrite thickening at 260 °C. The simulated formation of bainitic ferrite is accompanied with carbon diffusion from the bainitic ferrite nuclei to austenite, while substitutional elements, i.e. Cr, Si, Mn, are frozen in their sublattice. During the growth of bainitic ferrite, the bainitic ferrite exhibits partially carbon supersaturation condition. The trapped carbon composition input is based on our Atom Probe Tomography observations. Figure 6(c) illustrates carbon concentration along c-d line in Figure 6(a), showing the migrating bainitic ferrite/cementite interface and carbon redistribution across the phase boundary during cementite precipitation. Cementite nucleates and precipitates from the bainitic ferrite plate when the minimum local undercooling in bainitic ferrite is achieved for cementite formation.

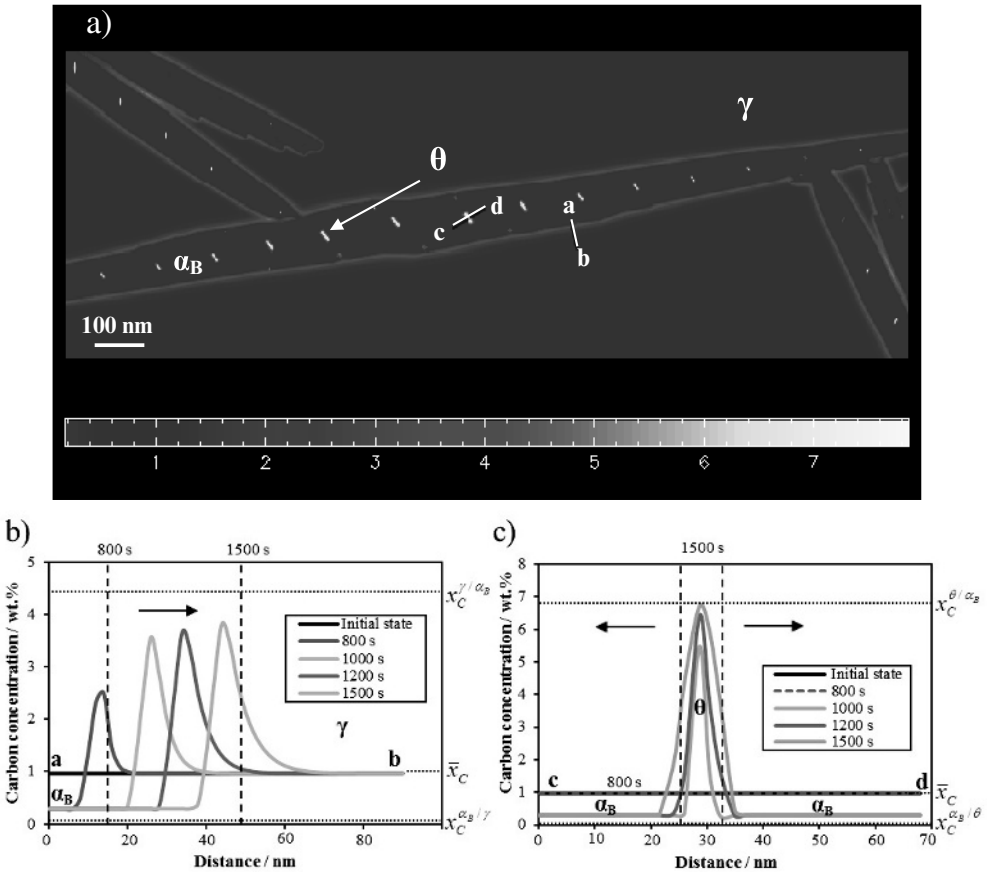

Figure 6. (a) phase field simulated microstructure in 100Cr6 at 260 °C for 1500 s; (b) carbon concentration along a-b line in Figure 6(a) showing the migrating bainitic ferrite/austenite interface and carbon redistribution behavior during bainitic ferrite thickening in bainite formation at 260 °C in 100Cr6; (c) carbon concentration along c-d line in Figure 6(a) showing the migrating bainitic ferrite/cementite interface and carbon redistribution behavior during cementite precipitation in bainite formation at 260 °C in 100Cr6.

Conclusions

In the present work, the nano-sized carbide precipitation features during bainite formation at different temperatures in high carbon steel 100Cr6 were investigated using transmission electron microscopy (TEM), atom probe tomography (APT) in combination with ab initio calculations and phase field simulations. The morphology, type and the elemental partitioning features of the nano precipitates within bainitic microstructures were characterized. Deeper insights into the nano-sized carbide precipitation within bainitic microstructures are achieved. The phase field simulation, showing the simulated results which can be compared against TEM observations and Atom Probe Tomography (APT) analysis at atomic scale, is a powerful and promising tool in material simulations, particularly for the complex bainitic phase transformation.

Acknowledgements

This work has been performed within the Interdisciplinary Centre for Advanced Materials Simulation (ICAMS) at the Ruhr University Bochum. Authors would like to express their appreciations to Dr. Markus Apel and Dr. Bernd Böttger in ACCESS of RWTH Aachen University for the fruitful discussions. ICAMS gratefully acknowledges funding from ThyssenKrupp Steel Europe AG, Bayer Material Science AG, Salzgitter Mannesmann Forschung GmbH, Robert Bosch GmbH, Benteler Steel/tube Management GmbH, Bayer Technology Services GmbH and the state of North Rhine-Westphalia as well as the European Commission in the framework of the European Regional Development Fund (ERDF).

References

[1] A.T.W. Barrow, J.-H. Kang, and P.E.J. Rivera-Díaz-del-Castillo, "The $\epsilon \rightarrow \eta \rightarrow \theta$ transition in 100Cr6 and its effect on mechanical properties," *Acta Materialia*, 60 (6) (2012), 2805-2815.

[2] J.-H. Kang, B. Hosseinkhani, and P.E.J. Rivera-Díaz-del-Castillo, "Rolling contact fatigue in bearings: multiscale overview," *Materials Science and Technology,* 28 (1) (2012), 44-49.

[3] W. Song, J.von Appen, P. Choi, R. Dronskowski, D. Raabe, and W. Bleck, "Atomic-scale investigation of ε and θ precipitates in bainite in 100Cr6 bearing steel by atom probe tomography and *ab initio* calculations," *Acta Materialia*, 61 (20) (2013), 7582–7590.

[4] M.K. Miller, *Atom Probe Tomography: Analysis at the Atomic Level* (New York, NY: Kluwer Academic/Plenum Press, 2000).

[5] J.B. Seol, D. Raabe, P. Choi, Y.R. Im, and C.G. Park, "Atomic scale effects of alloying, partitioning, solute drag and austempering on the mechanical properties of high-carbon bainitic–austenitic TRIP steels," *Acta Materialia*, 60 (17) (2012), 6183-6199.

[6] O. Dmitrieva, D. Ponge, G. Inden, J. Millán, P. Choi, J. Sietsma, and D. Raabe, "Chemical gradients across phase boundaries between martensite and austenite in steel studied by atom probe tomography and simulation," *Acta Materialia*, 59 (1) (2011), 364-374.

[7] E.A. Marquis, P. Choi, F. Danoix, K. Kruska, S. Lozano-Perez, D. Ponge, D. Raabe, and C.A. Williams, "New insights into the atomic-scale structures and behavior of steels," *Microscopy Today*, 20 (04) (2012), 44-48.

[8] K. Nakajima, M. Apel, and I. Steinbach, "The role of carbon diffusion in ferrite on the kinetics of cooperative growth of pearlite: a multi-phase field study," *Acta Materialia*, 54 (14) (2006), 3665-3672.

[9] J. Eiken, "A phase-field model for technical alloy solidification" (Ph.D. thesis, RWTH-Aachen University, 2010).

3rd World Congress on Integrated Computational Materials Engineering (ICME 2015)
Edited by: Warren Poole, Steve Christensen, Surya R. Kalidindi, Alan Luo, Jonathan D. Madison, Dierk Raabe, and Xin Sun
TMS (The Minerals, Metals & Materials Society), 2015

STEEL – *AB INITIO*: QUANTUM MECHANICS GUIDED DESIGN OF NEW Fe-BASED MATERIALS

Wenwen Song, Ulrich Prahl, Wolfgang Bleck

Department of Ferrous Metallurgy, RWTH Aachen University, Aachen, Germany

Keywords: High manganese, strain hardening, mechanism maps

Abstract

This contribution reports the results of the collaborative research unit SFB 761 "Steel - *ab initio*", a cooperative project between RWTH Aachen University and the Max-Planck-Institute for Iron Research in Düsseldorf (MPIE) financed by the German Research Foundation (DFG). For the first time, in a structural measure it is exploited how *ab initio* approaches may lead to a detailed understanding and thus to a specific improvement of the design process for a structural steel. Here, the challenge lies in the combination of abstract natural science theories with rather engineering-like established concepts. Aiming at the technological target of the development of new type of structural materials based Fe-Mn-C and Fe-Mn-Al-C alloys, the combination of *ab initio* and engineering methods is new, but could be followed quite successfully. Three major topics are treated in this research unit: a) development of a new method for material- and process-development based on *ab initio* calculations; b) design of a new class of structural materials with extraordinary property combinations; c) acceleration of development time and reduction of experimental efforts and complexity for material- and process-development. In the present work, the general concept of new material design is presented together with some exemplarily results showing the advantage of this combined scale bridging approach.

Introduction

Fe-Mn-Al-C austenitic steels with superior strain hardening behavior have gained much research interest in the last decades [1-3]. During plastic deformation, the materials develop extraordinary service properties by the deformation mechanisms with high strain hardening potential, i.e. Transformation Induced Plasticity (TRIP) effect, Twinning Induced Plasticity (TWIP) effect and Microband Induced Plasticity (MBIP) effect [4-6]. With the addition of Al, the stacking fault energy (SFE) of the alloy increases. The Al addition promotes the precipitation of the nano-sized kappa phase $(Fe, Mn)_3AlC$ from the austenite matrix in the Fe-Mn-Al-C austenitic alloys [7-9]. The microstructure and the size of the kappa phase are strongly influenced by the aging time and aging temperature, as well as the actual alloy composition [10-11].

In the present work, following the philosophy of Integrated Computational Materials Engineering (ICME), we developed stacking fault energy (SFE) maps for the design of new types of structural materials based on Fe-Mn-C and Fe-Mn-Al-C alloys [7]. Based on the Calphad method and the *ab initio c*alculation input, the 2D&3D SFE maps were calculated in order to study the chemical composition dependent SFE and the deformation mechanisms of high-Mn austenitic steels. The kappa phase formation and the associated ordering features in Fe-Mn-Al-C austenitic steels have been investigated by means of *in situ* synchrotron X-ray diffraction method. The Rietveld refinement technique has been employed to perform the phase analysis on the kappa phase formation in the steel. The contribution of the coherent kappa phase

precipitation to the mechanical property of the material is further discussed.

Deformation Mechanism Maps

Based on the Calphad method and the *ab initio c*alculation input, 2D composition-dependent stacking fault energy (SFE) maps of high-Mn steels in Fe-Mn-C and Fe-Mn-Al-C alloy system were calculated, Figure 1 [7]. The calculation was based on a subregular solution thermodynamics model and the maps were developed by using the Scientific Group Thermodata Europe (SGTE) database [12]. The main assumption in the thermodynamic calculation was to take the SFE (Γ) as the required Gibbs free energy to form a ε martensite platelet with the thickness of two atomic layers within the dense planes [13, 14]. In the model, the stacking fault energy was calculated as follows [15]:

$$\Gamma = 2\rho\Delta G_{eff}^{\gamma\to\varepsilon} + 2\sigma^{\gamma/\varepsilon} \quad (1)$$

where ρ is the molar surface density along the {111} plane, $\sigma^{\gamma/\varepsilon}$ is the γ/ε interfacial energy, $\Delta G_{eff}^{\gamma\to\varepsilon}$ is the effective Gibbs free energy change during the austenite → ε martensite transformation [7]. $\Delta G_{eff}^{\gamma\to\varepsilon}$ consists of two components, the chemical Gibbs free energy change ($\Delta G_{chem}^{\gamma\to\varepsilon}$) and the magnetic Gibbs free energy change ($\Delta G_{mag}^{\gamma\to\varepsilon}$), calculated by the following equations:

$$\Delta G_{eff}^{\gamma\to\varepsilon} = \Delta G_{chem}^{\gamma\to\varepsilon} + \Delta G_{mag}^{\gamma\to\varepsilon} \quad (2)$$

$$\Delta G_{chem}^{\gamma\to\varepsilon} = \left[\sum X_i \Delta G_i^{\gamma\to\varepsilon} + \sum X_i X_j \Delta\Omega_{ij}^{\gamma\to\varepsilon}\right] \quad (3)$$

where X_i is the molar fraction the element *i* in the system and $\Delta G_i^{\gamma\to\varepsilon}$ is the Gibbs free energy change due to ε martensite formation from austenite [7]. $\Delta\Omega_{ij}^{\gamma\to\varepsilon}$ is the interaction energy between the components *i* and *j*.

$$\Delta G_{mag}^{\gamma\to\varepsilon} = RTln\left(1+\frac{\beta^{\varphi}}{\mu_B}\right) f\left(\frac{T}{T_{Néel}^{\varphi}}\right) \quad (4)$$

where β^{φ}, $T_{Néel}^{\varphi}$ and μ_B are the magnetic moment, the Néel temperature of phase φ and the Bohr magneton [7]. The input parameters for the magnetic contributions and the binary interactions of the elements from the Ref. [7] were used and the details refer to the initial discussion on mechanism map development by Saeed-Akbari et al. [16].

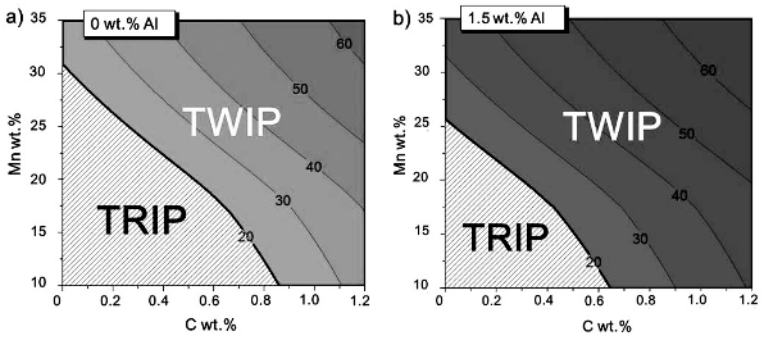

Figure 1. 2D composition-dependent map of stacking fault energy (unit, mJ/m²) at 300 K (a) Fe-Mn-C alloy system (b) Fe-Mn-Al-C alloy system, Al 1.5 wt.% [7].

The deformation mechanisms of high-Mn steels, i.e. TRIP, TWIP, MBIP, are predicted based on the thermodynamic calculation of SFE maps [7]. Figure 2 plots the 3D domain where the kappa carbide precipitates at 873 K. It illustrates the different composition domains with regarding to the different deformation mechanisms [7]. As shown in Figure 2, with the increase of SFE, the deformation mechanism shifts from TRIP to TWIP and further to MBIP. With the addition of Al, kappa carbide $(Fe, Mn)_3AlC$ precipitates in the Fe-Mn-Al-C steels [7].

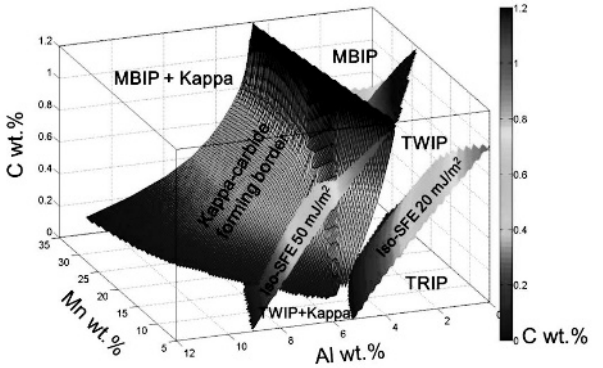

Figure 2. 3D composition-dependent SFE map of Fe-Mn-Al-C steel at 300 K [7].

TRIP/TWIP Effect in Fe-Mn-Al-C Alloys

The flow behavior of high manganese Fe-Mn-Al-C alloys designed by means of the mechanism maps is shown in Figure 3 and Figure 4. *In situ* high energy (60 keV) synchrotron X-ray with high brilliance, small beam size and high penetration depth were applied to study the dynamics of dislocation, stacking fault and twinning during *in situ* tensile test. Furthermore, the results indicate the change of microstructure and accordingly the deformation mechanisms with different the carbon content in the Fe-17Mn-1.5Al-xC alloys. With a change of carbon content from 0.3 wt.% to 0.6 wt.% in the Fe-17Mn-1.5Al-xC alloys, the predicted SFE by thermodynamic calculations changes from 18.9 mJ/m^2 to 27.5 mJ/m^2, which consequently leads to a change of predicted deformation mechanism from TRIP/TWIP to TWIP [7].

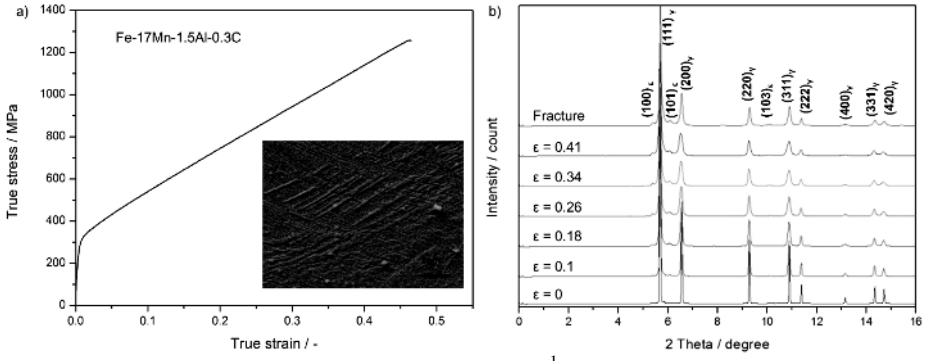

Figure 3. (a) True strain-stress curve, strain rate 0.001 s^{-1}; SEM of fractured sample after tensile test; (b) *In situ* synchrotron X-ray diffraction patterns during tensile test at room temperature.

During deformation, the occurrence of both the strain induced transformation of austenite to ε martensite and mechanical twinning is shown in the Fe-17Mn-1.5Al-0.3C steel, while only mechanical twinning is indicated in the Fe-17Mn-1.5Al-0.6C alloy [7]. The austenite Bragg peak broadening is further indicated in Figure 3b and Figure 4b. Due to the deformation twin formation, the microstructure in the steels is largely refined. The stacking fault probability and the twinning evolution show an anisotropic feature at different planes.

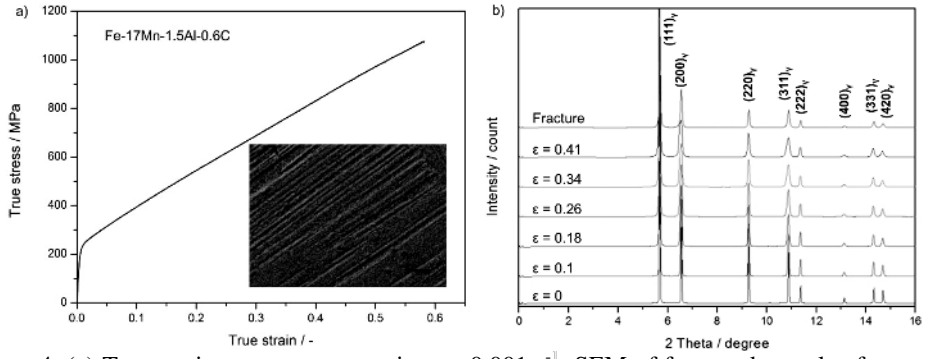

Figure 4. (a) True strain-stress curve, strain rate 0.001 s^{-1}; SEM of fractured sample after tensile test; (b) *In situ* synchrotron X-ray diffraction patterns during tensile test at room temperature.

Kappa Phase Formation in Fe-Mn-Al-C Alloys

The *in situ* SYXRD diffraction pattern in Figure 5a shows the kappa phase precipitation from austenitic matrix in Fe-30Mn-8Al-1.2C alloy during aging at 600 °C for different times [17]. With the increase of the aging time, the intensity of the γ (200) peak clearly decreases as shown in Figure 5a. As is indicated in Figure 5b, the lattice misfit between the kappa phase and the austenite matrix is very small. It shows that the lattice misfit value increases with the increase of aging time [17]. The lattice misfit value falls in the range of 1.6% - 1.8%. Up to 9 hours aging, the lattice misfit still maintains being very small (less than 2%). This indicates the high coherency of the kappa phase precipitation from the austenitic matrix, which largely contributes to the increase of the strength of the materials [17].

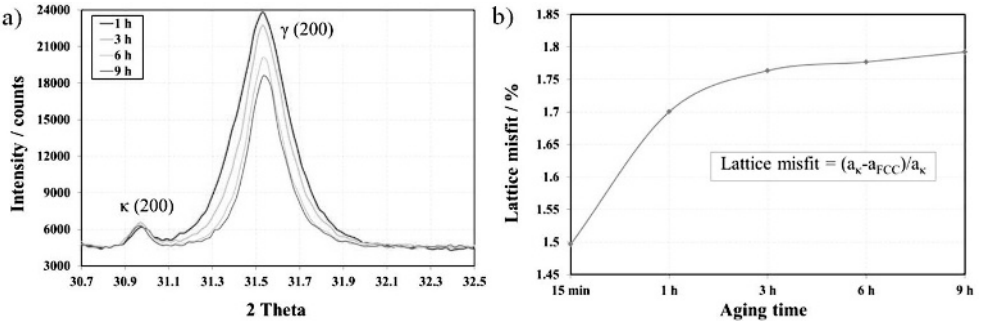

Figure 5. (a) *In situ* synchrotron diffraction peaks of κ (200) and γ (200) of Fe-30Mn-8Al-1.2C alloy annealed at 600 °C for different times. (b) The lattice misfit between the kappa phase and the austenite matrix in Fe-30Mn-8Al-1.2C alloy [17].

The kappa phase formation and the associated short- and long-range ordering features in Fe-Mn-Al-C austenitic steels were studied by means of *ab initio* theoretical calculations in combination with *in situ* synchrotron X-ray diffraction method in order to understand the driving forces for short- and long-range ordering in the steels. The results are published elsewhere [17]. Figure 6 shows the strength and ductility change with the increase of aging time during kappa phase formation at 600 °C in Fe-30Mn-8Al-1.2C alloy [17]. With the aging time up to 15 hours, the yield strength and ultimate tensile strength of the Fe-30Mn-8Al-1.2C alloy increases with the aging time [17]. With the aging time of 15 hours, the alloy possesses the strength maximum, UTS = 970 MPa and Y.S. = 789 MPa [17]. The coherent nano-sized kappa phase precipitated from the austenite matrix plays an important role in determining the mechanical properties of the Fe-Mn-Al-C austenitic steels. The nanoscale kappa phase and dislocation interaction is mainly responsible for the outstanding mechanical properties [18].

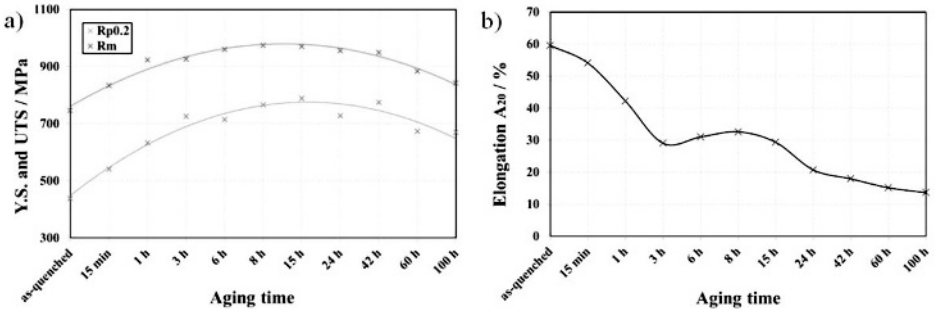

Figure 6. The ultimate tensile strength (UTS) and the yield strength (Y.S.) (a) and the ductility (b) change with the increase of aging time during kappa phase formation at 600 °C in Fe-30Mn-8Al-1.2C alloy [17].

In Figure 7, the general candidates (micro-alloyed phases NbC, VC, TiC) which is widely used for precipitation hardening is compared with the kappa phase coherent precipitation hardening [17]. It is indicated that with the proper microstructure control, the kappa phase precipitation strengthening is as effective as the micro-alloyed carbides, i.e. NbC, VC and TiC. The strengthening potential of kappa phase is between 100 - 350 MPa for a volume fraction of approximately 0.05 - 0.35 [17]. It reveals that kappa phase can be a promising candidate for precipitation hardening of the steels, and at the same time provides a great potential of strain hardening [17].

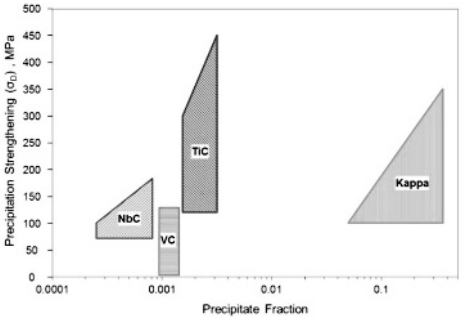

Figure 7. Comparison of strengthening by carbides in micro-alloyed steels [19] and kappa strengthening in high manganese steels [17].

Table 1 shows a comparison of the mechanical property of the investigated alloy under different aging states against the reference steel grades [17]. Comparing against the CP, DP and TRIP steels, the Fe-30Mn-8Al-1.2C alloy at the same or higher strength level can achieve much better ductility. All in all, the Fe-30Mn-8Al-1.2C alloy exhibits an improved combination of strength and ductility, with respect to the conventional HSLA, DP and TRIP steels [17].

Table 1. Comparison of the mechanical property of the investigated alloy under different aging states against the reference steel grades [17]

Steels	Y.S. $R_{p0.2}$ MPa	UTS R_m MPa	Elongation A %
Reference steel_DP HCT780	450-560	≥ 780	≥ 14
Reference steel_CP HCT780	500-700	≥ 780	≥ 10
Reference steel_TRIP HCT780	470-600	≥ 780	≥ 21
Fe-30Mn-8Al-1.2C_as-quenched	438	746	60
Fe-30Mn-8Al-1.2C_15 min aged	542	833	54
Fe-30Mn-8Al-1.2C_3 h aged	726	926	29

Conclusions

The composition-dependent SFE maps calculated via the subregular thermodynamic model can facilitate to predict the deformation mechanisms and new alloy design in high manganese Fe-Mn-Al-C alloys. The chemical content, i.e. C, Mn and Al, strongly influences the SFE and thus the deformation modes. With an increase of carbon content from 0.3 wt.% to 0.6 wt.% in the Fe-17Mn-1.5Al-xC alloys, the predicted SFE increases from 18.9 mJ/m^2 to 27.5 mJ/m^2 and the deformation mechanism shifts from TRIP/TWIP to TWIP. The Fe-30Mn-8Al-1.2C exhibits an improved combination of strength and ductility, with respect to conventional HSLA, DP and TRIP steels. The strengthening potential of kappa phase is between 100-350 MPa for a volume fraction of approximately 0.05-0.35.

Acknowledgement

The authors acknowledge the financial support from Deutsche Forschungs-gemeinschaft within the Collaborative Research Center SFB 761 “Steel *ab initio*”.

References

[1] H. Kim, D.-W. Suh, and N. J. Kim, “Fe–Al–Mn–C lightweight structural alloys: a review on the microstructures and mechanical properties,” *Science and Technology of Advanced Materials*, 14 (1) (2013), 014205.

[2] O. Bouaziz, S. Allain, C. Scott, P. Cugy, and D. Barbier, “High manganese austenitic twinning induced plasticity steels: A review of the microstructure properties,” *Current opinion in solid state and materials science,* 15 (4) (2011), 141-168.

[3] T. S. Byun, "On the stress dependence of partial dislocation separation and deformation microstructure in austenitic stainless steels," *Acta Materialia*, 51 (11) (2003), 3063-3071.

[4] G. Frommeyer, U. Brüx, and P. Neumann, "Supra-ductile and high-strength manganese-TRIP/TWIP steels for high energy absorption purposes," *ISIJ International*, 43 (3) (2003), 438-446.

[5] D. Barbier, N. Gey, S. Allain, N. Bozzolo, and M. Humbert, "Analysis of the tensile behavior of a TWIP steel based on the texture and microstructure evolutions," *Materials Science and Engineering: A*, 500 (1) (2009), 196-206.

[6] J. Yoo, and K.-T. Park, "Microband-induced plasticity in a high Mn–Al–C light steel," *Materials Science and Engineering: A*, 496 (1) (2008), 417-424.

[7] W. Song, T. Ingendahl, and W. Bleck, "Control of Strain Hardening Behavior in High-Mn Austenitic Steels," *Acta Metallurgica Sinica (English Letters)*, 27 (3) (2014), 546-556.

[8] I. Gutierrez-Urrutia, and D. Raabe, "Influence of Al content and precipitation state on the mechanical behavior of austenitic high-Mn low-density steels," *Scripta Materialia*, 68 (6) (2013), 343-347.

[9] C.N. Hwang, C.Y. Chao, and T.F. Liu, "Grain boundary precipitation in an Fe-8.0 Al-31.5 Mn-1.05 C alloy," *Scripta Metallurgica et Materialia*, 28 (2) (1993), 263-268.

[10] G.E. Hale, and A.J. Baker, Conf. on Alt. Alloying for Env. Res. New Orleans, LA., 1986

[11] H. Springer, and D. Raabe, "Rapid alloy prototyping: Compositional and thermo-mechanical high throughput bulk combinatorial design of structural materials based on the example of 30Mn–1.2 C–xAl triplex steels," *Acta Materialia*, 60 (12) (2012), 4950-4959.

[12] A.T. Dinsdale, "SGTE data for pure elements," *Calphad*, 15 (4) (1991), 317-425.

[13] A. Saeed-Akbari, L. Mosecker, A. Schwedt, and W. Bleck, "Characterization and prediction of flow behavior in high-manganese twinning induced plasticity steels: Part I. Mechanism maps and work-hardening behavior," *Metallurgical and Materials Transactions A*, 43 (5) (2012), 1688-1704.

[14] S. Allain, J.P., Chateau, and O. Bouaziz, "A physical model of the twinning-induced plasticity effect in a high manganese austenitic steel," *Materials Science and Engineering: A*, 387 (2004), 143-147.

[15] P.H. Adler, G.B. Olson, and W.S. Owen, "Strain hardening of Hadfield manganese steel," *Metallurgical and Materials Transactions A*, 17 (10) (1986), 1725-1737.

[16] A. Saeed-Akbari, J. Imlau, U. Prahl and W. Bleck, "Derivation and variation in composition-dependent stacking fault energy maps based on subregular solution model in high-manganese steels," *Metallurgical and Materials Transactions A*, 40 (13) (2009), 3076-3090.

[17] W. Song, W. Zhang, J. von Appen, R. Dronskowski, W. Bleck, "Kappa phase formation in Fe-Mn-Al-C austenitic steels," *Steel Research International*, accepted.

[18] I. Gutierrez-Urrutia, and D. Raabe, "Multistage strain hardening through dislocation substructure and twinning in a high strength and ductile weight-reduced Fe–Mn–Al–C steel," *Acta Materialia*, 60 (16) (2012), 5791-5802.

[19] H. Stuart (Ed.), *Proceedings of the International Symposium, Niobium &1*San Francisco, USA 1981

3rd World Congress on Integrated Computational Materials Engineering (ICME 2015)
Edited by: Warren Poole, Steve Christensen, Surya R. Kalidindi, Alan Luo, Jonathan D. Madison, Dierk Raabe, and Xin Sun
TMS (The Minerals, Metals & Materials Society), 2015

EXPERIMENTS AND MODELING OF THREE-DIMENSIONAL DENDRITIC MORPHOLOGY OF MAGNESIUM ALLOY

Manhong Yang[1], Zhipeng Guo[1], Shoumei Xiong[1,2]

[1]School of Materials Science and Engineering, Tsinghua University; Beijing, 100084, China
[2]State Key Laboratory of Automobile Safety and Energy, Tsinghua University

Keywords: Magnesium Alloys, Synchrotron X-ray Tomography, Dendritic Growth, Three-dimensional

Abstract

Magnesium alloys are one of the lightest structural materials. The mechanical properties of magnesium alloys are often affected by the dendritic microstructures. With hexagonal close-packed structure, the preferred growth direction of α-Mg dendrite was believed to be $\langle 11\bar{2}0 \rangle$, and different 3-D growth models were proposed. However, these growth models for α-Mg dendrites were divergent and not yet generally accepted. Recently, Mg–20 wt.% Y alloy was studied by synchrotron X-ray tomography to establish the three-dimensional dendritic morphology of magnesium alloy. According to the reconstructed results, the α-Mg dendrites grew along eighteen branches with six branches along $\langle 11\bar{2}0 \rangle$ in the {0001} basal plane, and twelve along $\langle 11\bar{2}3 \rangle$ in the non-basal plane. Based on the three-dimensional morphology of α-Mg (Y) dendrite, a cellular automaton model was developed to simulate the dendritic growth of magnesium alloy. Both the experimental and simulation results offer a deep insight in understanding the dendritic growth evolution of magnesium alloys during solidification.

Introduction

Magnesium alloys are widely used as casting alloys due to their excellent properties, such as high specific strength and low density [1]. The mechanical properties of magnesium alloys are greatly dependent on their as-cast microstructure, of which the so-called dendritic structure is important[2].

It is widely accepted that the preferred growth orientation is typically along $\langle 100 \rangle$ in face-centred cubic (FCC) and body-centred cubic (BCC) alloy systems [2,3]. However, for the hexagonal close-packed (HCP) alloy system, different growth orientations have been reported in references [4, 5]. Pettersen *et al.* [5] found that the dendrites in AZ91 magnesium under directional solidification had two different stem directions including $\langle 11\bar{2}0 \rangle$ and $\langle 22\bar{4}5 \rangle$. They also found the $\langle 11\bar{2}0 \rangle$ stems had secondary arms in six directions, while the $\langle 22\bar{4}5 \rangle$ stems had only three. Wang *et al.* [6] studied the 3-D morphology of α-Mg dendrites in directionally solidified Mg-9wt.%Al alloy by synchrotron X-ray tomography, and suggested that α-Mg dendrite grew along $\langle 11\bar{2}0 \rangle$ in the {0001} basal plane with a plate-like morphology. The plate-like dendritic morphology exhibited six-fold symmetry in the {0001} basal plane and was different from that reported by Pettersen [5]. In addition to experimental methods, numerical modeling has become a powerful tool to study the microstructure evolution of magnesium alloys. Böttger *et al.* [7,8] incorporated a hexagonal anisotropy function into the phase-field (PF) model, and simulated the

growth of the α-Mg dendrite, which had six prism orientations in the {0001} basal plane and two orientation in the ⟨0001⟩ directions. Wu *et al.* [9] simulated the dendrites growth of AM50 alloy by cellular automaton (CA) model based on Böttger's model [7]. Eiken [10] investigated the growth evolution of magnesium by PF model, and found that dendrites grew faster along $\langle 11\bar{2}0 \rangle$ than ⟨0001⟩ direction. Wang *et al.* [6,11] also simulated the unidirectional solidified dendrites by PF model based on the reconstructed dendrite by synchrotron X-ray tomography. They found that the Mg-Al alloy dendrites exhibited six-fold symmetry in the {0001} basal plane.

The purpose of this paper is to investigate the 3-D morphology of the α-Mg dendrite using synchrotron X-ray tomography. It was found that, for the first time, the reconstructed α-Mg dendrite had 18 primary branches. While, the growth function for the CA model was developed and employed to simulate the dendritic microstructure.

Experimental

Mg–20 wt.% Y alloy was selected as the primary phase and eutectic phase present good absorption contrast. As-cast alloys was prepared as follows: magnesium (99.95 wt.%) and yttrium (99.99 wt.%) were first melted at 800℃ under a mixed protective gas of 99.7% N_2 and 0.3% SF_6 [12,13], and then, the melt was poured into a permanent mould (preheated to 300℃ for 30 min) and cooled in air [12]. Finally, cylindrical specimens of 10 mm in diameter and 30 mm in height were machined from the as-cast ingots and were re-solidified to obtain the quenched alloys samples. The specimen was first sealed in a quartz tube with argon as protective atmosphere, then it was remelted and quenched in water between liquidus and eutectic temperatures. Cylindrical specimens of 1 mm in diameter and 5 mm in height were machined from the quenched ingot and were used for tomography experiments.

Tomography experiments were carried out at the BL13W1 beam line of the Shanghai Synchrotron Radiation Facility (SSRF). An X-ray energy of 28 keV was used to penetrate the specimens, and 900 projections were taken between 0° and 180° using an exposure time of 5 s per projection. The distance between the specimen and the camera was 20 cm. The reconstructions resulted in volumes of 2048^3 voxel with a pixel size of 0.74 μm.

Model Description

Heat transfer equation

It is assumed that the temperature field is homogeneous and the solute diffusion in the solid phase is negligible. The governing equation for the solute redistribution in the liquid and solid can be given by

$$\frac{\partial C_S}{\partial t} = \nabla \cdot \left(D_S \nabla C_S \right) \tag{1}$$

$$\frac{\partial C_L}{\partial t} = \nabla \cdot \left(D_L \nabla C_L \right) + C_L \left(1 - k\right) \frac{\partial f_S}{\partial t} \tag{2}$$

where C_L and C_S are the solute concentrations of the liquid and solid, respectively. D_L and D_S are the liquid and solid solute diffusion coefficients, k is the partition coefficient, f_S is the solid fraction and t is the time. The last term on the right hand side of the Eq. (2) represents the solute rejection at the solid/liquid interface.

Calculation of the growth kinetics

Local equilibrium exists at the solid/liquid interface

$$C_{\mathrm{S}}^{*} = kC_{\mathrm{L}}^{*} \tag{3}$$

$$C_{\mathrm{L}}^{*} = C_0 + \frac{T^{*} - T_{\mathrm{L}}^{\mathrm{eq}}}{m_{\mathrm{L}}} + \frac{\Gamma K f\left(\theta,\varphi\right)}{m_{\mathrm{L}}} \tag{4}$$

where C_0 is the initial concentration of the alloy, T^{*} and $T_{\mathrm{L}}^{\mathrm{eq}}$ is the interface and equilibrium liquidus temperature respectively, m_{L} is the liquidus slope, Γ is the Gibbs-Thomson coefficient, K is the interface curvature and $f\left(\theta,\varphi\right)$ is the surface energy anisotropy [14]. The interface curvature was calculated by the counting method [9].

The growth velocity at the solid/liquid interface can be expressed as [15]

$$\boldsymbol{v}_{\mathrm{n}} = \frac{1}{C_{\mathrm{L}}^{*}\left(1-k\right)}\left(-D_{\mathrm{L}}\nabla C_{\mathrm{L}} + D_{\mathrm{S}}\nabla C_{\mathrm{S}}\right)\cdot\boldsymbol{n} \tag{5}$$

The solid fraction increment δf_{S} at the interface can be calculated as [9]

$$\delta f_{\mathrm{S}} = \frac{\delta t}{\Delta s}\left(V_x + V_y + V_z\right) - \frac{\delta t^2}{\Delta s^2}\left(V_x\cdot V_y + V_x\cdot V_z + V_y\cdot V_z\right) + \frac{\delta t^3}{\Delta s^3}\cdot V_x\cdot V_y\cdot V_z \tag{6}$$

where Δs is the cell size and δt is the time step. When the solid fraction f_{S} equals 1, the cell changes into solid state and captures the neighboring liquid cells.

Results and Discussion

2-D microstructure of magnesium-based alloys

Fig. 1 shows optical micrographs (OM) of the Mg–20 wt.% Y alloy. The microstructure mainly comprised of the primary phase or the α-Mg dendrite (white) and eutectic phase (black). The eutectic phase was uniformly distributed between the primary dendrites on the grain boundaries. As shown in Fig. 1, the α-Mg dendrite exhibited a typical snow-flake shape with six branches growing out symmetrically from the nuclei as designated by "D_1" and "D_2". There were also dendrites exhibiting six branches without six-fold symmetry as designated by"D_3" and"D_4". It is also noted that not all the α-Mg dendrites grew into a snow-flake shape and most dendritic morphologies were distorted like "D_5" and "D_6".

3-D microstructure of magnesium alloys

A tomography slice extracted from the samples of the Mg–20 wt.% Y is shown in Fig. 2a. Following the procedures for image processing including cropping, 3-D filtering, thresholding and segmentation [14], a sub-volume of the dendrites was reconstructed and is shown in Fig. 2b.

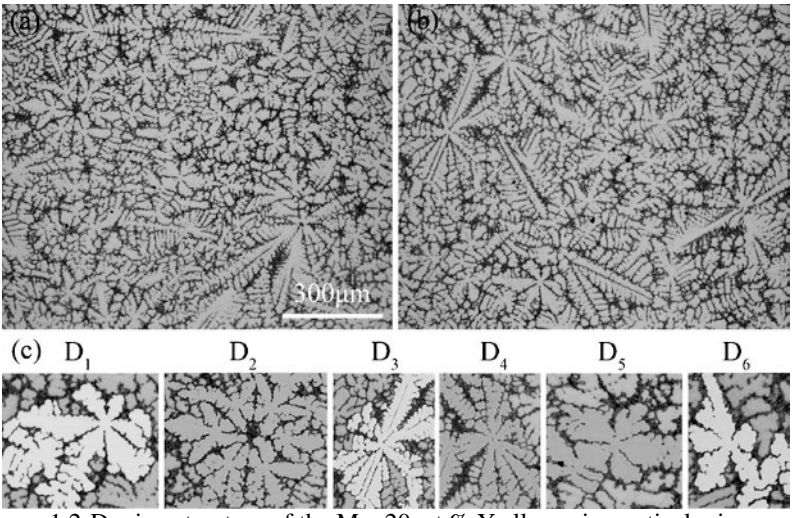

Figure 1 2-D microstructure of the Mg–20 wt.% Y alloy using optical microscope

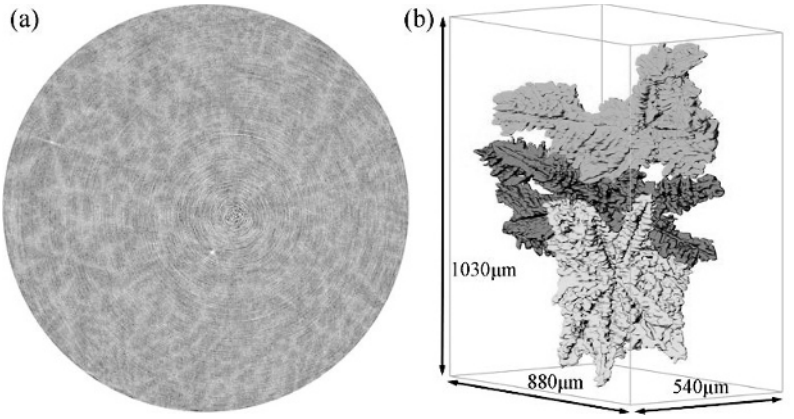

Figure 2 (a) A tomography slice of the Mg–20 wt.% Y alloy and (b) the according 3-D reconstruction of the dendrites extracted from the quenched sample.

All the reconstructed results show that the dendrites have the same 3-D microstructure and Fig. 3 shows the integrated 3-D morphology of the α-Mg dendrite from synchrotron X-ray tomography experiment. As shown in Fig. 3b, the dendrite exhibited six-fold symmetry on the basal plane, as designated by $A_1 - A_6$. As shown in Fig. 3c, the dendrite can be divided into three parts, that is, the top ($B_1 - B_3$), the middle ($A_1 - A_4$) and the bottom ($B_2 - B_4$). It is clear that the overall dendrite had eighteen branches. The dendrite exhibited intensive side branching in the top and bottom, and the dendrite branches finally fell into two categories. The first category had six-fold symmetric branches on the $\{0001\}$ basal plane, or the growth orientation on the basal plane was $\langle 11\bar{2}0 \rangle$, as reported in [4]. The second category has twelve branches above and below the basal plane. Further investigation revealed that the angle between A_4 and B_1 (or B_2) is smaller than 60°, indicating that the dendritic morphology was not six-fold symmetric on the $\{10\bar{1}0\}$ crystal plane. Based on measurements, the angle between A_4 and B_1 (or B_2) is determined to be 52°±3°.

By crystallographic calculation, the growth orientation along B_1 is $\langle 11\bar{2}3 \rangle$, which is close to $\langle 22\bar{4}5 \rangle$ as reported in literature [5].

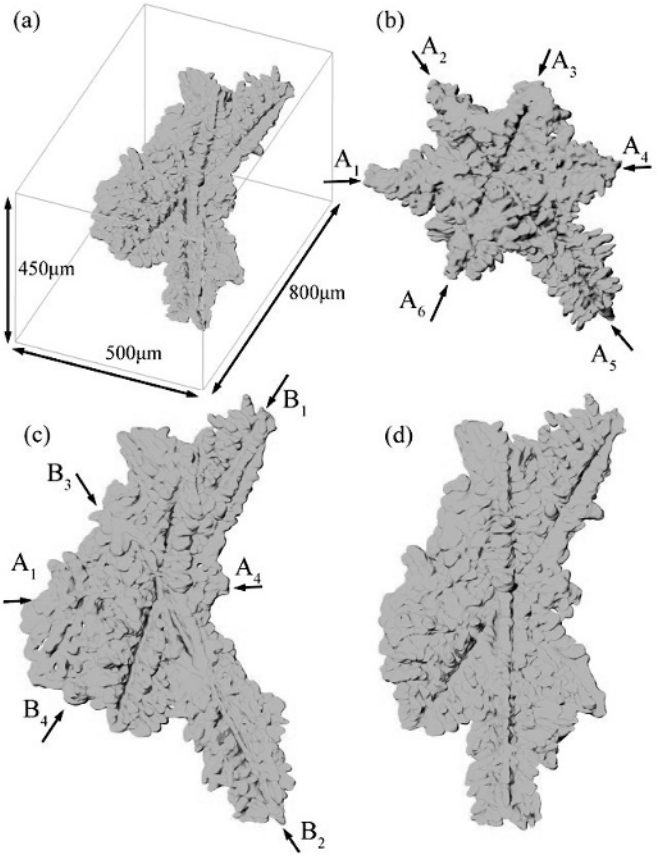

Figure 3 (a) The 3-D reconstructed dendrites extracted from the Mg–20 wt.% Y alloy. Dendrite morphologies with respect to three different view directions including $\{0001\}$, $\{10\bar{1}0\}$ and $\{11\bar{2}0\}$ were shown in (b) – (d) respectively.

The CA simulation

Based on the reconstructed 3-D dendrite morphology of the α-Mg dendrite, a growth model describing the eighteen-branch morphology was developed, and the corresponding neighborhood configuration was defined [9]. The dendritic growth of the Mg–20 wt.% Y alloy was simulated to verify the 3-D CA model. A single nucleus was set at the centre of the calculation domain with 200 × 200 × 200 cubic cells and the spatial step was set to be 1 μm. The temperature field was uniform and the cooling rate was 80 K/s. The Neumann boundary condition was employed. Figs. 4a and 4b show the simulated 3-D dendritic morphology and the contour map of the solute distribution. According to Fig. 4c, the dendrite grew into six-fold symmetry on the *xy*-plane. On the *xz*-plane, the dendrite grew with six arms of which two lay in the *xy*-plane and four lay at

upper and lower sides, as indicated in Fig. 4d. The simulated dendrite also exhibited eighteen branches, which agreed with that obtained by the experiment.

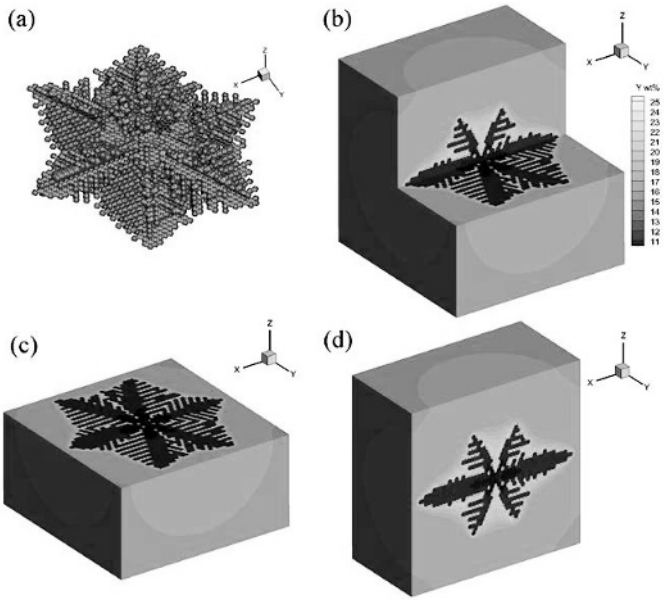

Figure 4 Simulated dendritic morphology of the α-Mg dendrite: (a) simulated equiaxed dendritic morphology; (b) 3-D solute distribution map with a cooling rate of 80K/s; (c) – (d) the dendritic morphology on the *xy*- and *xz*- plane, respectively.

Conclusions

The 2-D and 3-D dendritic morphologies of magnesium alloy were studied using the optical microscope and synchrotron X-ray tomography technique. It was found that the dendrite grew along eighteen branches with six in $\langle 11\bar{2}0 \rangle$ and twelve in $\langle 11\bar{2}3 \rangle$ directions. Based on the reconstructed dendritic morphology, a 3-D CA model was developed to simulate the dendritic growth of the magnesium alloy.

Acknowledgments

This research is funded by The National Natural Science Foundation of China (51205229 and 51275269), and the Tsinghua University Initiative Scientific Research Program (20121087918). The authors would also like to thank the Shanghai Synchrotron Radiation Facility for the provision of beam time.

References

[1] M K Kulekci. Magnesium and its alloys applications in automotive industry[J]. The International Journal of Advanced Manufacturing Technology, 2008,39(9-10):851-865.
[2] J A Dantzig, M Rappaz. Solidification[M]. EPFL press, 2009.
[3] M Asta, C Beckermann, A Karma, et al. Solidification microstructures and solid-state parallels: Recent developments, future directions[J]. Acta Materialia, 2009,57(4):941-971.

[4] K Pettersen, N Ryum. Crystallography of directionally solidified magnesium alloy AZ91[J]. Metallurgical Transactions A, 1989,20(5):847-852.
[5] K Pettersen, O Lohne, N Ryum. Dendritic solidification of magnesium alloy AZ91[J]. Metallurgical Transactions A, 1990,21(1):221-230.
[6] M Y Wang, J J Williams, L Jiang, et al. Dendritic morphology of α-Mg during the solidification of Mg-based alloys: 3D experimental characterization by X-ray synchrotron tomography and phase-field simulations[J]. Scripta Materialia, 2011,65(10):855-858.
[7] B Böttger, J Eiken, M Ohno, et al. Controlling microstructure in magnesium alloys: a combined thermodynamic, experimental and simulation approach[J]. Advanced Engineering Materials, 2006,8(4):241-247.
[8] B Böttger, J Eiken, I Steinbach. Phase field simulation of equiaxed solidification in technical alloys[J]. Acta materialia, 2006,54(10):2697-2704.
[9] M Wu, S Xiong. A three-dimensional cellular automaton model for simulation of dendritic growth of magnesium alloy[J]. Acta Metallurgica Sinica(English Letters), 2012(03):169-178.
[10] J Eiken. Dendritic growth texture evolution in Mg-based alloys investigated by phase-field simulation[J]. International Journal of Cast Metals Research, 22, 2009,1(4):86-89.
[11] M Wang, T Jing, B Liu. Phase-field simulations of dendrite morphologies and selected evolution of primary α-Mg phases during the solidification of Mg-rich Mg–Al-based alloys[J]. Scripta Materialia, 2009,61(8):777-780.
[12] Z W Zou, S M Xiong. Effect of Sr and Nd on Microstructure and Mechanical Properties of AZ91-1Si Alloy, Materials Science Forum. 2009, 610-613: 765-770.
[13] X Wang, S Xiong. Oxidation behavior of molten magnesium in atmospheres containing SO_2[J]. Corrosion Science, 2011,53(12):4050-4057.
[14] M Yang, Z Guo, S Xiong. Characterization of the 3-D dendrite morphology of magnesium alloys using synchrotron X-ray tomography and 3-D phase-field modelling. Under review.
[15] L Nastac. Numerical modeling of solidification morphologies and segregation patterns in cast dendritic alloys[J]. Acta Materialia, 1999,47(17):4253-4262.

3rd World Congress on Integrated Computational Materials Engineering (ICME 2015)
Edited by: Warren Poole, Steve Christensen, Surya R. Kalidindi, Alan Luo, Jonathan D. Madison, Dierk Raabe, and Xin Sun
TMS (The Minerals, Metals & Materials Society), 2015

PHASE FIELD SIMULATION OF OROWAN STRENGTHENING BY COHERENT PRECIPITATE PLATES IN A Mg-Nd ALLOY

Hong Liu[1], Yunzhi Wang[2], Jian-Feng Nie[1]

[1]Department of Materials Engineering, Monash University, Clayton, VIC 3800, Australia
[2]Department of Materials Science and Engineering, The Ohio State University, 2041, College Road, Columbus, OH 43210, USA

Keywords: Magnesium alloys; Precipitate-dislocation interaction; CRSS; Phase field method

Abstract

The phase field dislocation model has been used to compute and simulate interactions between basal *a*-type dislocations and coherent β_1 precipitate plates in a Mg-3wt.%Nd alloy that is strengthened exclusively by the β_1 plates. The computed increments of the critical resolved shear stress (ΔCRSS) for samples aged for 10 hours at 523 K agree well with those calculated from the existing strengthening equation for plate-shaped particles. The phase field simulations further indicate that the ΔCRSS value increases with an increase in plate aspect ratio and number density, and that the change of ΔCRSS is not sensitive to the variation of β_1 plate diameter distribution when the average diameter of β_1 plates is fixed. When the volume fraction of β_1 plates is constant, the ΔCRSS value for a random spatial distribution of the β_1 plates is approximately 0.78 times of that for a regular spatial distribution.

Introduction

Plate-shaped precipitates are often the key strengthening constituents in age hardenable magnesium alloys [1-2], such as $\{1\bar{1}00\}_\alpha$ plates of β_1 phase in Mg-Nd alloys [1-2]. However, there is currently little detailed quantitative understanding of the interactions between these precipitate plates and gliding dislocations and the strengthening effects produced by such precipitate plates. There has been a lack of information on the quantitative relationship between the spatial distribution and size distribution of precipitate plates and alloy yield strength. The current versions of the Orowan equation that are used to predict the critical resolved shear stress increment (ΔCRSS) of these alloys are modified from the equations for spherical particles, and the validity of these modifications has not been thoroughly examined by experiments or simulations [3-5].

Therefore, the main objective of this study is to provide detailed and accurate information on dislocation-precipitate interactions in one of these alloys. The *a*-type dislocations with a $1/3\langle 11\bar{2}0\rangle_\alpha$ Burgers vector are the most commonly observed in HCP structures [6]. This type of dislocations is usually classified into three categories according to their slip planes, i.e., basal *a*-type, prismatic *a*-type and pyramidal *a*-type [6]. Among these three categories, the basal *a*-type dislocation is the most frequently observed one. Therefore, the slip system selected in this paper is $1/3\langle 11\bar{2}0\rangle_\alpha\ (0001)_\alpha$. To avoid the need to track the exact position of the gliding dislocation at every time step, the phase field dislocation approach [7] is used to systematically and quantitatively evaluate the effect of the number density, size, planar diameter distribution, and

spatial distributions on ΔCRSS. A Mg-3Nd (wt.%) alloy is selected as a model system. The precipitates in aged samples of the Mg-3Nd (wt.%) alloy are predominantly $\{1\bar{1}00\}_\alpha$ plates of a single precipitate phase, β_1, which significantly simplifies the microstructure construction process [2]. The β_1 phase has a cubic structure (a = 0.74 nm). The orientation relationship between β_1 and α-Mg phases is such that $(\bar{1}12)_{\beta_1}//(1\bar{1}00)_\alpha$ and $[110]_{\beta_1}//[0001]_\alpha$. According to TEM images, it is rare to observe that β_1 particles are sheared by dislocations, thus all precipitates are assumed to be non-shearable. Note that the deformation mode is assumed to be basal slip.

Methodologies

Crystalline and Elastic Strain Energies of Dislocations

To determine the energy barrier of dislocation gliding inside the Mg matrix, the generalized stacking fault (GSF) energy contour for Mg matrix phase is calculated by the *ab-initio* approach [8]. Since only the $\langle 11\bar{2}0\rangle_\alpha(0001)_\alpha$ slip system is considered in the present study, and all dislocations are assumed as perfect, the function of the crystalline energy is obtained by fitting the GSF landscape of Mg matrix phase along $\langle 11\bar{2}0\rangle_\alpha$ through a forth order poly-nominal equation:

$$\Gamma_\alpha(\eta) = 5.032 \times 10^3(\eta^4 - 2\eta^3 + \eta^2). \quad (1)$$

The elastic strain energy of dislocation is formulated by using the Khachaturyan and Shatalov's microelasticity theory [9], and the homogeneous elastic constant approximation is used. In the calculation, the coordinate system is $x_0 = [1\bar{1}00]_\alpha$, $y_0 = [11\bar{2}0]_\alpha$ and $z_0 = [0001]_\alpha$. It is assumed that all forces on the surface are zero, i.e., a stress-free boundary condition is assumed in the calculation [9]. The elastic strain energy of dislocations is given by:

$$E^{elas}(\theta,\eta) = \frac{1}{2} \int \frac{d\mathbf{g}}{(2\pi)^3} \left[B_{pq}\left(\frac{\mathbf{g}}{|\mathbf{g}|}\right) \{\tilde{\eta}_p\}_\mathbf{g} \{\tilde{\eta}_p\}^*_\mathbf{g} \right] - \int d\mathbf{r} \left[\sigma_{ij}^{app} \varepsilon_{ij}(\mathbf{r})\right], \quad (2)$$

where the integral is taken in reciprocal space, g is a vector in reciprocal space, $\{\tilde{\eta}_p\}_\mathbf{g}$ is the Fourier transform of η(r), r is a vector in real space, the σ_{ij}^{app} is applied stress and $\varepsilon_{ij}(\mathbf{r})$ is the SFTS field of an arbitrary microstructure consisting of precipitates and dislocations. Note that g = 0 is excluded from the integration, which defines the principal value. The asterisk indicates the complex conjugate. $B_{pq}(\mathbf{g}/|\mathbf{g}|)$ can be expressed as [9]:

$$B_{pq}(\mathbf{g}/|\mathbf{g}|) = B_{pq}(\mathbf{n}) = C_{ijkl}\varepsilon_{ij}(p)\varepsilon_{kl}(q) - n_i\sigma_{ij}(p)\Omega_{jk}\sigma_{kl}(q)n_l \quad \mathbf{g} \neq 0$$

where n = **g**/|**g**| is a unit vector in the reciprocal space and is defined only when **g** ≠ 0, $\Omega_{ij}^{-1} = n_k n_l$, and $\sigma_{ij}(p) = C_{ijkl}\varepsilon_{kl}(p)$. The SFTS field in an arbitrary microstructure consisting of precipitates and dislocations can be formulated as [10-11]:

$$\varepsilon_{ij}(\mathbf{r}) = \varepsilon_{ij}^0 \theta(\mathbf{r}) + \frac{\boldsymbol{b} \otimes \boldsymbol{m}}{2d_{(0001)}} \eta(\mathbf{r}), \quad (3)$$

where ***m*** is the slip plane normal and ***b*** denotes the Burgers vector, d is the inter-planar spacing of the slip plane, and θ(r) is a shape function: θ(r) = 1 when r is located in the β_1 phase while θ(r) = 0 when r is in the α-Mg matrix. The first term of this SFTS formula describes the lattice

mismatch between α-Mg and β_1 phases. In the present study, only the second term, i.e., the eigenstrain of dislocations, is considered.

Total Energy and Kinetics of Dislocations

The total energy E of the dislocation is a sum of the crystalline energy, elastic strain energy and gradient energy:

$$E = \int \mathrm{d}^3 r \left[{E^{crystal}}/{d_{(0001)}} + \frac{\kappa_\eta}{2}(\nabla\eta)^2 \right] + E^{elas}, \quad (4)$$

where the term $\frac{\kappa_\eta}{2}(\nabla\eta)^2$ is the gradient energy, which is related to the dislocation core energy [9-11], and κ_η is the gradient energy coefficient. The minimization of the total energy E is carried out numerically by solving the time-dependent Ginzburg-Landau equation [12].

Microstructure Construction and Initial Conditions

A HADDF-STEM image showing the distribution of β_1 particles with 1 μm × 1 μm size is shown in Fig. 1a. The horizontal and vertical directions, i.e., x and y directions are $[1\bar{1}00]_\alpha$ and $[11\bar{2}0]_\alpha$, respectively, and the viewing direction is parallel to $[0001]_\alpha$. In this STEM image, the β_1 particles appear bright because Nd has a relatively high atomic number. This STEM image is digitized and used directly as an input-parameter in phase field simulations (Fig. 1b). In Fig. 1b, the morphology of β_1 particles is simplified to be rectangular.

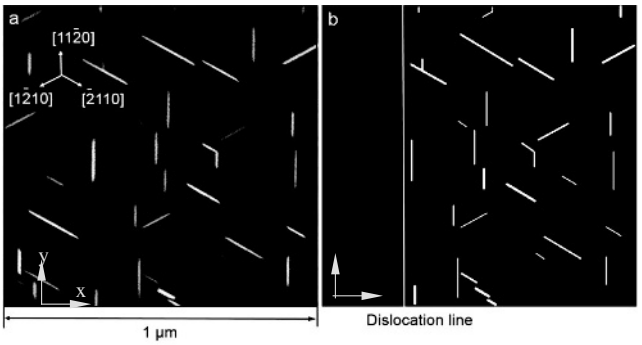

Fig. 1 (a) HAADF-STEM image of β_1 precipitates in a Mg-3wt.%Nd alloy aged for 3 hours and 200 °C and (b) digitized image with initial position of the dislocation.

A 512 × 512 system is used to simulate the distribution of precipitates in the $(0001)_\alpha$ slip plane. The length of each grid is 1.95 nm. To avoid the influence of elastic interactions between two neighbouring dislocations on ΔCRSS calculation, the inserted dislocation cannot be placed too close to the system boundary. In addition, to ensure the accuracy of the ΔCRSS calculation, i.e., to ensure the amount of precipitates in the system is high enough, the dislocation has to be placed close to the left side of the system. Therefore, a compromise is made on the position of the inserted dislocation and, in this case, the position of the dislocation is selected as $x = 128$ grid (Fig.1b). The β_1 particles in the region with $x < 128$ grid are removed in order to have a straight dislocation in the simulation. The insert dislocation is a screw type with $\boldsymbol{b} = a/3\langle 11\bar{2}0\rangle_\alpha$.

Curvature Correction of Dislocation Line Tension

A dislocation line is considered as the boundary between the slipped and unslipped regions. Because of the diffuse-interface nature of the phase field model, the value of the dislocation core

energy, which corresponds to the boundary energy, is often over-estimated and has to be corrected. A method commonly used is to obtain the correction coefficient [11], which is the ratio between the critical stress needed to stabilize a dislocation loop in the simulation and the stress obtained from the equation $\tau = Gb/2r$, where G is the shear modulus of the matrix and r is the radius of the dislocation loop. In this study, before the correction, the critical stress is much higher and equals to $\tau = 1.7Gb/2r$. However, after the curvature correction, the critical stress is restored to match the value obtained from the equation $\tau = Gb/2r$.

Results and Discussion

ΔCRSS of Aged Mg-3wt.%Nd Alloy

Fig. 2 (a) and (b) shows the gliding process of a screw dislocation ($\boldsymbol{b} = a/3[11\bar{2}0]_\alpha$) under an applied external stress, 55 MPa, at different time steps. The dislocation starts to glide when a shear stress is applied. The dislocation bows when it approaches the β_1 plates, and will glide through the gap of β_1 particles if the applied shear stress is larger than Gb/λ, where λ is the inter-particle spacing. Otherwise, it will be pinned and cannot glide further. The dislocation front is indicated by letter *A* in Fig. 2b. After the dislocation has bypassed the precipitates, dislocation loops are left around individual particles (marked by letter *B*) or clusters of *C*). For the 55 MPa applied external stress, the dislocation is pinned. When the stress is increased to 65 MPa (Fig. 2c), the dislocation is able to glide through the entire microstructure.

The smallest applied stress for a dislocation to percolate completely through the precipitate forest is defined as ΔCRSS. In the present study, to ensure the accuracy of the calculation, 10 groups of randomly distributed precipitates are constructed for each aging time by using 10 different sets of random seeds. For each group of precipitates, the smallest stress necessary for a screw ($\Delta\tau_s$) or an edge ($\Delta\tau_e$) dislocation to completely percolate through the precipitate forest is computed and the averaged value of $\Delta\tau_s$ and $\Delta\tau_e$ is used to represent the ΔCRSS ($\Delta\tau$) of the group. This method is repeated for each of the ten groups. Then, the values of ΔCRSSs of the ten groups are averaged and used as the ΔCRSS ($\overline{\Delta\tau}$) of the selected aging condition. The average value of these ten groups are 62.45 MPa. The difference between this value and ΔCRSS value predicted by Equations proposed by Zhu *et al.* [13], which is 63.43 MPa, is acceptable. The standard deviation of $\overline{\Delta\tau}$ is approximately 6 MPa.

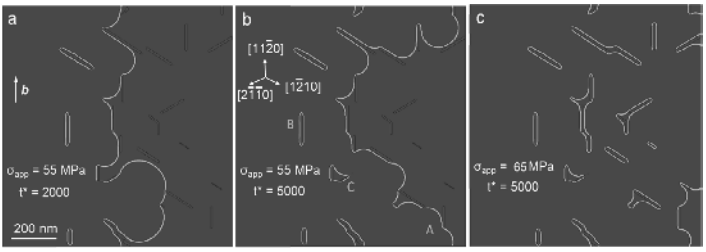

Fig. 2 (a) and (b) Gliding process of a screw dislocation ($\boldsymbol{b} = a/3[11\bar{2}0]_\alpha$) under an applied shear stress of 55 MPa at different time steps. The dislocation front is indicated by letter A in (b). After the dislocation bypasses the precipitates, some dislocation loops are left surrounding individual precipitates or clusters of precipitates, which are marked by letters B and C respectively in (b). (c) The dislocation has passed the entire microstructure when applied stress is increased to 65 MPa. Viewing direction is parallel to $[0001]_\alpha$.

Effect of Precipitate Planar Diameter Distribution on ΔCRSS

There are no explicit forms of the size distribution of planar diameters, $f(d_p)$, to describe the diameter distribution for plate-shaped precipitates. One approach is to measure d_p of each β_1 plate from TEM images. In the present study, a total of 383 precipitate plates was measured for samples aged for 3 hours. The histogram, (Fig. 3), shows the obtained d_p distribution. Four different types of distribution functions were tested on the d_p distribution, and it was found that the log-normal distribution gave the best fit of the d_p distribution. The log-normal distribution has the following form:

$$f(d_p) = \frac{1}{l \cdot \sigma\sqrt{2\pi}} e^{-\frac{(\ln d_p - \mu)}{2\sigma^2}}, \quad (5)$$

where the fitting parameters, μ and σ, are 4.23 and 2.1, respectively, and the fitting curve is shown in Fig. 3.

The other convenient method is to assume that all precipitates have the same diameter, d_0. Under this assumption, the form of $f(d_p)$ becomes:

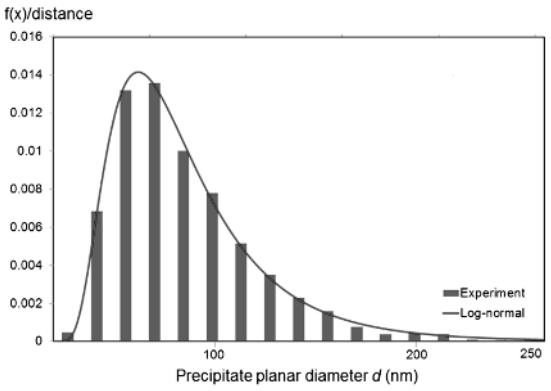

Fig. 3 Distribution of the measured planar diameter of β_1 particles $(0001)_\alpha$ intersection plane in samples aged for 3 hours at 200 °C. The curve shows the fitting by the log-normal distribution.

$$f(d_p) = \frac{d_p}{d_0\sqrt{{d_0}^2 - {d_p}^2}} \quad (0 < d_p \le d_0). \quad (6)$$

This $f(d_p)$ is used in the construction of the distribution of precipitates that have the same diameters. The other input parameters, which include $\bar{t}_p$ and N_v of β_1 precipitates, remain the same in the simulations. The simulations are based on the distribution of precipitates in samples aged for 3 hours at 200 °C. The other input parameters, the number density N_v and the average planar thickness $\bar{t}_p$, as measured from TEM images, are 2126 μm^{-3} and 5.2 nm respectively. The distribution of precipitates is assumed to be regular or random. The $\overline{\Delta\tau}$ values corresponding to the regular and random distributions are 83.3 ± 5.20 and 62.45 ± 5.85 MPa, respectively. For each of the two types of distributions, the $\overline{\Delta\tau}$ value is obtained from ten groups of planar diameters of precipitates. These $\overline{\Delta\tau}$ values are not significantly different from the $\overline{\Delta\tau}$ values obtained from a log-normal type d_p distribution.

To examine whether the value of ΔCRSS is sensitive to the change of $f(d_p)$ when the average planar diameter $\bar{d}_p$ is fixed, the $\overline{\Delta\tau}$ values are computed for the following three types of $f(d_p)$:

- Degenerate distribution: The planar diameters of all precipitates are the same and equal to $\bar{d}_p$, and $\bar{d}_p$ = 69.30 nm.
- Bernoulli distribution: Two arbitrary values are assumed for the planar diameters of precipitates: d_{p1} = 10.0 nm and d_{p2} = 128.6 nm. To make $\bar{d}_p$ equal to 69.30 nm, the number of

precipitates for each size is equal.

- Uniform distribution: The d_p values are uniformly distributed between 10 nm to 128.6 nm, i.e., the probability for a precipitate to have a planar diameter of any value between 10 nm to 128.6 nm is equal.

Comparison of the computed values of $\overline{\Delta\tau}$, Table I, the results indicate that their difference is less than 3 MPa when the distribution is changed from one type to the other. This implies that the ΔCRSS is not sensitive to the change of $f(d_p)$ when $\bar{d}_p$ is fixed.

Table I ΔCRSS (MPa) values for alloys containing precipitates of different $f(d_p)$

Planar Diameter Distribution $f(d_p)$	Degenerate	Bernoulli	Uniform
Random Spatial Distribution	60.45 ± 7.02	58.50 ± 6.93	63.50 ± 6.90
Regular Spatial Distribution	75.51 ± 6.37	72.50 ± 4.23	73.26 ± 5.50

Effect of Precipitate Aspect Ratio and Number Density on ΔCRSS

The variation of ΔCRSS values as a function of aspect ratio, A, and/or number density N_v of precipitate plates is computed under the assumption that all particles are randomly distributed and have the same diameter d. The plate aspect ratio varies from 1:1 to 60:1. The distributions of precipitates with different aspect ratios are shown in Figs. 4a-e. When A reaches 40:1 or 60:1, the $\overline{\Delta\tau}$ value is approximately 83.0 or 124.7 MPa, Table II. A comparison of microstructures shown in Figs. 4a-4e reveals that, when A increases, the number density per unit area N_a also increases. The increase in N_a is simply because the increase in plate aspect ratio raises the probability of intersection by the slip plane. For a given A, if N_v of precipitates increases to 4252 or 8504 μm^{-3} (Figs. 4f-4g), i.e., two or four times higher than that in the peak-aged condition, then the ΔCRSS reaches 82 or 116 MPa. These results suggest that, when A/N_v of precipitates increases, the effective inter-precipitate spacing λ decreases, and a higher applied stress is required for dislocations to glide through the precipitate forest.

Effect of Precipitate Spatial Distribution on ΔCRSS

To accurately calculate the ΔCRSS of an alloy containing a random distribution of particles, a modified versions of Orowan equation have been proposed [5-6, 13]:

$$\Delta\tau = \frac{\mu \cdot Gb}{2\pi M \cdot \lambda_r} \ln\left(\frac{R}{r_0}\right), \tag{7}$$

where G is the shear modulus of the matrix, λ_r is the spacing between particles that have a regular distribution, μ is the ratio of ΔCRSS values of the alloys containing a random distribution precipitates and a regular distribution of precipitates, M is a constant that is often expressed by the term $(1\text{-}v)^{1/2}$ where v is the Possion's ratio, and R and r_0 are the outer and inner cut-off radius of the dislocation.

Empirically, the average diameter of precipitates $\bar{d}$ and the length of the Burgers vector of the gliding dislocation b are used to represent R and r_0 respectively for alloys containing spherical precipitates [3-5, 13]. For point obstacles and spherical particles, mathematical analyses indicate that μ equals to 0.84 when the stress field of the dislocation is not considered [5]. If the stress field of dislocation is taken into account, then the form of μ becomes $(\ln D / \ln \lambda_r)^{1/2}$ or a coefficient of 0.8 [3-5, 13]. Note that the above forms of μ are valid only for spherical particles. Whether or not these forms are still valid when the particle shape changes from sphere to plate

has not been examined. For precipitate distributions in samples aged for 3 hours, the $\overline{\Delta\tau}$ values corresponding to the regular and random distributions are 83.3 ± 5.20 and 62.45 ± 5.85 MPa, respectively.

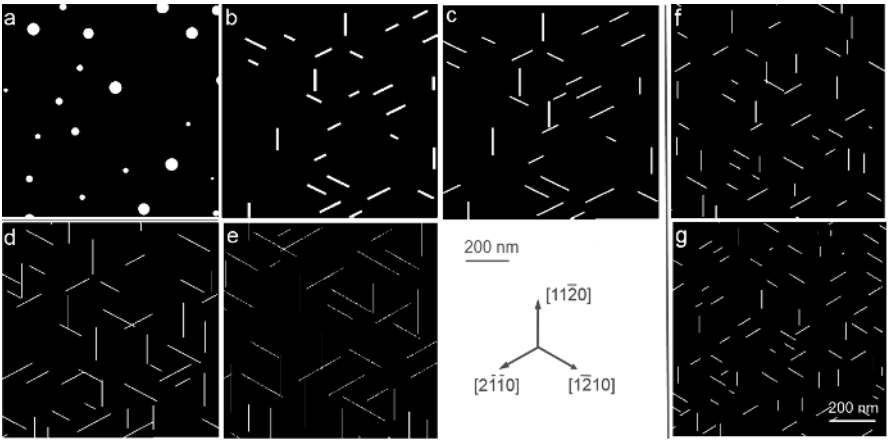

Fig. 4 Microstructures constructed to examine the effect of precipitate aspect ratio and number density on ΔCRSS increment. In figures (a)-(e), the volume fraction and number density of precipitates in each figure equals to those of β_1 in samples aged for 3 hours at 200°C. The precipitate aspect ratio is approximately (a) 1:1, (b) 10:1, (c) 20:1, (d) 40:1 and (e) 60:1. In figures (f) and (g), the volume fraction and aspect ratio of precipitates are identical to those of β_1 in samples aged for 3 hours at 200 °C, and the a number density of the distributions of precipitates are (f) 4252, and (g) 8504 μm^{-3}. Viewing direction is parallel to $[0001]_\alpha$.

Table II ΔCRSS (MPa) values for different A and N_v

Aspect Ratio (A)	1:1	10:1	20:1	40:1	60:1
Random Spatial Distribution	52.35 ± 4.40	60.50 ± 6.05	67.45 ± 6.60	83.00 ± 7.20	124.70 ± 8.65
Regular Spatial Distribution	65.42 ± 3.70	76.58 ± 4.76	91.14 ± 5.20	110.66 ± 6.51	157.80 ± 5.25
μ	0.80	0.79	0.74	0.75	0.79

Number Density (μm^{-3})	N_v (2126)	$2N_v$ (4252)	$4N_v$ (8504)
Random Spatial Distribution	62.45 ± 5.85	82.32 ± 8.14	116.57 ± 6.80
Regular Spatial Distribution	83.26 ± 2.20	108.31 ± 3.05	143.83 ± 4.20
μ	0.75	0.76	0.81

Therefore, μ values are fluctuated around 0.75. To test whether or not μ varies when N_v/A of precipitates increases, similar computation methods are repeated and calculation results of $\overline{\Delta\tau}$ and μ are listed in Table II. The results indicate that, when N_v/A of precipitates increases, the value of μ still fluctuates around 0.78 (between 0.74 and 0.81).

Summary

Assuming all β_1 precipitates are non-shearable, in the present study, quantitative effects of the distribution and morphology of coherent β_1 precipitate plates on ΔCRSS values are simulated by the phase field dislocation model.

The results of is study indicates that the ΔCRSS values of the Mg-Nd alloy aged for 3 hours at 200°C computed by the phase field dislocation model are in excellent agreement with the ΔCRSS values predicted by previous modified Orowan-looping equations [13]. The simulation results indicate that, when the aspect ratio or number density of β_1 plates increases, the effective inter-precipitate spacing decreases and a higher applied stress is needed for a dislocation to glide through the β_1 precipitate forest. The simulation further suggests that, when the plate aspect ratio increases from 13:1 to 40:1 or 60:1, the ΔCRSS increases by 1.32 or 2.00 times, and that, when the precipitate number density increases by a factor of 2 or 4, the ΔCRSS increases by 1.31 or 1.86 times.

The phase field simulation also demonstrates that, when the average diameter of β_1 plates is constant, the change of ΔCRSS is not sensitive to the variation of β_1 plate diameter distribution. For a given volume fraction of β_1 plates, a random spatial distribution of the β_1 plates can give rise to a ΔCRSS value that is 0.78 times of that corresponding to a regular spatial distribution.

Acknowledgements
The authors are grateful to the support from the Australian Research Council. H.L. wishes to acknowledge the support from Monash University in the form of Monash Graduate Scholarship and International Postgraduate Research Scholarship. H.L. also wishes to acknowledge Yuman Zhu for providing of Fig. 1a.

References

[1] J.F. Nie, "Precipitation and Hardening in Magnesium Alloys" *Metall. Mater. Trans. A*, 43A (2012) 3891-3939.
[2] J.F. Nie, B.C. Muddle, "Characterisation of Strengthening Precipitate Phases in a Mg-Y-Nd Alloy", *Acta Mater.* 48 (2000) 1691-1703.
[3] U.F. Kocks, "A Statistical Theory of Flow Stress and Work Hardening", *Phil. Mag.* 13 (1965) 541-566.
[4] M.F. Ashby, "Results and Consequences of a Recalculation of the Frank-Read and the Orowan Stress", *Acta Metall.* 14 (1966) 678-680.
[5] D.J. Bacon, U.F. Kocks, R.O. Scattergood, "The Effect of Dislocation Self-Interaction on the Orowan Stress", *Phil. Mag.* 28 (1973) 1241-1263.
[6] D. Hull, D.J. Bacon, *Introduction to Dislocations.* 5th Ed. Oxford: Elsevier; 2011.
[7] C. Shen, Y. Wang, "Phase Field Model of Dislocation Networks", *Acta Mater.* 51 (2003) 2595-2610.
[8] Z. Pei, L.F. Zhu, et. al., "Ab-initial and Atomistic Study of Generalized Stacking Fault Energies in Mg and Mg-Y Alloys" *New J. Phys.*15 (2013) 043020-043039.
[9] A.G. Khachaturyan, *Theory of Structural Transformations in Solids*, John Wiley & Sons, New York, 1983.
[10] C. Shen, Y. Wang, "Effect of Elastic Interaction on Nucleation: I. Calculation of the Strain Energy of Nucleus Formation in an Elastically Anisotropic Crystal of Arbitrary Microstructure", *Acta Mater.* 59 (2011) 3484-3497.
[11] N. Zhou, C. Shen, et. al., "Modelling Displacive-Diffusional Coupled Dislocation Shearing of γ' Phase in Ni-base Superalloys", *Acta Mater.* 55 (2011) 5369-5381.
[12] S.M. Allen, J.W. Cahn, "A Microscopic Theory for Anti-phase Boundary Motion and its Application to Antiphase Domain Coarsening", *Acta Mater.* 27 (1979) 1085.

[13] A.W. Zhu, E.A. Starke, “Strenthening Effect of Unshearable Particles of Finite Size: a Computer Experimental Study”, *Acta Mater.* 47 (1999) 3263-3269.

3rd World Congress on Integrated Computational Materials Engineering (ICME 2015)
Edited by: Warren Poole, Steve Christensen, Surya R. Kalidindi, Alan Luo, Jonathan D. Madison, Dierk Raabe, and Xin Sun
TMS (The Minerals, Metals & Materials Society), 2015

APPLICATION OF MULTI-SCALE FATIGUE MODELS IN LIGHTWEIGHT METAL CASTINGS

Qigui Wang

Materials Technology, GM Global Powertrain Engineering, Pontiac, MI USA

Keywords: Multi-Scale Fatigue Models, Life Prediction, Lightweight, Metal Castings

Abstract

Lightweight metal castings are increasingly used in critical structural applications which are often subjected to cyclic loading during service. Fatigue property of the lightweight metal castings has become a critical design criterion. Fatigue performance of lightweight metal castings strongly depends upon the presence of casting flaws and characteristics of microstructural constituents. The existence of casting flaws significantly reduces fatigue crack initiation life. In the absence of casting flaws, however, crack initiation occurs at the fatigue-sensitive multi-scale microstructural constituents. This paper discusses the recently-developed multi-scale fatigue (MSF) models and their applications in lightweight aluminum and magnesium castings.

Introduction

Fatigue properties of lightweight metal castings, like cast Al and Mg components, are strongly dependent upon the existence of flaws, such as porosity and oxide films produced during casting [1-27]. In fact, the maximum flaw size has been recognized as the most important parameter in determining the fatigue properties of lightweight metal castings, where generally the larger the maximum flaw size, the lower the fatigue strength for a given fatigue life [8,11,26,27]. In the presence of casting flaws, the fatigue initiation life is negligible and the total fatigue life is spent in propagation of a fatigue crack from such flaws. In the absence of casting flaws or when the pores and oxide films are smaller than a critical size, the cracked/debonded second phase particles and persistent slip bands become the fatigue crack initiation sites [4,10,13,14]. In these cases, the cycles spent on crack initiation by cracking or debonding the second phase particles or forming persistent slip bands can significantly increase the total fatigue life.

Like other engineering materials, fatigue life of lightweight metal castings consists of two parts: fatigue crack initiation life and fatigue crack propagation life. The fatigue crack propagation life can be further divided into short fatigue crack propagation life and long fatigue crack propagation life. The total fatigue life, N_t, can then be expressed as follows [3-4, 28]:

$$N_t = N_i + N_s + N_l \quad (1)$$

where N_i, N_s, and N_l are number of cycles for crack initiation, microstructurally and physically short crack propagation and long crack growth, respectively. The long crack propagation life N_l can be predicted by integrating the crack growth rate [4-6,10,11,26]. Crack growth rates are related to the applied stress and flaw size by the stress intensity factors such as ΔK, ΔK_{max}, ΔK_{th}, K_c (K_{IC}) defined by linear elastic fracture mechanics (LEFM). However, quantitative characterization of N_i and N_s remains challenging. LEFM is not applicable to crack initiation, and short crack propagation rates are unpredictable because of sensitivity to local microstructures at the crack tip

and violation of the assumptions of homogenous and isotropic material at the crack tip. In the past three decades, great effort has been focused on the understanding of crack initiation and short crack behavior in lightweight metal castings as well as their life predictions [2, 6-9]. This paper presents the multi-scale fatigue (MSF) models recently developed to estimate the fatigue life of lightweight metal castings spent in both crack initiation and propagation from the multi-scale casting flaws, the cracked/debonded second phase particles and persistent slip bands (PSB) [10]. To demonstrate the model applicability, both aluminum and magnesium alloy castings with various degrees of casting flaws and microstructure constituents are used.

Multi-Scale Fatigue (MSF) Life Models

Life prediction of lightweight metal casting components is always challenging not only because of uncertainty of flaw population, but also because of the complexity of primary and second phase structure as well as nano-scale precipitate structure. At GM, multi-scale fatigue (MSF) life models have been developed to predict fatigue life of cast aluminum and magnesium components with various degrees of porosity, oxides films and microstructural features [27]. When pore and oxide sizes are larger than competing microstructural weak links (such as second phase particles), crack initiation life can be ignored. When the flaw size in the casting approaches the microstructural feature size (such as grain or dendritic cell size: ~25-50 μm), however, crack initiation life from microstructural constituents such as persistent slip bands can dominate the total fatigue life.

Fatigue Crack Initiated from Casting Flaws

Fatigue cracks usually initiate from flaws in metal castings. The cycles for crack initiation can be ignored ($N_i \cong 0$) and fatigue life is mainly spent in crack propagation. When the equivalent flaw size is large than a critical size, which depends on the microstructure, the fatigue life can be simply predicted using [26,27]:

$$N = N_i + N_p = N_p = C_1 \sigma_a^{-m} a_{eq}^{-(m-2)/2} \tag{2}$$

When the equivalent flaw size is less than the critical size, the fatigue life can be predicted using:

$$N = N_i + N_p = N_p = C_2 \left(\varepsilon_{\max} \sigma_a \sigma_{ys}^{-1}\right)^n a_{eq}^q \tag{3}$$

where C_1, C_2, m, n, and q are constants; σ_a is the stress amplitude; σ_{ys} is yield strength; ε_{max} is the maximum total strain during loading cycle; and a_{eq} is the equivalent initial crack-like flaw size.

Fatigue Crack Initiated from Second Phase Particles

In Coarse Microstructure

In coarse microstructure (large SDAS, secondary dendrite arm spacing, > 50 μm), the dendrite cell walls act as grain boundaries because they are surrounded by a nearly continuous array of second phase particles. The sizes of second phase particles are similar to the dendrite arm spacing, especially in the unmodified microstructure. The fatigue life ($N = N_p$) can be predicted by a short crack propagation model assuming that a fatigue crack initiated from a second phase particle at the first cycle ($N_i = 0$) [24].

$$N = N_i + N_p = N_p = C_3 \left(\varepsilon_{\max} \sigma_a \sigma_{ys}^{-1}\right)^n d_{eq}^q \tag{4}$$

where C_3, n, and q are constants; σ_a is the stress amplitude; σ_{ys} is yield strength; ε_{max} is the maximum total strain during loading cycle; and d_{eq} is the equivalent initial crack-like second phase particle size.

The criterion for cracking or decohesion of second phase particles is given as [27]:

$$\sigma_p = 4\varphi\beta\alpha^t \mu_m \gamma^*_{\max} \tag{5}$$

where σ_p is fracture strength of second phase particle; $\gamma^*_{\max}$ is the critical maximum local shear strain, below which fatigue crack initiates by decohesion; α is the particle aspect ratio; t is a constant between 0 and 1; φ is an "accommodation factor" equal to the elastic strain in the particle divided by the plastic strain in the matrix; φ depends on the morphology of particles and the slip system of the matrix, and is equal to 0.393 for spheres and 0.75 for plates in a matrix deforming by multiple slip; β is the modulus correction factor to account for elastic inhomogeneity; μ_m is the shear modulus of the aluminum matrix.

In Fine Microstructure

In fine microstructure (small SDAS, < 50 μm), the small dendrites and fine second phase particles make the dendrite cell boundaries more discontinuous. As a result, dislocations can move across the cell boundaries and the slip distance of dislocations is increased from one SDAS to the scale of the grain size. In this case, fatigue cracks often initiate from decohesion of second phase particles and then quickly propagate to a grain size by cyclic plastic shear. The crack initiation life (N_i) can be estimated by [27]:

$$N_i\left(\Delta\varepsilon^p_{eq}\right)^e = C_4\left(d_g\right)^f \tag{6}$$

The cycles required to propagate the crack from one grain size to final failure can be estimated using long crack model as shown in Eqn. (2). Therefore, for fine microstructures the total fatigue life (N) can be calculated by [27]:

$$N = N_i + N_p = C_4\left(\Delta\varepsilon^p_{eq}\right)^{-e}\left(d_g\right)^f + C_5\sigma_a^{-m}\left(d_g\right)^{-(m-2)/2} \tag{7}$$

where $\Delta\varepsilon^p_{eq}$ is local equivalent plastic strain; d_g is equivalent grain size; e, f, C_4, C_5, and m are constants.

Fatigue Crack Initiated from Persistent Slip Bands

In Coarse Microstructure

In coarse microstructure with SDAS > 50 μm, persistent slip bands (PSB) can form in favorably oriented grains, particularly close to the grain boundaries near the free surfaces of the component. Because the cell boundaries are outlined with nearly continuous second phase particles, the cell size defines the slip distance for crack initiation. Once a PSB is formed, the fatigue cracks initiated from notch-like PSB on the free surfaces of the component can quickly propagate across the dendrite cells. The crack initiation life can be estimated by [27]:

$$N_i = C_6\left(\Delta\varepsilon^p_{eq}\right)^{-g}\left(\lambda_{eq}\right)^h \tag{8}$$

The cycles to propagate the crack from one dendrite cell size to final failure (N_p) can be estimated using a short crack model. The total fatigue life can thus be calculated by [27,28]:

$$N = N_i + N_p = C_6\left(\Delta\varepsilon_{eq}^{p}\right)^{-g}\left(\lambda_{eq}\right)^{h} + C_7\left(\varepsilon_{\max}\sigma_a\sigma_{ys}^{-1}\right)^{s}\left(\lambda_{eq}\right)^{t} \quad (9)$$

where λ_{eq} is equivalent circle diameter of dendrite cell size; C_6, C_7 , g, h, s, and t are material-related constants.

In Fine Microstructure

In fine microstructures (small SDAS, < 50 μm), the density of second phase particles in the dendrite cell boundaries is low and dislocations can move across the cell boundaries until they are blocked at the grain boundaries. In this case, the characteristic microstructure feature constraining slip is the grain size. The fatigue life of cast aluminum and magnesium components failed by slip bands can be estimated by Equation (7).

Application of MSF Life Models

Multi-scale fatigue (MSF) models have been used to estimate the fatigue life of cast aluminum and magnesium alloys. A comparison of the calculated propagation life based on short crack model (Equations (3)) and the empirical constants, to actual fatigue life (N_f) is made in Fig. 1a. The calculated N_P is in good agreement with the actual fatigue life N_f. This indicates that the total fatigue life of castings failing from porosity is mainly comprised of crack propagation, and the assumption that initiation life is near zero is reasonable. Similar results were reported by Caton *et al.* [9].

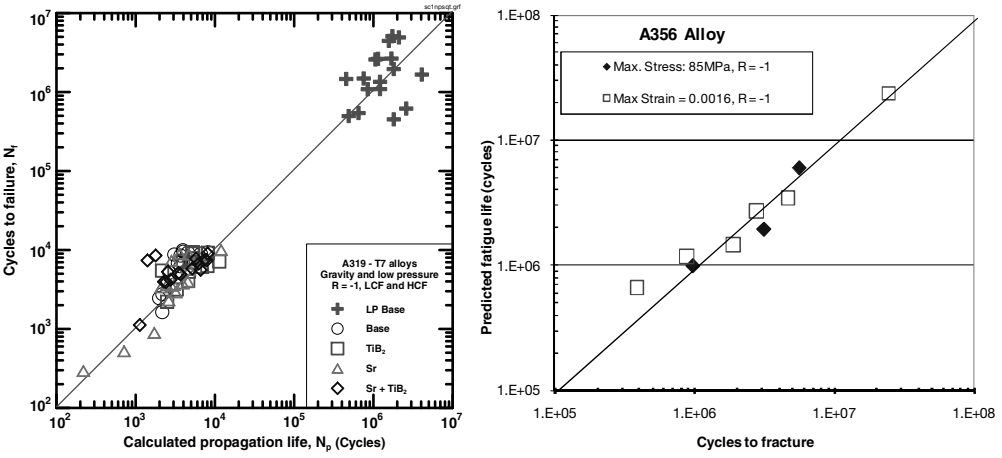

(a) (b)

Fig. 1. Comparison of the predicted and actual fatigue life (N_f) in aluminum castings. (a) 319 samples failed by porosity and (b) A356 samples failed by the cracked and debonded second phase particles [27].

Fig. 1b shows a comparison of the calculated fatigue life of cast aluminum A356 samples failed by cracked and debonded second phase particles based on Equations (4) and (7) with actual fatigue

life. In the two sets of data shown in the figure, the samples tested at the stress amplitude of 85MPa and stress ratio R = -1 have coarse unmodified microstructures (SDAS: 55~70 μm) and large Si and Fe-rich particles. The fatigue cracks in all three samples were initiated by cracked Si and Fe-rich particles so Equation (4) was used to calculate the fatigue life. For samples tested under maximum strain amplitude of 0.0016 and stress ratio R = -1, Equation (7) was employed since these samples have fine microstructures (SDAS: 15~30 μm) and fatigue cracks were initiated by decohesion of second phase particles followed by quick propagation to a grain size. It should be noted that the calculated fatigue life shown in the figure is based on nominal characteristic size (equivalent circle diameter, ECD) of second phase particles and dendrite grains. It can be seen that the calculated fatigue life is in good agreement with the actual fatigue life.

A comparison of the calculated fatigue life of samples failed by persistent slip bands in both coarse (SDAS: 70μm) and fine (SDAS: 20μm) microstructure with actual fatigue life is made in Figs. 2 and 3 with cast aluminum alloys. Fatigue life curves predicted from the coarse microstructure (SDAS: 70μm) by Equation (9) are compared to experimental data points in Figure 2, while Figure 3 compares the predicted fatigue life curves for a fine microstructure calculated by Equation (7) to experimental data. Solid lines represent total calculated fatigue life consisting of initiation life (N_i) and propagation life (N_p) which are shown as dashed lines. The upper, median, and lower solid lines in each figure show the stress-life relationships for castings with the characteristic microstructure sizes of median-3 Sigma, median, and median+3 Sigma, respectively. It can be seen that the predicted fatigue life is in good agreement with the actual fatigue life. By considering the probabilistic distribution of characteristic microstructures (median +/- 3 sigma SDAS or grain size), the model can accurately predict the variation and scatter of the fatigue life data.

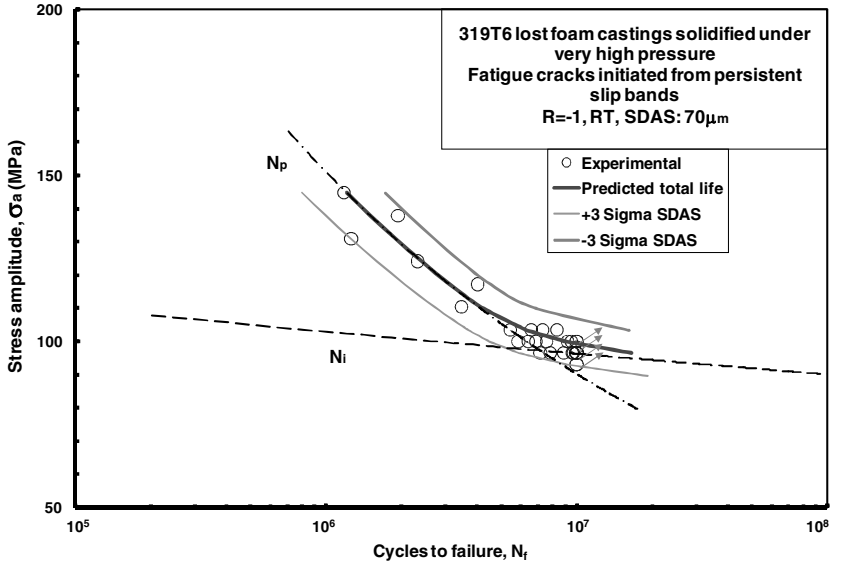

Fig. 2. Comparison of actual fatigue life (N_f) of 319T7 alloy samples failed by slip bands with the calculated life based on Equation (9). Arrows indicate runout samples which did not fail after 10 million cycles [27].

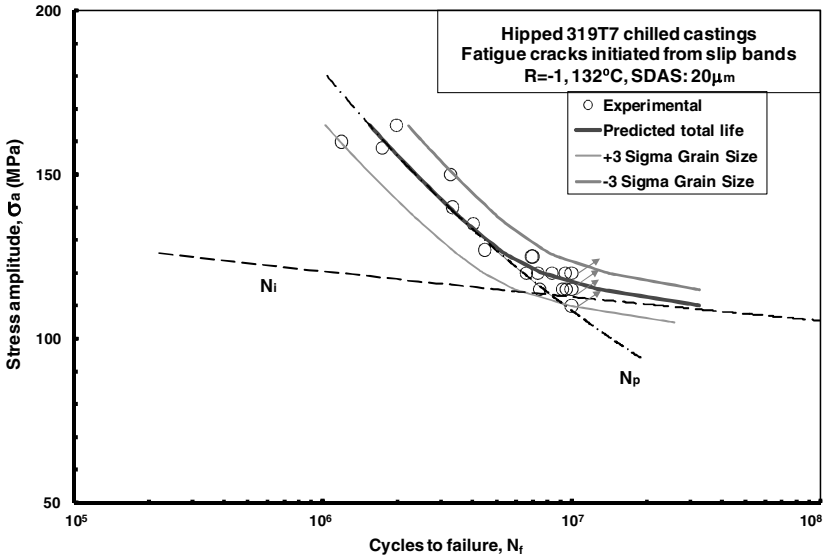

Fig. 3. Comparison of actual fatigue life (N_f) of 319T7 alloy samples with crack initiation by slip bands with the calculated life based on Equation (7). Arrows indicate runout samples which did not fail after 10 million cycles [27].

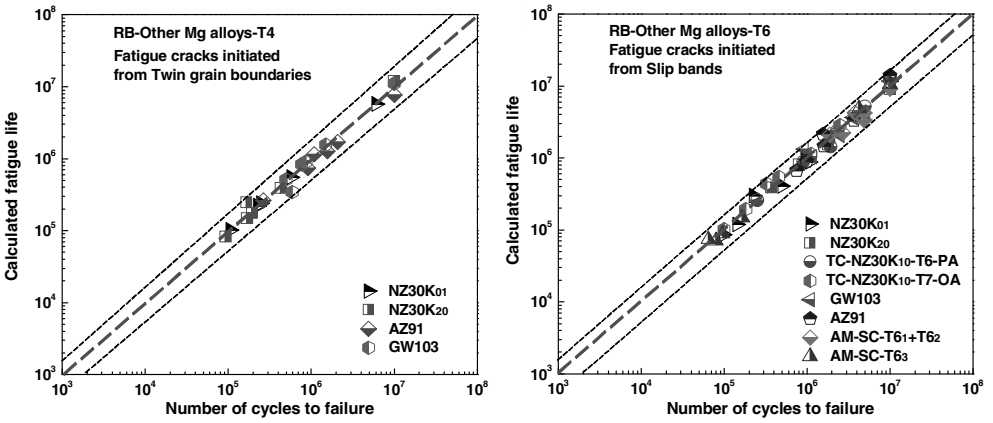

(a) (b)

Fig. 4. Comparison of the actual fatigue life measured with the calculated fatigue life for various Mg alloys under (a) T4 and (b) T6 heat treatment conditions. The fatigue test is the rotating bending test (RB) at room temperature. [29]

Similar results have been obtained in cast magnesium alloys after comparing the calculated fatigue lives with actual measurements, Fig. 4 [29]. In defect-free cast magnesium alloys studied, the

calculated fatigue lives shown in the figure are based on nominal characteristic sizes (equivalent circle diameter, ECD) of grains and fatigue life model in Equation (9). It is seen that the calculated fatigue lives are in good agreement with the actual fatigue lives measured. The selection of grain sizes as characteristic microstructure feature extremes is appropriate for estimating fatigue life of cast magnesium alloy with less or no casting flaws.

In lightweight metal castings, casting flaws and microstructure features such as porosity, oxides, second phase particles and dendrite cell and grain structures are not uniform in the entire stressed volume due to randomness in the nucleation and growth of casting flaws and microstructure features during local solidification. It is generally accepted that the characteristic flaw and microstructure features in metal castings follow extreme value probabilistic distributions. [26,27,30] The upper tail populations in these distributions dominate the fatigue behavior. In the presence of second phase particles, inhomogeneous deformation during cyclic loading results in high internal stress in the particles due to dislocation pileups at particles. The larger the particle, the higher the internal stress. When internal stress is greater than the particle fracture strength, the particle cracks. Otherwise, decohesion occurs when the internal stress is higher than interfacial strength between the particle and matrix. Cracking or decohesion of second phase particles can happen in the first few cycles particularly when the second phase particle are segregated and located in the high stress areas. If the cracked particle size or the debonded particle area is comparable to characteristic microstructure sizes such as dendrite cells (in coarse microstructure) or grain size (in fine microstructure), then the fatigue crack immediately propagates like a long crack. Otherwise, the fatigue crack behaves like a short crack and persistent slip bands (PSB) can form in favorably oriented grains or dendrite cells, particularly close to the grain or boundaries near the free surfaces of the component. In this case, a substantial portion of fatigue life is spent in crack initiation and small crack propagation which must be included in the total life estimates.

Summary

The fatigue life of lightweight metal castings failed by various crack initiation mechanisms can be calculated using the presented multi-scale fatigue (MSF) models together with the flaw population and microstructure characteristics. Like casting flaws, the characteristic microstructure dimensions can be estimated by the extreme value statistics. Good agreement between the measured and the calculated fatigue lives has been shown in this paper for both aluminum and magnesium castings over a range of microstructural scales and flaw populations.

Acknowledgments

The author would like to acknowledge the support of his organization. Special thanks are extended to Drs. Peggy Jones, Dale Gerard, and Yucong Wang for their valuable discussions during the course of this work.

References

1. Laz, P.J., *Int. J. Fatigue* 4 (1998), 263-270.
2. Mayer, H., *Int. J. Fatigue*, 25 (2003), 245-256.

3. Wang, Q.G., Apelian, D. and Griffiths, J.R., in *Advances in Aluminum Casting Technology*, eds: M. Tiryakioglu and J. Campbell (ASM International, Materials Park, OH, 1998), 217-224.
4. Barsom, J.M. and Rolfe, S.T., *Fracture and fatigue control in structures* (3rd ed. ASTM. 1999), 196-197.
5. Stephens, R.I., *Metal Fatigue in Engineering* (2nd ed. John Wiley and Sons, inc. 2001), 144-156.
6. Stanzl-Tschengg, S.E., *Int. J. Fatigue*, 17(2) (1995) 149-155.
7. Avalle, M., *Int. J. of Fatigue*, 24 (2002), 1-9.
8. Wang, Q.G., Apelian, D., Lados, D., *Journal of Light Metals*, 1 (2001), 73-84.
9. Caton, M.J., Jones, J.W., Boileau, J.M. and Allison, J.E., *Met Mater Trans A*. 30A (1999), 3055-3068.
10. Buffiere, J.Y., Savelli, S. and Jouneau, P.H., *Materials Science and Engineering A*, 316 (2001), 115–126.
11. Couper, M.J., Neeson, A.E., Griffiths, J.R., *Fatigue Fract. Engng Mater.Struct*, 3 (1990), 213-227.
12. Chan, Kwai S., Jones, P.E., Wang, Q.G., *Materials Science and Engineering A*, 341 (2003), 18-34.
13. Wang, Q.G., Apelian, D., Lados, D., *Journal of Light Metals*, 1 (2001), 85-97.
14. Han, Sang-Won, Kumai, Shinji and Sato, Akikazu, *Materials Science and Engineering A*, 332 (2002), 56–63.
15. Lee, Min Ha, Kim, Jae Joong, Kim, Kyung Hoon, *Materials Science and Engineering A.* 340 (2003), 123-129.
16. Lados, Diana A. and Apelian, D., *Materials Science and Engineering A*, 385 (2004), 200-211.
17. Yi, J.Z., Gao, Y.X., Lee, P.D. and Lindley, T.C., *Materials Science and Engineering A*, 386 (2004), 396-407.
18. Verdu, C., Cercueil, H. and Communal, S., *Mater. Sci. Forum*, 217 (1996), 1449.
19. Evans, W.J., Jones, H.V., Spittle, J.A., Brown, S.G.R., in: H. Oikawa (Ed.), in Proceedings of the 10th Conference on the Strength of Materials (The Japan Institute of Metals, Sendai, 1994), 501.
20. Call, K., *Fatigue Fract Eng, Mater Stuct.,* 23 (2000), 159-172.
21. Lee, F.T., Major, J.F., Samuel, F.H., *Fatigue Fract. Eng. Mater. Struct*, 18 (3) (1995), 385-396.
22. Lee, F.T., Major, J.F., Samuel, F.H., *Metall, Mater, Trans, A*, 26 (1995), 1553-1570.
23. Laird, C., in *Fatigue Crack Propagation* (ASTM STP 415. ASTM), 196, 131-168.
24. Hussain, K., Engineering Fracture Mechanics, 4 (1997), 327-354.
25. Socie, D.F., Exp. Mech., 17 (1977), 50
26. Wang, Q.G. and Jones, P.E., Metall. Mater. Trans. B, 38 (4) (2007), pp. 615-622.
27. Wang, Q.G. and Jones, P.E., *U.S. Patent* 7623973 B1 (No. 24, 2009)
28. Suresh, S., Fatigue of Materials, Eds.: E.A. Davis and I.M. Ward, Cambridge University press (1991).
29. Zhenming Li, Qigui Wang, Alan A. Luo, Penghuai Fu, Liming Peng, submitted to Intl J. of Fatigue, 2015.
30. Murakami, Y. and Endo, M., *Int. J. Fatigue*, 16 (1994), 163-182.

3rd World Congress on Integrated Computational Materials Engineering (ICME 2015)
Edited by: Warren Poole, Steve Christensen, Surya R. Kalidindi, Alan Luo, Jonathan D. Madison, Dierk Raabe, and Xin Sun
TMS (The Minerals, Metals & Materials Society), 2015

EXPERIMENTAL VERIFICATION FOR SOLID FRACTION MEASUREMENT IN SEMI-SOLID SILVER METAL PROCESSING IN COMPARISON WITH THEORETICAL THERMODYNAMICS MODEL

Pun Wirot[1,2], Boonrat Lohwongwattana[2], Ekasit Nisaratanaporn[2]

1Graduate student, Faculty of Engineering, Chulalongkorn University, Bangkok, 10330,Thailand
2 Corresponding author, Innovative Metals Research Unit, Faculty of Engineering, Chulalongkorn University, Bangkok, 10330, Thailand

Keywords: Semi-solid processing, sterling silver, thermal analysis, thermodynamic models

Abstract

The actual volume fraction of the solid in semi-solid metal processing is critical to achieving the most effective semi-solid metal processing. The semi-solid slurry with different solid fractions shows different ability to fill molds. To determine suitable processing conditions for semi-solid sterling silver (92.5 wt.%), thermal analysis (TA), experimental verification in actual investment casting machine as well as thermodynamics models were performed. Classical Gibbs free energy calculation and Scheil-Gulliver modeling were used to estimate the relationship between solid fraction and temperature. In order to obtain the relationship between temperature and solid fraction, comparisons were made amongst different techniques. The investigated 925 silver alloy was heated to 950 ^{o}C, and gas bubbling apparatus was used to introduce argon gas into the melt. Cooling curves for the metal were recorded with two thermocouples, one at the center of the melt volume and one beside the containing crucible wall. Different cooling curves and temperature profiles are presented from various tests to compare solid fractions. It was found that the latent heat of fusion strongly affected the solid fraction in addition to thermodynamic contribution. To adequately express the solid fraction relationship, the thermodynamics modeling needed modifications that took into account the cooling effects as well as temperature gradient in the crucible.

1.Introduction

Sterling silver is an alloy comprising of 92.5% silver by mass and 7.5% of other metals by mass, most of the time, copper is mainly used in the jewelry industry. Silver jewelry manufacturing commonly uses investment casting or lost wax-casting technique [1] that has many drawbacks. One of the reasons behind these downsides is mould, which is generally formed from investment or plaster that has poor thermal conductivity and consecutively could lead to poor mechanical properties of specimen namely hardness and ultimate tensile strength[2].

Semi-solid casting has been developed around the 19th century [3] with the intention to improve mechanical properties of aluminum alloys from casting process [4]. Semi-solid casting process takes place when the molten metal has partially transformed into semi-solid or slurry prior to casting into the mould. The semi-solid casting process has been developed for silver casting by gas induced semi-solid process (GISS) [5]. The GISS process utilizes the principle of rapid heat extraction and vigorous local stirring using the injection of fine gas bubbles through a graphite diffuser.

In this work, solid fraction is determined by thermal analysis (TA) with computer-aided cooling curve analysis (CA-CCA) [6, 7] as comparative characterization method. The methodology, allows for understanding of a melt batch via recording of phase change temperatures. The amount of heat evolving from solidification is further calculated into solid fraction under the relationship between first derivative curve (dT/dt) normalized and a base line. The calculated solid fractions were compared with thermodynamics models.

2. Experimental procedures

2.1 Preparation of 925 silver alloys

925 silver alloys was prepared by granulation technique. Commercial-grade high purity (99.99%) silver was melted in graphite crucible inside an induction furnace under argon environment. Heraeus-7.25wt.% Master alloys (H925) was successively added into the molten metal at 1000 ^{0}C with rigorous stirring for 10 minutes. Then the molten metal was granulated into cold water tank. Droplets of liquid metal were immediately solidified. The chemical composition was analyzed by using ICP-AES. An averaged result is tabulated shown in Table 1.

Table 1 Average chemical composition of 925 silver alloys

	Element (wt.%)				
	Ag	Cu	Zn	Sn	Si
925Silver Alloys	93.930	4.410	1.600	0.050	0.007

2.2Thermal Analysis

2.2.1Cooling curve

350-gram of granulated silver alloy was placed in graphite crucible then heated to a temperature of 950 ^{o}C by using induction casting machine, INDUTHERM VC 600. The atmosphere has been vacuumed and argon flushed for three times before five minutes melting in argon atmosphere. In order to record and verify a cooling curve, two thermocouples were installed at the center and the inner-wall of the crucible. The experiments were separated into two conditions with and without gas bubble. For the gas bubbling condition, argon gas was fed with rate of 1 liter/minute into the molten metal through porous graphite diffuser until the metal is fully solidified. During each cooling cycle, raw data such as temperature and time was recorded by a data logger (Pico Tech) from 950 ^{o}C to 500 ^{o}C.

Figure1. Schematic for thermal analysis experiment set-up

2.2.2 Solid fraction and baseline

Initiation of transformation can be obtained from cooling curve. This method is originally described in 1984 by Stefanescu [5] having four simplifying assumptions; (1) internal conduction of the sample can be ignored, (2) volumetric specific heat of the metal remains constant, (3) releases of latent heat rate for each phase transformation are equal, and (4) rate of heat extraction from the sample can be described by a Cauchy type boundary condition. The solid fraction (f_s) was defined by a following equation.

$$f_s = \frac{\int_{t_l}^{t}[\left(\frac{dT}{dt}\right)_{pt} - \left(\frac{dT}{dt}\right)_{npt}]dt}{\int_{t_l}^{t_s}[\left(\frac{dT}{dt}\right)_{pt} - (\frac{dT}{dt})_{npt}]dt}$$

where the subscripts on the differential pt and npt refer to phase transformation and no phase transformation respectively. Base-line curve which represents no phase transformation can be estimated by a third order polynomial curve fitting.

2.3 Thermodynamics model

Two types of thermodynamics models were employed. First is the classical Gibbs free energy calculation with lever-rule. This model assumes that the equilibrium of solidification has very slowly cooled with complete diffusion in the liquid state and complete diffusion in the liquid and complete equilibrium in the solid.

The second model is Scheil-Gulliver, which assumes that there is no diffusion in solid phases, no diffusion in the solid phases, infinitely rapid diffusion in the liquid phase, and local equilibrium at the solid/liquid interface.

Figure2 shows a liquidus projection of Ag-Cu-Zn alloys and a solidification path of Sterling silver alloys at a composition of 4.4 %wt. copper, 1.6 %wt. zinc and balance silver. In this ternary system, from the beginning to the end of solidification, there are three possible events, primary crystallization of face centered cubic silver, secondary crystallization of Cu-phase and finally a eutectic reaction. The list of is shown in Table 2.

2.4 Microstructure

First the wax patterns were prepared and installed into wax tree inside a flask. The flask was then filled with investment. Subsequently the flask was heated in steps to rid of the wax and to cure the investment. The final temperature was 600 ^{o}C. Two main conditions were utilized for comparative study. First, the conventional as-cast tree to be used as controlled set of specimens, was cast at 950 ^{o}C assuring a complete liquid melt. Second, the semi-solid casting was employed by casting the semi-solid slurry into a flask mould after feeding the argon gas for 15 seconds into the molten metal.

Samples for the microstructure were cross-sectioned then ground to mirror finish, and finally polished with mixture of 10 grams Chromium trioxide, 10 ml sulfuric acid and 1000 ml distilled water. Grain size and metallographic studies of the samples were carried out by optical microscope and scanning electron microscope.

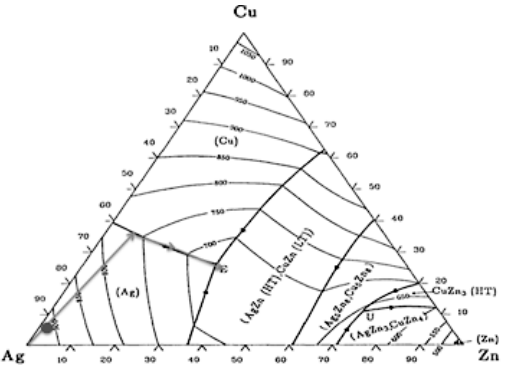

Figure2. Liquidus projection of Ag-Cu-Zn alloys and the solidification path of sterling silver alloys [8]

Table 2 List of the reaction identified from solidification path

ID#	Transformation
1	Start of solidification of $\propto -Ag$ (liquidus)
2	Maximum growth of primary $\propto -Ag$ phase
3	Start of solidification of $\beta - Cu$
4	Maximum growth of secondary $\beta - Cu$ phase
5	Eutectic reaction of AgZn and CuZn
6	End of solidification (solidus)

3.Results and Discussion

3.1Thermal analysis and microstructure

The thermal analysis results for silver alloys in the as-cast state is shown in Figure3(a). The first derivative of the cooling curve (dT/dt) was shown. The changing of slope is related to the difference latent heat from phases as well as recalescence. The first changing of slope observed at 891 ^{o}C corresponded to the solidification of primary Ag-phase. Then the mixed signals of primary Ag-phase growth as well as recalescence were detected as temperature 745 ^{o}C when the maximum growth of the primary Ag-phase has been reached. Finally the eutectic reaction took place at 745 ^{o}C and there is mixed responses from recalescence and delay in enthalpy release as the temperature dropped down to 677 ^{o}C.

For comparison, Figure3(b) represents the temperature profile during the semi-solid casting process. Argon gas was fed into the melt at one liters per minute through porous graphite was observed at 894 ^{o}C which represented the solidification of primary Ag-phase, then the primary Ag-phase took on growth process as temperature dropped down to 788 ^{o}C. After that the eutectic reaction took over before the solidification ended at 770 ^{o}C

Comparisons between semi-solid condition and as-cast condition were further investigated. Solidus line of the semi-solid (gas bubbling) system dropped at a faster rate than the as-cast(non-bubbling gas) system as shown in table 3.This solidification process is faster under bubbling gas condition because the feeding gas had come into contact with molten metal, which in turn promoted rapid heat extraction. The heat can be exchanged faster when compared with non-bubbling gas condition. Moreover, at each local heat extraction between room-temperature argon bubble and molten metal, heterogeneous nucleation of primary Ag-phase is formed. [3]

(a1)

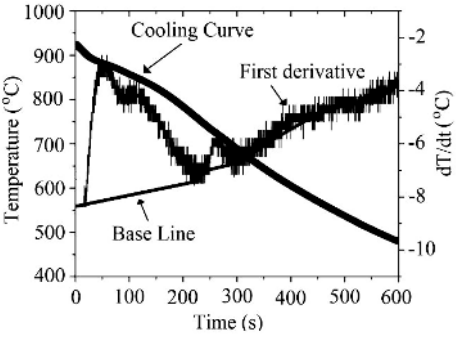

(b1)

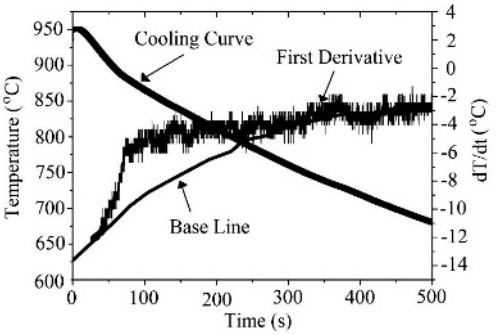

(a2)

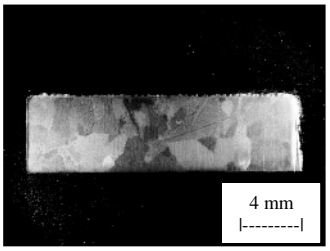

(b2)

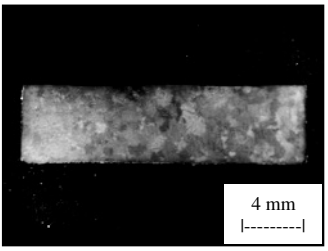

(a3) (b3)

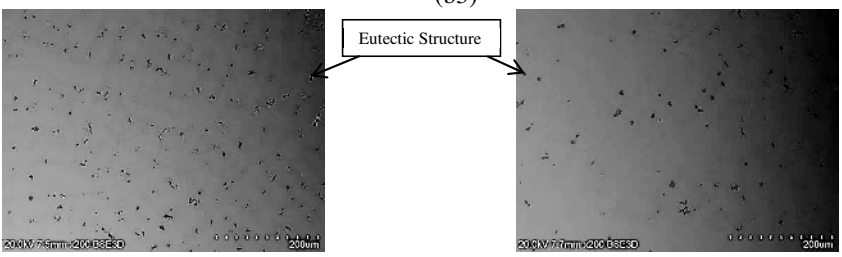

Figure3. Thermal analysis results (1) grain size (2) and microstructure (3) for (a) without gas bubble (b) with gas bubble

Grain size was also different between the two conditions. Average grain size from as-cast casting, condition was 2.60 mm while average grain size from semi-solid casting was 1.33 mm. Microstructure of as-cast state and semi-solid casting are shown in Figure(a3) and (b3). Interestingly the area fraction of eutectic structure in semi-solid casting is lower when compared with as-cast state owing to precipitated Cu.

3.2 Solid fraction curves

The relationship between solid fraction and temperature curves are shown in Figure4. Both thermal analysis and thermodynamics model have their own limitations. The limitation of thermal analysis is the latent heat signal to noise ratio. If there is low amount of latent heat, the calculation would not be accurate as the cooling curve cannot clearly identify the changing of peaks in the first derivative resulting in the missing of phase transformation. In our work, we could easily detect the formations of primary Ag-phase and eutectic phase but the peak of secondary Cu-phase precipitation. The calculation from thermodynamics models, Classical Gibbs free energy and Scheil-Gulliver from Table3 can identify all of the possible phases. However, calculation from thermodynamics model inaccurately quantified the solid fraction. This is because all of the solidification has cooling rate effect as well as the heat extraction process is becoming more complex as the molten metal solidifies. [9]

(a) (b)

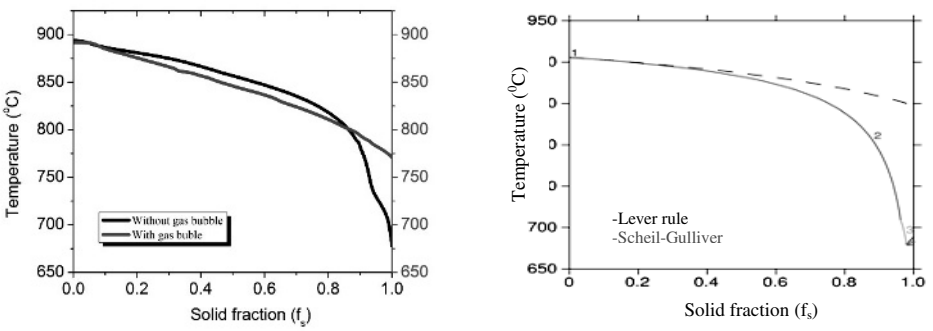

Figure4. Solid fraction vs. temperature curve for (a) thermal analysis (b) thermodynamics model

Table 3 Thermal analysis results for the temperature (^{o}C) and solid fraction (%) at critical point during solidification comparison with thermodynamic models

Methods	1	2	3	4	5	6
without gas bubble	891	745	-	-	745	677
with gas bubble	894	788	-	-	788	770
Lever-rule	906	725	725	665	665	665
Scheil-Gulliver	906	709	709	679	679	679

4.Summary

We have found that thermal analysis is a reliable technique for achieving the relationship between solid fraction and temperature. However, there is a limitation with the amount of latent heat which could lead to misinterpretation of phase transformation events. On the other hand, thermodynamics model can identify all possible phases but it cannot accurately represent the actual cooling rate. In order to have extraordinary accurate relation between solid fraction and temperature both the Thermodynamics model and thermal analysis method must performed concurrently.

Acknowledgements

The authors gratefully thank the funding from Beauty Gems Factory, The Thailand Research Fund, Thai Gem and Jewelry Traders Association, Graduate student, Faculty of Engineering, Chulalongkorn University.We also thank the Innovative Metal Research Unit team and especially Miss C.Yipyintum for all the kind supports.

References

1. Northover, S.M. and J.P. Northover, *Microstructures of ancient and modern cast silver–copper alloys.* Materials Characterization, 2014. **90**(0): p. 173-184.
2. Nisaratanaporn, E., et al., *Study on the microstructure, mechanical properties, tarnish and corrosion resistance of sterling silver alloyed with manganese.* Materials Science and Engineering: A, 2007. **445–446**(0): p. 663-668.
3. Fleming, M.C., *Behavior of metal alloys in the semisolid state [J].* Metallurgical Transactions B1991. **22B**: p. 269-293.
4. Canyook, R., et al., *Characterization of the microstructure evolution of a semi-solid metal slurry during the early stages.* Acta Materialia, 2012. **60**(8): p. 3501-3510.
5. Wannasin, J., R.A. Martinez, and M.C. Flemings, *Grain refinement of an aluminum alloy by introducing gas bubbles during solidification.* Scripta Materialia, 2006. **55**(2): p. 115-118.
6. Stefanescu, I.G.C.a.D.M., AFS Trans, 1984. **92**: p. 947.
7. Liang, S.M., et al., *Thermal analysis and solidification pathways of Mg-Al–Ca system alloys.* Materials Science and Engineering: A, 2008. **480**(1–2): p. 365-372.

8. Effenberg, G.P.a.G., *Ternary Alloys*. Vol. 1. 1988, Weinheim,Germany: VCH Verlagsgesellschaft.
9. Nafisi, S., D. Emadi, and R. Ghomashchi, *Semi solid metal processing: The fraction solid dilemma.* Materials Science and Engineering: A, 2009. **507**(1–2): p. 87-92.

3rd World Congress on Integrated Computational Materials Engineering (ICME 2015)
Edited by: Warren Poole, Steve Christensen, Surya R. Kalidindi, Alan Luo, Jonathan D. Madison, Dierk Raabe, and Xin Sun
TMS (The Minerals, Metals & Materials Society), 2015

EXPERIMENTAL AND NUMERICAL DETERMINATION OF THE FRACTURE ENERGY OF PAN/PHENOLIC-BASED CARBON/CARBON COMPOSITES

Khurram Iqbal*

State Key Laboratory of Structural Analyses for Industrial Equipment, School of Aeronautics and Astronautics, Dalian University of Technology, 116024 Dalian, China
*khurramiqbal.nust@gmail.com

Keywords: Composite material, Delamination, Finite element method, Fracture

ABSTRACT

In this paper, the validity of some formulations allowing the determination of the fracture energy of PAN/phenolic-based carbon/carbon composites has been verified. The G_{IIC} is chosen as fracture characterizing parameter which is experimentally determined by considering a multiplying form that is numerically evaluated using a finite element method. The numerical results are compared to the experimental data, and a good agreement has been observed. The specimen geometry was used to determine the mode II delamination fracture energy.

1. Introduction

Poly-acrylonitrile (PAN)/phenolic-based carbon/carbon (C/C) composites are important class of materials used for space/aviation industries due to dimensional stability, invariability of material property, high strength and rigidity, and corrosion resistance [1-4]. The versatile properties of phenolic-based carbon justify their applications as matrices in different kinds of composites [1, 3]. Some of the most important advantages are the modest price, the wide spectrum of obtainable properties, and the high carbon yields. The carbon yields allow the conversion of carbon fiber reinforced phenolic resin-based plastics (CFRP) to high temperature composites such as C/C, C/C-SiC and C/C-Cu composites [5-7]. These materials show different rigidity and strength with other composite materials due to difference in properties of fiber and matrix materials. Each composite part receives not only compression, but also bending and torsion [8-12]. During the pyrolysis [13-15] at temperature above 500°C, due to the shrinkage of the matrix and the hindering of stiff carbon fibers, the matrix experiences a tensile stress and the tensile stress applied to the matrix increases with rising pyrolysis temperature. When the tensile stress locally exceeded the tensile strength of the matrix, the first cracks appeared at the weakest sites, such as the fiber/matrix interface, pores or cracks [16-19].

In order to understand the mechanical properties of PAN/phenolic-based carbon/carbon composites; several studies have been carried out [16, 18-22]. But on the other hand, very

limited information available is on the study of interlaminar fracture toughness mode II of these composites. Therefore, this paper studies the effect of carbonization on mechanical properties of PAN/phenolic-based carbon/carbon composites. The interlaminar fracture toughness was determined by experiments. The numerical technique was conducted by using interlaminar fracture toughness data obtained from the experiments. This numerical technique was then used to interpret the variations in mechanical properties.

2. Analysis

2.1 Fracture Work

The work of fracture is calculated as the area under the load vs. displacement (P-*u*) curves as shown in Fig. 1. The test is stopped when the load drops below 0.5 kN or when the crack mouth opening displacement (CMOD) gauge range limit is reached at $u = u_c$. The work of fracture W under the experimental curve was computed using a technique called the quadrangle rule:

$$W = \sum_{i=1}^{n} (u_{i+1} - u_i).P_i + \frac{1}{2}\sum_{i=1}^{n} (u_{i+1} - u_i).(P_{i+1} - P_i) \quad (1)$$

where P_i is the applied load (N) at the i load step, P_{i+1} is the applied load (N) at the $i+1$ load step, u_i is the load line displacement (LLD) at the i step and u_{i+1} is the load line displacement (LLD) at the $i+1$ step, respectively.

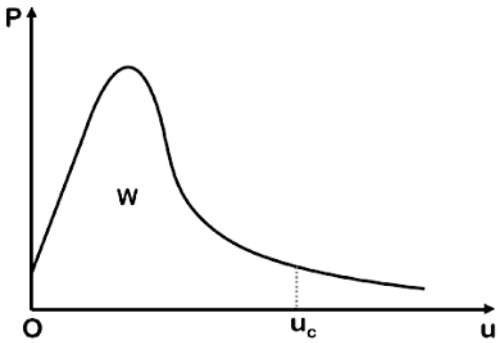

Fig. 1. Schematic diagram of Load vs. load line displacement (P-*u*) curve.

2.2 Fracture Energy

The fracture energy G_{IIC} was obtained and it was calculated by dividing the work of fracture W by the area A of the specimens:

$$G_{IIC} = \frac{W}{A} \quad (2)$$

3. Experimental

3.1 Materials

The reinforcements for carbon/carbon composites, 3 K poly-acrylonitrile (PAN)-based high strength fibers (Supplied by Toray Industries Inc., Japan) were chosen. For the matrix materials, phenolic (FB) resins (supplied by Bengbu High-Temperature Resistant Resin Factory, China) were adopted. The characteristics of the as-received materials are listed in Table I.

Table I. Characteristics of carbon fiber and FB resin.

Materials	Appearance	Composition (wt %)	Density (g/cm^3)	Tensile strength (MPa)	Tensile modulus (GPa)	Diameter (μm)
Carbon fiber	Black	C≥93	1.76	3530	230	7
FB resin	Yellow	C≥69	1.28	≥71	≥3.6	3-20

3.2 Preparation of CFRP and C/C composites

The carbon fiber reinforced phenolic resin-based plastics (CFRP) composites were manufactured by wet layup method. A composite was made by using 20 layers of the carbon fiber fabrics ($0^\circ/90^\circ$) of thickness 4 to 4.5 mm. The carbon fiber fabrics were placed into an open metallic moulds with an inner dimension of 100mm × 70mm × 60mm, and wet out with the phenolic resin using a consolidation roller. The fiber volume fraction was set to about 50% (nominal) in the CFRP composites. Before producing moulding compounds, the inner wall of metallic mould were coated with a silicon-releasing agent, and dried at room temperature for 30min. The produced moulding compounds were cured at 150°C for 10 hours. After cooling down to room temperature, the CFRP specimens were removed from the metallic moulds, and the specimens were then machined. The CFRP composites were also post-cured at 240°C in ambient atmosphere for 8 hours, and then pyrolyzed to convert into carbon/carbon (C/C) composites. Pyrolysis (carbonization step) of the CFRP composites was performed at the temperature of a 1000°C for 1 hour at the rate of 10°C/min in a nitrogen atmosphere. Schematic diagram of the fabrication method and the image for CFRP and C/C composites are shown in Fig. 2.

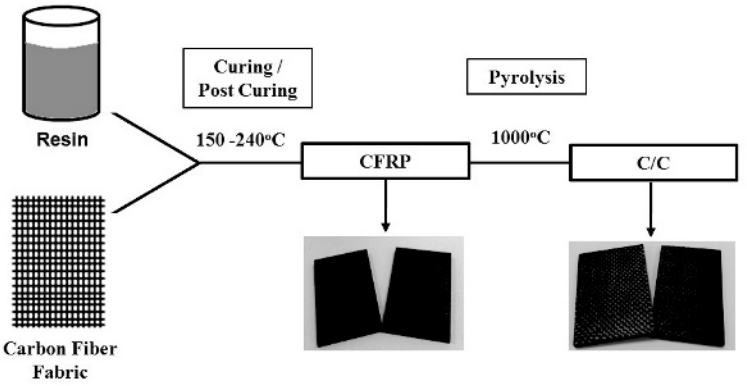

Fig. 2. Schematic diagram of the fabrication method, and the image for CFRP and C/C composites.

3.3 Measurement

Interlaminar fracture toughness of the specimens was analyzed using the three-point bending test [20-22]. These specimens were cut of the size 60mm × 10mm × 4 mm. Straight notches from each specimens of 0.15mm width were prepared using an Isomet machine. In this paper, Notch depth (*a*) to length (S_0) of specimens ratio 1:4, span length 40mm, and a crosshead speed 0.5mm/min were kept. Bending load was applied perpendicular to the specimens. The specimen geometry was used to determine the mode II delamination fracture energy [20] as shown in Fig. 3.

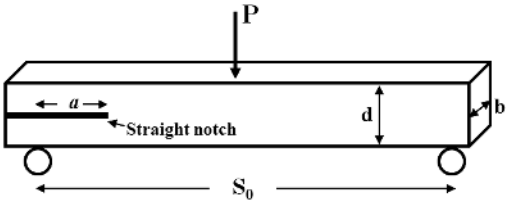

Fig. 3. Schematic diagram of the specimen geometry.

4. Results and discussion

From Figs. 4 (a) and (b), inter-layer fracture toughness shows the trend of increase as the deflection velocity of load point increases, and significantly higher inter-layer fracture toughness of CFRP specimen compared to C/C specimen. The peak values give the maximum load, which is required for the crack to propagate through the specimens. It indicates that the fiber volume fraction in the composite control its toughness. However some variation was expected due to the void content level. The crack surfaces were loaded in shear as shown in Fig. 4(c). Load-displacement curves were obtained during the

test and the crack front location was marked on the CFRP and C/C composites specimens during crack propagation. In order to eliminate the effect of a relatively blunt artificial crack, the initial crack propagation step was ignored and the crack length was adjusted correspondingly to the location of nascent crack tip. The fracture energy in Mode II, G_{IIC},of the specimens was calculated through an experiment according to the following Eqs. (3), (4) and (5).

$$G_{IIC} = \frac{9a^2 P^2 C}{2b(2L^3 + 3a^3)} \tag{3}$$

$$C = \frac{3a^3 + L^3}{2bh^3 E_l} \tag{4}$$

$$E_l I = \frac{PL^3}{48\delta} \tag{5}$$

where P is the critical load for crack initiation, C is the compliance, a is the crack length (between the support point and the edge of the crack), L is the support span, δ is the displacement, I is the moment of inertia of area, b and h are the width of the specimen and half thickness respectively, and E_l is the longitudinal modulus.

When the load is applied, the crack surfaces slide with friction, and thus dissipate part of the external work in the form of Mode II. Load-displacement traces were used in the calculation of the final G_{IIC} values. These are shown in Fig. 5 and Fig. 6, and showing a good agreement between experimental work and numerical calculations.

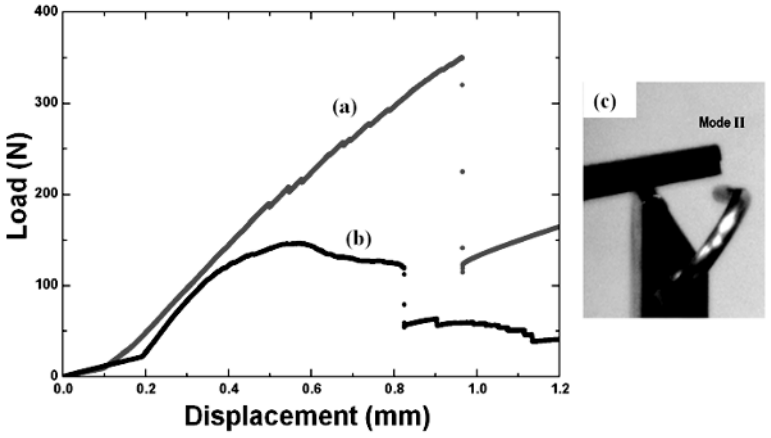

Fig. 4. Load vs. displacement curves for (a) CFRP and (b) C/C specimens, and (c) Mode II loads for a C/C specimen during fracture testing.

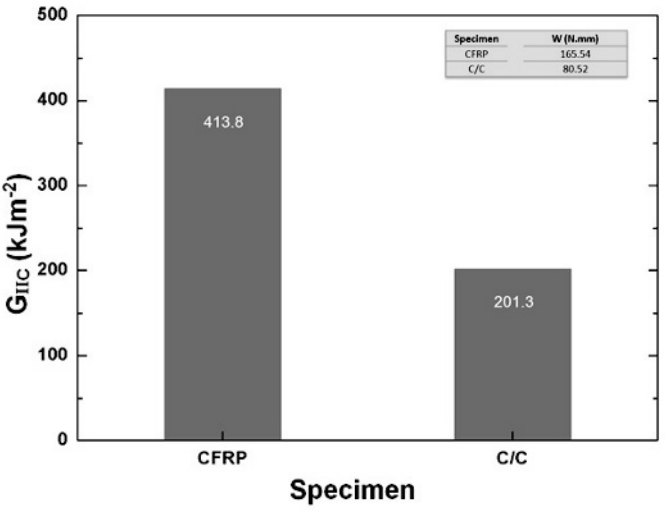

Fig. 5. Numerical values of interlaminar fracture energy, G_{IIC}, based upon Eqs. 1 and 2 under Mode II loading of CFRP and C/C specimens.

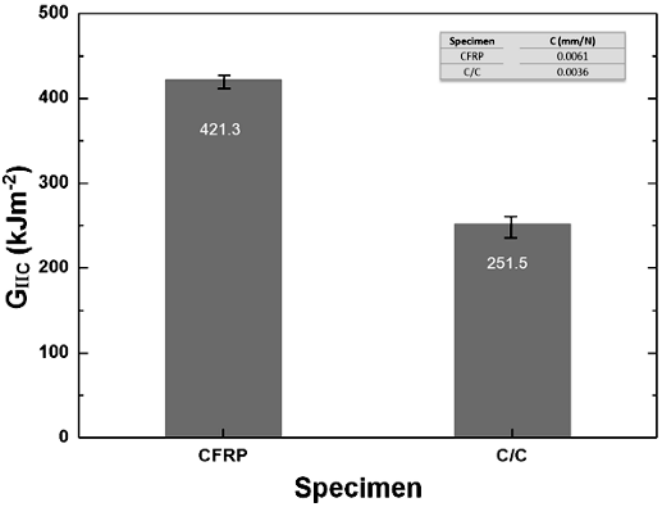

Fig. 6. Experimental values of interlaminar fracture energy, G_{IIC}, based upon Eqs. 3, 4 and 5 under Mode II loading of CFRP and C/C specimens.

5. Conclusions

The PAN/phenolic-based carbon/carbon (C/C) composites were prepared by pyrolyzing the carbon fiber reinforced phenolic resin-based plastics (CFRP) composites. A quadrangle method has been presented to evaluate fracture energy of PAN/phenolic-based carbon/carbon composites. The results obtained by a numerical technique have been confronted with the experimental results. The results are in good agreement with the experimental results.

References

[1] Gardziella A, Pilato LA, Knop A. Phenolic resins, chemistry, applications, standardization, safety and ecology. Springer. New York (2000).

[2] Vineta S, Gordana B, Dimko D. Composite material based on an ablative phenolic resin and carbon fibers. J Serb Chem Soc 2009; 74 : 441-453.

[3] Knop A, Scheib W. Chemistry and application of phenolic resins, Springer-Verlag. Berlin. 1979 : 97.

[4] Richardson MOW. Polymer engineering composites. Applied Science Publishers Ltd. London 1977 : 38.

[5] Fitzer E. Manocha LM. Carbon reinforcements and carbon/carbon composites. Springer. Berlin 1998; 250-319.

[6] Li JG, Hausner H. Reactive wetting in the liquid-silicon/solid-carbon system. J Am Ceram Soc 1996; 79 : 873-880.

[7] Liu Y, Zhang C, Qiao S, Yang Z. Fabrication and microstructure of C/Cu composites. Adv Eng Mater 2010; 12 : 493-496.

[8] Almir BS, Santos N, Lebre CLR. Flexural stiffness characterization of reinforced plastic (FRP) pultruded beams. Compos Struct 2007; 81 : 247-282.

[9] Li M, Matsuyama R, Sakai M. Interlaminar shear strength of C/C-composites: the dependence on test methods. Carbon 1999; 37 : 1749-1757.

[10] Zhandarov S, Mader E. Characterization of fiber/matrix interface strength: applicability of different tests, approaches and parameters. Compos Sci Technol 2005; 65 : 149-160.

[11] Paiva JMF, Mayer S, Rezende MC. Evaluation of mechanical properties of four different carbon/epoxy composites used in aeronautical field. Mater Res 2005; 8 : 91-97.

[12] Crouch B. Finite element modeling of the three-point bend impact test. Comput Struct 1993; 48 : 167-173.

[13] Birt EA, Smith RA. A review of NDE methods for porosity measurement in fiber reinforced polymer composites. Insight 2004; 46 : 681-686.

[14] Chen-Chi MM, Jia-Min L, Wen-Chi C, Tse-Hao K. Carbon/Carbon nanocomposites derived from phenolic resin-silica hybrid creamers: Microstructure, physical and morphological properties. Carbon 2002; 40 : 977-984.

[15] Schulte-Fischedick J, et al. The crack development on the micro- and mesoscopic scale during the pyrolysis of carbon fiber reinforced plastics to carbon/carbon composites. Composites: Part A 2007; 38 : 2171-278.

[16] Jenkins GM, Kawamura K. Polymeric carbons- carbon fiber, glass and char. Cambridge University Press. London (1976).

[17] Krenkel W, Gern F. Microstructure and characteristics of CMC manufactured via the liquid phase route, proceedings of the ninth international conference on composite materials. Madrid. Spain. July 12-16. 1993. Vol. II : Ceramic matrix composites and other systems; 173-181
[18] Wang CJ. The effect of resin thermal degradation on thermostructural response of carbon-phenolic composites and the manufacturing process of carbon-carbon composites. J Reinf Plast Compos 1996; 15 : 1011-1026
[19] Krenkel W. Carbon fiber reinforced CMC for high performance structurs. Int J Appl Ceram Technol 2004; 1 : 188-200.
[20] Russell AJ, Street KN. The effect of matrix toughness on delamination static and fatigue fracture under mode II shear loading of Graphite/Epoxy composites. ASTM STP 937.
[21] Yokoyama T. Determination of Dynamic fracture-initiation toughness using a novel impact bend test procedure. J Pressure Vessel Technol 1993; 115 : 389-397.
[22] Bacon C, Färm J, Lataillade J. Dynamic fracture toughness determined from load-point displacement. Exp Mech (1994); 20 : 217-223.